

# Structure Formation in Tokamak Turbulence: Impact of Collisions and Kinetic Electrons

Von der Universität Bayreuth  
zur Erlangung des Grades eines  
Doktors der Naturwissenschaften (Dr. rer. nat.)  
genehmigte Abhandlung

von

**Arne Weikl**

aus Bayreuth

1. Gutachter: Prof. Dr. Arthur G. Peeters
2. Gutachter: Prof. Dr. Alexander Kendl

Tag der Einreichung: 22. Mai 2019  
Tag des Kolloquiums: 18. Oktober 2019



*Betreut durch* PROF. DR. ARTHUR G. PEETERS



# Abstract

## Structure Formation in Tokamak Turbulence: Impact of Collisions and Kinetic Electrons

In this thesis, the formation of structures in the zonal  $E \times B$  shear flow of the plasma in a Tokamak fusion reactor is studied with the nonlinear Eulerian gyro-kinetic code GKW. As this sheared zonal flow suppresses ion temperature gradient driven turbulence, structures in the zonal flow have a vast impact on the heat transport observed in a Tokamak and thus play a crucial role in developing an efficient fusion reactor.

The formation of staircases in the shear of the zonal flow suppresses turbulence and leads to an upshift of the threshold in the temperature gradient, at which a significant heat flux is observed. The defining feature of this particular threshold, the so-called finite heat flux threshold, is that the heat flux does not go smoothly to zero when the threshold value is approached from above. An examination of the influence of ion-ion collisions reveals that this threshold is shifted to lower values due to collisions. Their influence is most prominent in the regime below the collisionless finite heat flux threshold and above the previously measured Dimits threshold. Investigating both the intensity as well as the radial profile of the  $E \times B$  shear rate allows to reliably link the radial structure of the staircase to the observed behaviour. Fully developed staircases are observed below the finite heat flux threshold, while partially developed staircases are observed above. Increasing the collision frequency hinders the transgression from a partial to a fully developed staircase, leading to the observed reduction of the finite heat flux threshold. The results cannot be explained satisfactorily by solely considering the shear intensity alone, which bolsters the importance of the structure formation in the  $E \times B$  shear.

Investigating  $E \times B$  shear structures in the zonal flow while treating the electrons as a fully kinetic species, reveals that the formation of staircases can be observed. However, in many cases strong small scale structures emerge in the shear rate, which appears to hinder staircase formation and prevents an efficient suppression of the turbulence induced heat transport. The small scale structures are linked to the self-interaction of turbulent modes through the double periodic boundary conditions of the toroidal geometry of a Tokamak plasma. Compared to simulations in the adiabatic electron limit, the influence of the boundary conditions is more prominent, because of the long extension of the mode structure along the field lines in the kinetic electron case. As the self-interaction is a newly discovered mechanism to drive the zonal flow, an extensive characterization is carried out.

It is found that the driven structures scale with the normalized Larmor radius, are weakly affected by collisions and are also observed in global simulations. Changing the boundary conditions through the variation of the magnetic shear weakens the small scale structures, which leads to a reappearance of the staircase structure and most of its typical traits.

The observation of the small scale structures driven by self-interaction in simulations with kinetic electrons raises the question, how effective certain zonal flow structures damp the ion temperature gradient instability driving the turbulence. To investigate this question, the growth rate of the turbulent modes after quenching is measured under the damping effect of a zonal flow profile. A quantitative measurement for the efficiency of a structure is provided by considering the damping in relation to the intensity of the zonal flow structure. All results of this examination lead to the conclusion that the damping is predominantly effected by zonal flow structures with a low radial wave vector.

# Zusammenfassung

## Strukturbildung in Tokamak-Turbulenz: Der Einfluss von Kollisionen und kinetischen Elektronen

In dieser Abhandlung wird die Strukturbildung in der zonalen  $E \times B$  Strömung des Plasmas eines Tokamak Fusionsreaktors mit Hilfe des nichtlinearen Euler'schen gyrokinetischen Codes GKW untersucht. Da diese gescherte zonale Strömung die Iontemperaturgradient-getriebene Turbulenz unterdrückt, haben Strukturen in der zonalen Strömung einen starken Einfluss auf den Wärmetransport in einem Tokamak und spielen deshalb eine wichtige Rolle bei der Entwicklung eines effizienten Fusionsreaktors.

Die Bildung von Treppenstrukturen (Staircases) in der Scherrate der zonalen Strömung unterdrückt die Turbulenz und führt zu einer Erhöhung des Schwellwerts im Temperaturgradienten, ab dem ein signifikanter Wärmefluss beobachtet wird. Das Besondere dieses Schwellwerts, dem sogenannten Schwellwert mit endlichem Wärmefluss (Finite Heat Flux Threshold), ist, dass der Wärmefluss sich unstetig der Null annähert, wenn man sich dem Schwellwert rechtsseitig annähert. Eine Untersuchung des Einflusses von Ionen-Ionen-Kollisionen zeigt, dass dieser Schwellwert durch Kollisionen nach unten verschoben wird. Der Einfluss der Kollisionen ist in dem Bereich zwischen dem bereits bekanntem Dimits-Schwellwert und dem kollisionsfreien Schwellwert mit endlichem Wärmefluss am stärksten. Eine Betrachtung der Intensität als auch des radialen Profils der  $E \times B$  Scherrate erlaubt es das Auftreten und die Form der Treppenstruktur eindeutig mit den Beobachtungen zu verknüpfen. Voll entwickelte Treppenstrukturen werden unterhalb des Schwellwerts beobachtet, während teilentwickelte Treppenstrukturen oberhalb beobachtet werden. Ein Erhöhen der Kollisionsfrequenz behindert den Übergang von einer teilentwickelten zu einer voll entwickelten Treppenstruktur, was zu der beobachteten Senkung des Schwellwert mit endlichem Wärmefluss führt. Diese Resultate können nicht durch die Intensität der Scherrate allein erklärt werden, was die Wichtigkeit der Strukturbildung in der  $E \times B$  Scherrate unterstreicht.

Eine Untersuchung der Strukturen in der  $E \times B$  Scherrate, bei der die Elektronen als vollwertige kinetische Spezies betrachtet werden, zeigt dass auch hier Treppenstrukturen beobachtet werden können. Jedoch treten auch oft starke, kleinskalige Strukturen auf, welche die Bildung von Treppenstrukturen und damit die Unterdrückung von Turbulenz behindern. Diese kleinskaligen Strukturen stehen mit der Selbstinteraktion turbulenter Moden durch die doppelt-periodischen Randbedingungen der toroidalen Geometrie

eines Tokamak-Plasmas in Verbindung. Verglichen mit Simulationen im adiabatischen-Elektronen Grenzfall ist hier in der kinetischen Betrachtung der Einfluss der Randbedingungen stärker, da die Modenstruktur entlang der Feldlinien weiter ausgedehnt ist. Da die Selbstinteraktion ein neu entdeckter Mechanismus ist um die zonale Strömung zu treiben, wird eine weitreichende Untersuchung und Charakterisierung durchgeführt. Hierbei wird festgestellt, dass die kleinskaligen Strukturen mit dem normierten Larmorradius skalieren, schwach von Kollisionen beeinflusst werden und auch in globalen Simulationen beobachtet werden können. Eine Veränderung der Randbedingungen durch eine Variation der magnetischen Scherung führt zu einer Abschwächung der kleinskaligen Strukturen, was zu einem erneuten Auftauchen der Treppenstrukturen führt.

Die Beobachtung der durch die Selbstinteraktion getriebenen, kleinskaligen Strukturen wirft die Frage auf, wie effektiv verschiedenen Strukturen in der zonalen Strömung die, die Turbulenz treibende Iontemperaturgradientinstabilität dämpfen. Um dieser Frage nachzugehen, wird die Wachstumsrate der turbulenten Moden nach der Unterdrückung gemessen, wobei der dämpfenden Einfluss von Strukturen in der Scherrate der zonalen Strömung berücksichtigt wird. Indem die Dämpfung mit der Intensität der Struktur in Relation gesetzt wird, kann die Effizienz der Struktur quantifiziert werden. Die Ergebnisse dieser Untersuchung ergeben, dass die Dämpfung hauptsächlich durch Strukturen mit einem kleinen Wellenvektor erfolgt.

# Acknowledgements

The greatest share of thanks goes to my supervisor Arthur Peeters, whose guidance during the course of this thesis has been proven irreplaceable. His insight and experience have been a great support and his ideas and encouragement were invaluable for the success of my research.

I would like to thank Florian Rath for the many insightful discussions on plasma physics and on staircases in particular and also the times spent outside of academia. Furthermore I would like to thank Felix Seiferling for the discussions not only on plasma physics while we shared an office. To Stefan Großhauser I would like to express my thanks for all the discussion on how to write good code and for encouraging me to implement the results of those discussions. Additionally I would like to thank Pierluigi Migliano, William Hornsby, Rico Buchholz and Lukas Krönert for the time we shared while working in plasma physics.

Outside of academia I would like to thank Jessica Pater for her kind and encouraging support during the creation of this thesis and also my father Karlheinz Weigl for his aid.



# Contents

<b>1. Motivation</b>	<b>13</b>
<b>2. Plasmas and Tokamaks</b>	<b>17</b>
2.1. Particle motion in a magnetised plasma . . . . .	17
2.2. Tokamak Fusion Reactor . . . . .	19
2.3. Turbulence due to the Ion Temperature Gradient instability . . . . .	25
2.4. Zonal flows and turbulence suppression thereby . . . . .	28
2.5. Structures in the zonal flow . . . . .	31
2.6. Collisions . . . . .	33
<b>3. Simulating Plasma</b>	<b>35</b>
3.1. Gyro-kinetics . . . . .	35
3.1.1. Kinetic description of a plasma . . . . .	35
3.1.2. Gyro-kinetic ordering . . . . .	36
3.1.3. The gyro-kinetic transform . . . . .	37
3.1.4. The gyro-kinetic equation . . . . .	38
3.2. Adiabatic electron response . . . . .	39
3.3. Field aligned coordinates and background magnetic field configuration . .	40
3.3.1. Hamada Coordinates . . . . .	40
3.3.2. Background magnetic field configuration . . . . .	44
3.4. Spectral representation . . . . .	45
3.5. Simulation domains in a Tokamak . . . . .	45
3.5.1. Flux-tube simulation . . . . .	45
3.5.2. Global simulation . . . . .	47
3.6. Gyro-Kinetic Workshop (GKW) . . . . .	48
3.6.1. Gyro-kinetic equation of GKW . . . . .	48
3.6.2. Normalization . . . . .	50
3.6.3. Implementation . . . . .	51
3.6.4. Modelling Collisions . . . . .	52
<b>4. Influence of collisions on the Finite Heat Flux Threshold</b>	<b>55</b>
4.1. Collisional damping of zonal flows . . . . .	56
4.2. Analysis Of The Finite Heat Flux Threshold . . . . .	60
4.3. Analysis of the shear intensity . . . . .	67
4.4. Analysis Of the radial shear profile . . . . .	71
4.5. Conclusion . . . . .	73

<b>5. Zonal flow generation through self-interaction</b>	<b>77</b>
5.1. Zonal flow drive through self-interaction . . . . .	78
5.2. Heat flux near marginal stability . . . . .	81
5.3. Physical nature of the small scale $\omega_{E \times B}$ structures . . . . .	86
5.4. Parameter dependence of the self-interaction . . . . .	89
5.5. Staircase structures with kinetic electrons . . . . .	93
5.6. Self-interaction in global simulations . . . . .	95
5.7. Self-interaction influenced by collisions . . . . .	99
5.8. Reduced time step in the electromagnetic picture . . . . .	101
5.9. Conclusion . . . . .	102
<b>6. Suppression of ITG due to structures in the zonal flow</b>	<b>105</b>
6.1. Numerical setup . . . . .	105
6.2. Comparison of growth rate spectra . . . . .	109
6.3. Relative Suppression Strength . . . . .	111
6.4. Relation to zonal flow spectrum . . . . .	113
6.5. Conclusion . . . . .	115
<b>7. Conclusion and Outlook</b>	<b>117</b>
<b>A. Running GKW with LAW</b>	<b>121</b>
<b>B. GTS-theory</b>	<b>123</b>

# 1. Motivation

Thermonuclear fusion appears as a promising solution to satisfy the worlds rising hunger for clean and sustainable energy. In a fusion reactor, two atomic nuclei are brought close together, leading to the formation of a different nuclei. For lighter elements, the reactants' mass exceeds the mass of the products. This mass difference is released as kinetic energy of the products, which can be harvested (to obtain electrical energy).

Atomic nuclei repulse each other due to the Coulomb force. To overcome this Coulomb barrier, the reactants need to have a high temperature. To obtain suitable fusion reaction rates  $10^8$  degrees Kelvin or more are required [1], as shown in Fig. 1.1, in which the reaction rates for feasible fusion reactions are depicted. At that temperature, the atoms

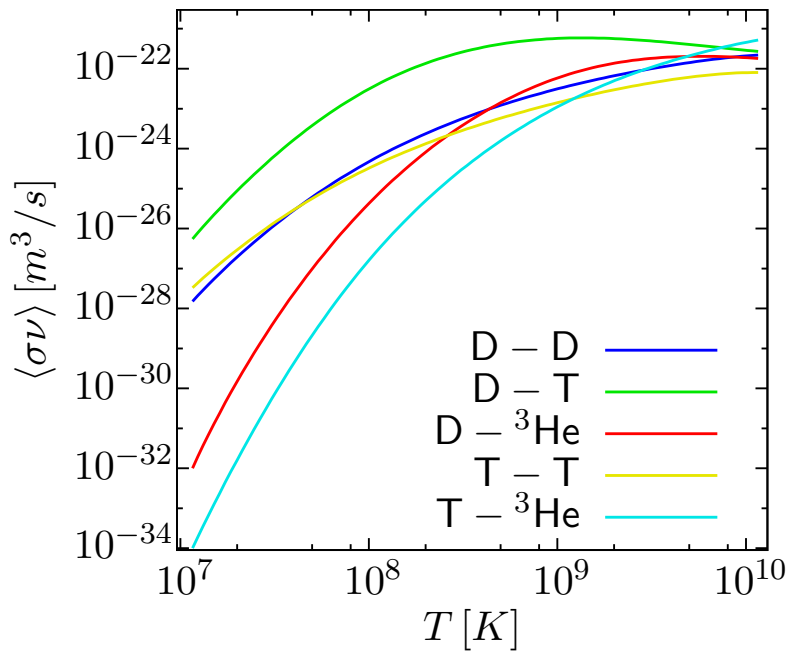


Figure 1.1.: Fusion reaction rates averaged over a Maxwellian distribution for promising fusion reactions [1, 2] labelled by their reactants: D - deuterium, T - tritium,  $^3\text{He}$  - helium-3.

are fully ionized, i.e. they are in the plasma state. Two promising methods to confine a fusion plasma are known: magnetic confinement and inertial confinement. In the field of magnetic confined fusion, the Tokamak and the Stellarator are the two favoured designs,

## 1. Motivation

both featuring a toroidally shaped magnetic field to contain the plasma. This work focuses on the Tokamak fusion reactor, whose defining feature is toroidal symmetry. An example of a Tokamak reactor experiment is the ASDEX Upgrade (Fig. 1.2) located near Munich. The next stage Tokamak, currently (as of 2019) under construction, will be the

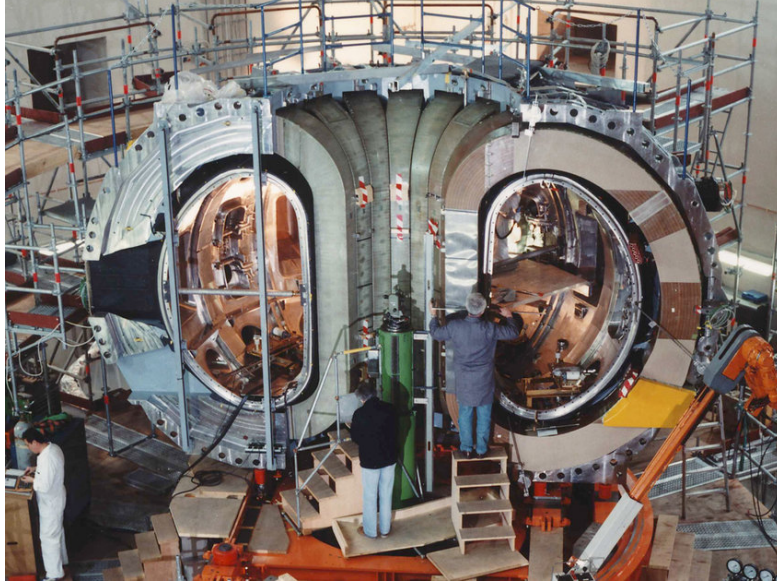


Figure 1.2.: ASDEX Upgrade during assembly. From Ref. [3].

International Thermonuclear Experimental Reactor (ITER) [4, 5] located in Cadarache (south France).

The intermediate goal of fusion reactor research is to achieve ignition, i.e. sustaining the required plasma temperature solely through the heating of the fusion process. This can be described as a constraint [6] for the triple product of the plasma's density  $n$ , the temperature  $T$  and the energy confinement time  $\tau_E$

$$nT\tau_E \geq 3 \cdot 10^{21} \frac{\text{keVs}}{\text{m}^3}, \quad (1.1)$$

given here for the generally favoured deuterium-tritium reaction. The value of  $nT\tau_E$  is determined by the quality of the magnetic confinement of a fusion reactor. Consequently, the improvement of the confinement is a prerequisite for ignition and is therefore one of the most focused topics in fusion research. The quality of the confinement is affected negatively by a multitude of effects, with turbulence in the plasma being the most important. Under reactor conditions, the ion temperature gradient instability, which is investigated in this thesis, is considered to be the dominant driving mechanism for turbulence. Turbulence can be suppressed or regulated by sheared zonal flow, i.e. a sheared, axisymmetric plasma rotation. The zonal flow is driven by the turbulence itself, leading to a self regulation of the turbulence and to an improvement of the confinement

of the plasma. Recent findings [7–11] show that structures form in the zonal flow, which enhance the stabilization of the turbulence. The main subject of this thesis is to understand how the structures formed in the zonal flow behave and how they affect the turbulence. It will improve the understanding and predictions of the turbulence and the quality of the confinement.



## 2. Plasmas and Tokamaks

In this chapter, a brief overview of the theoretical background used in the later chapters is given. An overview of typical mechanisms that govern the particle motion in a plasma is given in Sec. 2.1. Sec. 2.2 presents general information about a tokamak fusion reactor. The Ion Temperature Gradient instability (ITG), a cause of turbulence, is introduced in Sec. 2.3. In Sec. 2.4, the zonal flow, the common model to describe its generation and the suppression of turbulence through the zonal flow are discussed. After that, a short overview of the current state of research on the structure formation in the zonal flow is presented in Sec. 2.5. Finally, Sec. 2.6 gives a brief note on particle collisions in a plasma.

### 2.1. Particle motion in a magnetised plasma

Here, basic physical mechanisms that occur in a (tokamak) plasma are briefly presented. A more detailed treatment can be found, for example, in Refs. [6, 12, 13].

Due to the Lorentz force, charged particles in a magnetic field execute a circular motion with the (cyclotron) frequency

$$\omega_{c,s} = \frac{|q_s|B}{m_s} \quad (2.1)$$

in the plane perpendicular to the field. Here,  $m_s$  is the particle mass,  $q_s$  its charge,  $B$  the strength of the magnetic field and the particle species are denoted with a  $s$ -subscript. The radius of that motion is called Larmor (or gyro) radius  $\rho_s$

$$\rho_s = \frac{m_s v_{\perp,s}}{|q_s|B}, \quad (2.2)$$

where  $v_{\perp,s}$  is the particle's velocity perpendicular to the magnetic field. For typical tokamak parameters the Larmor radius ranges in the millimetres for ions (protons) and is a factor of fifty to hundred smaller for electrons [6]. The direction of the rotation depends on the sign of the charge, thus ions and electrons gyrate in the opposite direction. It is convenient to put the Larmor radius in relation to a system size, e. g. the major radius of the reactor  $R_{\text{ref}}$ , typically several meters. This defines a dimensionless normalized Larmor radius  $\rho_*$

$$\rho_* = \frac{\rho_i}{R_{\text{ref}}}, \quad (2.3)$$

commonly used in relation to the ion species. From the values given above it can be seen that  $\rho_*$  is very small for fusion reactors, being  $\approx 10^{-3}$  to  $\approx 10^{-4}$ . On a large scale

## 2. Plasmas and Tokamaks

particles can be considered as confined on a magnetic field line, exhibiting a free motion only along the magnetic field. This picture holds for a homogeneous, isotropic and static magnetic field without external forces, as only then the particles move in properly closed circles (in projection). In a reactor, the field configuration deviates from these assumptions. Under these circumstances the particle orbits do not close upon themselves (in projection), leading to a small net particle motion perpendicular to the field lines, i.e. a drift of the centre of the gyro motion. Although the aforementioned picture is still valid on a coarse level, corrections have to be introduced to describe the drifting of the particles. Compared to the motion along the magnetic field, the motion due to the drifts is small, i.e. of the order of  $\rho_*$ , as it is related to the inhomogeneities on the scale of the Larmor radius. The most important of these drifts will be briefly explained in the following.

In the presence of an electric field with a component perpendicular to the magnetic field, particles undergo the so-called  $E \times B$  drift  $\mathbf{v}_{d,E \times B}$ , which moves the particle in the direction perpendicular to both fields. Through the Coulomb force the electric field leads to an acceleration of the particle over one half of the gyration and a deceleration over the other half. From Eq. (2.2) it can be seen that this leads to a correspondingly varying Larmor radius such that the centre of the gyromotion moves, as depicted schematically in Fig. 2.1. Considering that both the direction of the Coulomb force and the circumferential

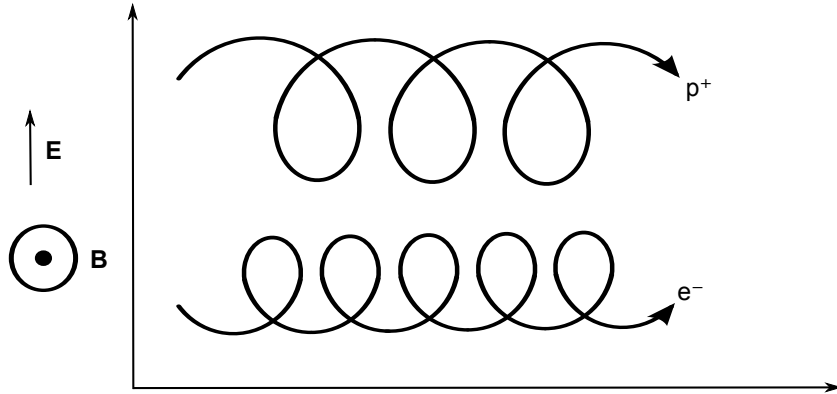


Figure 2.1.: Schematic of the  $E \times B$  drift.

direction depend of the sign of the particle's charge, it can be seen that the direction of  $\mathbf{v}_{d,E \times B}$  does not depend on the sign of the particle's charge. Solving the equation of motion under the influence of the Lorentz force for a particle leads to

$$\mathbf{v}_{d,E \times B} = \frac{\mathbf{E} \times \mathbf{B}}{B^2}, \quad (2.4)$$

where  $\mathbf{E}$  denotes the electric field. This mechanism can be applied not only to the Coulomb force, but also to an arbitrary force  $\mathbf{F}$  leading to a general drift  $\mathbf{v}_d$

$$\mathbf{v}_d = \frac{\mathbf{F} \times \mathbf{B}}{qB^2}, \quad (2.5)$$

However, as in general  $\mathbf{F}$  does not depend on the particle's charge, the direction of  $\mathbf{v}_d$  does depend on the charge. If the magnetic field exhibits inhomogeneities, the  $\nabla B$  drift  $\mathbf{v}_{d,\nabla B}$  is found. It can be described heuristically by a variation of the Larmor radius through the spatial variation of the strength of  $B$ . Again from the equation of motion, under the assumption of a large gradient length compared to the Larmor radius,

$$\mathbf{v}_{d,\nabla B} = \frac{mv_{\perp}^2}{2q} \frac{\mathbf{B} \times \nabla B}{B^3} \quad (2.6)$$

is obtained. It can be seen that the direction of the  $\nabla B$  drift does depend on the particle charge. If a particle's gyrocentre follows a curved magnetic field line, a drift perpendicular to the curvature radius, the so-called curvature drift  $\mathbf{v}_{d,R}$ , appears. When the particle follows the curved field line with curvature radius  $R_c$ , it is subjected to a centrifugal force, leading to a deviation of the circular motion and subsequently, a drift. To describe  $\mathbf{v}_{d,R}$ , a general drift, i.e. Eq. (2.5) with a centrifugal force is used. Assuming a large curvature radius, this leads to

$$\mathbf{v}_{d,R} = \frac{mv_{\parallel}^2}{qR_c^2} \frac{\mathbf{R}_c \times \mathbf{B}}{B^2} = \frac{mv_{\parallel}^2}{q} \frac{\mathbf{B} \times (\mathbf{B} \cdot \nabla)\mathbf{B}}{B^4}. \quad (2.7)$$

Again, the direction of the drift depends on the sign of the particle's charge. For a plasma where the pressure is low compared to the magnetic field strength,

$$\mathbf{v}_{d,R} \approx \frac{mv_{\parallel}^2}{q} \frac{\mathbf{B} \times \nabla B}{B^3} \quad (2.8)$$

can be written, which allows to treat  $\mathbf{v}_{d,R}$  similar to  $\mathbf{v}_{d,\nabla B}$ . A time varying electric field leads to the polarization drift  $\mathbf{v}_{d,p}$ . The temporal variation of  $\mathbf{E}$  leads to a variation of the Larmor radius, resulting in the drift

$$\mathbf{v}_{d,p} = \frac{1}{\omega_c B} \frac{d\mathbf{E}}{dt}, \quad (2.9)$$

which also depends on the charge.

## 2.2. Tokamak Fusion Reactor

In this section, the basics of a tokamak fusion reactor are presented. For a more in-depth treatment Ref. [6] is advised. A Tokamak confines a plasma magnetically. A correspondingly strong magnetic field leads to a gyro-radius much smaller than the device size, preventing the particles from escaping perpendicularly to the magnetic field. To prevent the particles from leaving the reactor through the motion along the magnetic field lines, the magnetic field is shaped in the form of a torus, as sketched in Fig. 2.2. Such a magnetic field, which has only a toroidal component, however, does not lead

2. Plasmas and Tokamaks

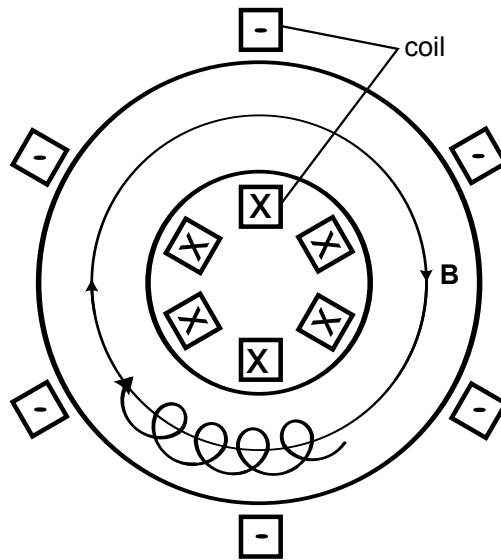


Figure 2.2.: Simple toroidal confinement.

to a stable configuration. Due to the toroidal curvature, the magnetic field possesses a radial gradient with a higher magnetic field strength obtained closer to the axis of symmetry. Following Eq. (2.6) and Eq. (2.7) it can be seen that this leads to a curvature and  $\nabla B$  drift of the particles as depicted in Fig. 2.3. Because these drifts are charge

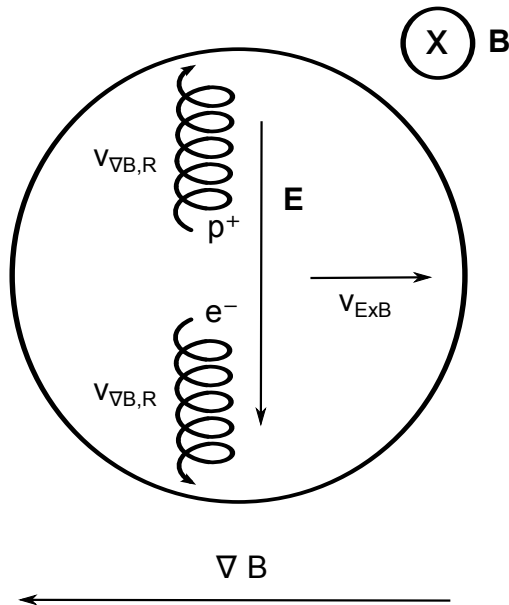


Figure 2.3.: View of a poloidal cut with the  $\nabla B$  drift and the resulting  $E \times B$  drift in a tokamak.

dependent, they lead to a charge separation and consequently to the generation of an electric field. As shown in Eq. (2.4), the electric field leads to a radially outward  $E \times B$  drift, also shown in Fig. 2.3, which carries all particles outwards onto the device wall. To prevent this, the magnetic field is twisted helically by superimposing a poloidal field. In this configuration, a particle following a magnetic field line is subjected to the  $\nabla B$  drift both on the upper and the lower side, leading to a compensation, which allows a stable magnetic confinement. A schematic overview of a tokamak is given in Fig 2.4 (in comparison, a technical sketch of ITER is given in Fig. 2.7). The field in the toroidal

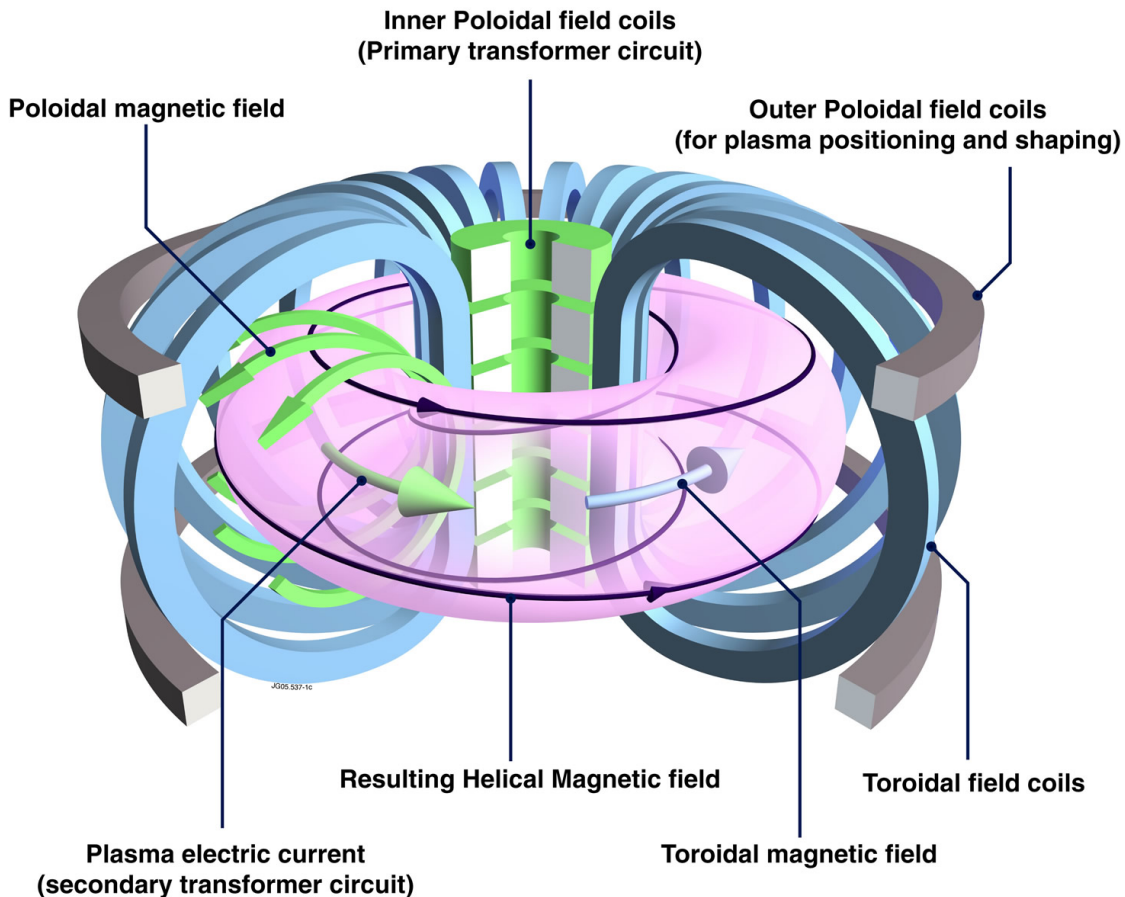


Figure 2.4.: Schematic view of a tokamak fusion reactor. From Ref. [14].

direction is produced by the corresponding main field coils. To generate the poloidal field, a toroidal current is induced in the plasma, commonly through central poloidal (transformer) coils. Additional coils are used for fine tuning of the plasma position and shape. Due to the need to induce the current via a change of the magnetic flux in the primary transformer coil, a tokamak can only operate in a pulsed mode.

The geometry of the magnetic field configuration in a tokamak is described as a set of

## 2. Plasmas and Tokamaks

nested surfaces with constant magnetic flux, so-called flux-surfaces. Following toroidal coordinates are introduced to gain an initial description, they are sketched in Fig. 2.5. The major radius of a torus  $R_{\text{ref}}$  describes the distance to the magnetic axis, being

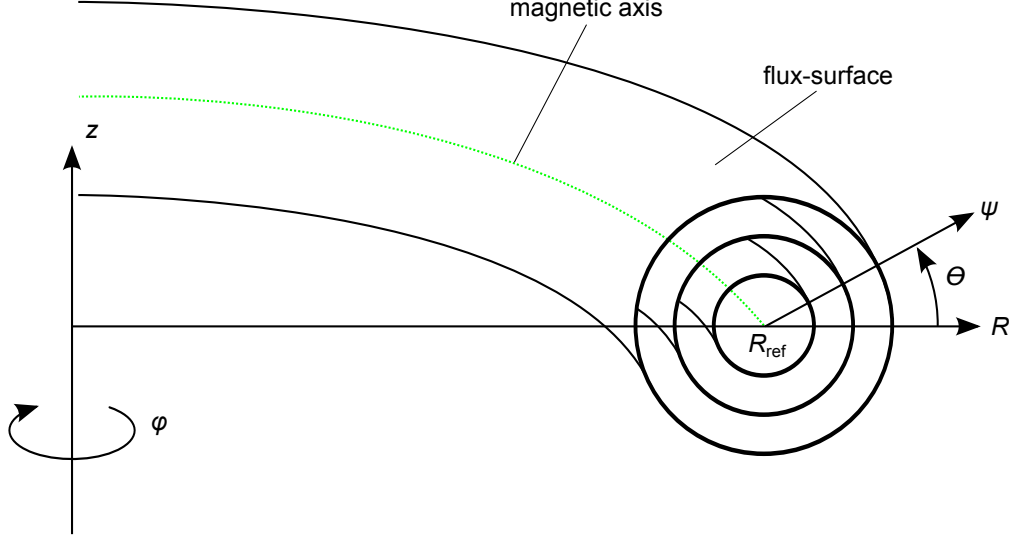


Figure 2.5.: Sketch of nested flux-surfaces and toroidal coordinates  $(\psi, \theta, \phi)$  and for reference, cylindrical coordinates  $(R, -\phi, z)$ . For convenience, the special case of circular and concentric flux-surfaces is depicted.

the innermost flux-surface. The flux-surfaces are labelled by the corresponding flux  $\psi$ . Generally, the radius of a flux-surface depends on the poloidal angle  $\theta$ , where the exact form can be determined by the Grad-Shafranov equation [15]. In a tokamak, the toroidal magnetic field component is an order of magnitude larger than the poloidal field component. Consequently, the vector that lies inside the magnetic surface and is perpendicular to the field makes only a small angle with the unit vector of the poloidal direction, so they are often used as synonyms. The toroidal angle is denoted  $\phi$ . For theoretical studies, the described configuration is often simplified under the assumption of circular and concentric flux surfaces. In that case, the minor radius  $r$ , comparable to  $\psi$ , is used. To describe the form of a flux surface, the inverse aspect ratio

$$\varepsilon = \frac{r}{R} \quad (2.10)$$

is defined. An important quantity to describe a tokamak plasma is the safety factor  $q$ . It is defined as the number of toroidal revolutions needed by a field line to end up at the same poloidal position. If  $q$  has a rational value, the field line closes upon itself, if irrational, the field line traces out the flux-surface. From definition one obtains

$$q = \frac{1}{2\pi} \oint \frac{1}{R} \frac{B_\phi}{B_\theta} ds, \quad (2.11)$$

which gives for small  $\varepsilon$

$$q = \varepsilon \frac{B_\phi}{B_\theta}. \quad (2.12)$$

The safety factor varies with the minor radius and plays an integral role for large scale magnetohydrodynamic instabilities, hence its name. To describe this variation, the (magnetic) shear  $\hat{s}$

$$\hat{s} = \frac{r}{q} \frac{\partial q}{\partial r} \quad (2.13)$$

is defined. To describe the quality of the confinement, the so-called plasma- $\beta$  is used. It is the ratio of the kinetic and the magnetic pressure and is defined as

$$\beta = \frac{p}{B^2/2\mu_0}, \quad (2.14)$$

where  $p$  is the pressure and  $\mu_0$  the magnetic permeability.

Due to the toroidal shape, the strength of the magnetic field changes if one follows the twisted magnetic field lines around the torus. At the outboard mid plane, the magnetic field has a minimum, thus called the low field side, while at the inner board side, the field has a maximum, thus called the high field side. For circular concentric flux surfaces  $B(\theta)$  is given as

$$B(\theta) = \frac{B_0}{1 + \varepsilon \cos \theta}. \quad (2.15)$$

The variation of the magnetic field along the field line leads to trapping of (a part of the) charged particles on the low field side. This can be seen by considering the magnetic moment and energy of the particle. The magnetic moment of a gyrating particle, which can be shown to be a constant of motion, is

$$\mu = \frac{mv_\perp^2}{2B(\theta)} = \text{const.} \quad (2.16)$$

Thus, the variation of  $B(\theta)$  along a field line yields a variation of the perpendicular velocity  $v_\perp$ . Since the total kinetic energy of a particle

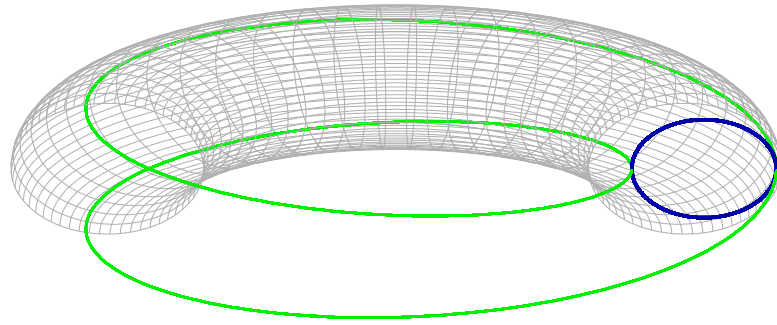
$$W = \frac{m}{2}v^2 = \frac{m}{2}v_\parallel^2 + v_\perp^2 = \text{const.} \quad (2.17)$$

is conserved, the velocity along the field line  $v_\parallel$  decreases as the particle moves from the low field side to the high field side. A particle with a parallel velocity on the low field side that satisfies

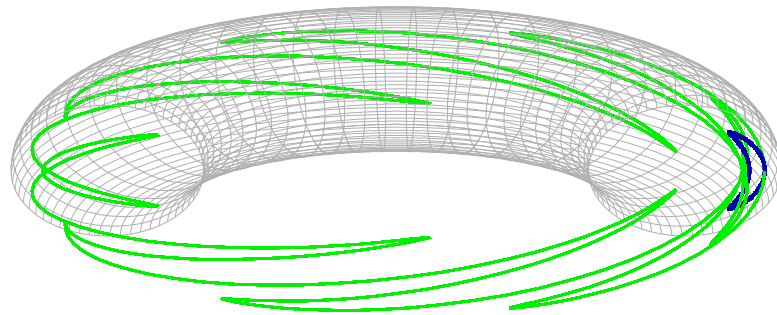
$$v_\parallel \leq \left( \frac{B_{\min}}{B_{\max}} - 1 \right) v_\perp, \quad (2.18)$$

cannot reach the high field side and is trapped in the magnetic field well. Particles with a  $v_\parallel$  above that threshold are commonly denoted passing particles. The poloidal projections of the particle's orbits of both cases are shown in Fig. 2.6a and Fig. 2.6b.

## 2. Plasmas and Tokamaks



(a) Sketch of the orbit of a passing particle's gyro-centre in a tokamak (green). The projection on a poloidal plane is shown in dark blue. The field is oriented outwards in that poloidal plane whereas the particles move inwards.



(b) Sketch of the orbit of trapped particle's gyro-centre in a tokamak (green). The projection on a poloidal plane is shown in dark blue. The field is oriented outwards in that poloidal plane whereas the particles move inwards.

The passing particles exhibit a circular curve, slightly shifted due to drifts, whereas the trapped particles show a “banana” shaped orbit.

The largest tokamak experiment, a grand international project, will be the International Thermonuclear Experimental Reactor (ITER) [4, 5], located in the south of France, with the first plasma to be scheduled in 2025 [16] (as of 2019). Its plasma geometry has a major radius of 6.2m, a minor radius of 2m and a volume of  $840\text{m}^3$  [16]. A sketch is shown in Fig. 2.7. Further tokamak experiments notable for this thesis that are operating, are ASDEX Upgrade [3] (Germany), DIII-D [17] (US) and JET [18] (UK). They are predecessors of ITER, with their major radii being about a factor of 2 to 4 smaller. A historical overview of fusion research, inter alia detailing their involvement, can be found in Ref. [19]

### 2.3. Turbulence due to the Ion Temperature Gradient instability

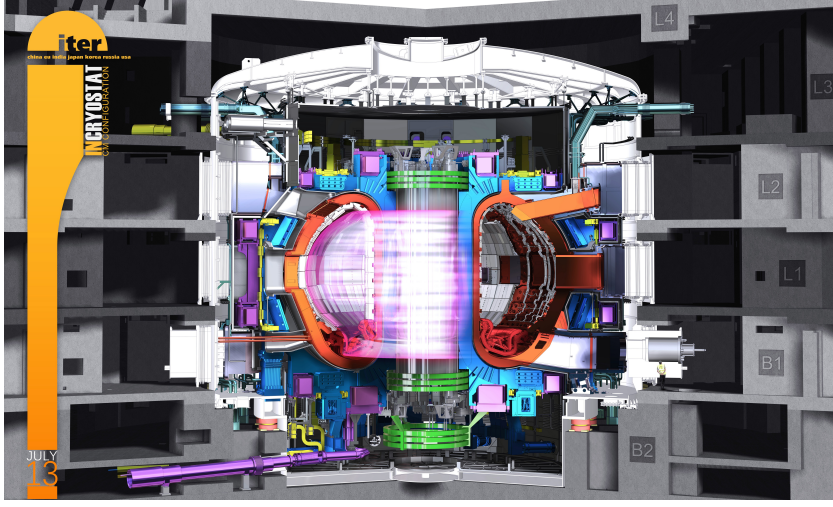


Figure 2.7.: Sketch of ITER. From Ref. [16].

### 2.3. Turbulence due to the Ion Temperature Gradient instability

In the plasma of a fusion reactor, the Ion Temperature Gradient (ITG) instability (see for example Ref. [20] and references therein) is expected to be the dominant instability leading to anomalous transport connected with turbulence. The understanding of the ITG requires the concept of drift waves (see for example Refs. [6, 12]). They are self-consistent wave-like density perturbations and flow velocity patterns that propagate across the magnetic field due to a density gradient in the plasma. Drift waves are not necessarily unstable and can be purely travelling waves, however they become unstable due to dissipative effects in the plasma. As they do not depend on the curvature of the magnetic field, a simplified description can be carried out in slab-like geometry (where magnetic field lines are straight and  $r \equiv x$ ,  $\theta \equiv y$ ,  $\varphi \equiv z$ ,  $\mathbf{B} = B\mathbf{e}_z$ ) that represents a poloidally small part of the torus. Starting with a small plane wave perturbation of the background ion density  $n_{0,i}$ :

$$n_i \propto \exp[k_y y - \omega t]. \quad (2.19)$$

The electrons react significantly faster than the ions due to their smaller mass and move along the magnetic field lines ( $z$ -direction) to restore quasi-neutrality, which leads to a change in the electron pressure

$$p_e = (n_{0,e} + n_e)T_{0,e}, \quad (2.20)$$

with the electron density perturbation  $n_e$  and the (here unperturbed) temperature  $T_{0,e}$ . Thereby, the electrons obey the (simplified) force balance

$$(n_{0,e} + n_e)m_e \frac{\partial v_{\parallel,e}}{\partial t} = -\frac{\partial p_e}{\partial z} + (n_{0,e} + n_e)eE_z, \quad (2.21)$$

## 2. Plasmas and Tokamaks

The inertial term is neglected, as the electron reaction is considered instantaneous on the time scale of the ion dynamics, such that the pressure is balanced only by the electric field. Assuming that  $T_{0,e}$  is constant in the small region considered here and neglecting second order terms, this results in

$$T_{0,e} \frac{\partial n_e}{\partial z} = n_{0,e} e \frac{\partial \phi}{\partial z}, \quad (2.22)$$

which leads to the adiabatic electron response

$$n_e = n_{0,e} e \frac{\phi}{T_{0,e}}, \quad (2.23)$$

which generates a potential perturbation  $\phi$  in phase with the density perturbation  $n_i$ . The resulting electric field leads to an  $E \times B$  drift of the ions  $\mathbf{v}_E = -ik_y \phi / B \mathbf{e}_x$ . Their reaction is described with the linearised continuity equation:

$$\frac{\partial n_i}{\partial t} = -\mathbf{v}_E \cdot \nabla n_{0,i}. \quad (2.24)$$

The drift is aligned with the density gradient  $\nabla n_{0,i} / n_{0,i} = -\mathbf{e}_x / L_n$  and moves ions into the region of the perturbation out of phase in relation to the density perturbation. From the dense region, plasma is moved (in  $x$ -direction) to one side of a high density region of the perturbation. From the region with lower background density, plasma is moved to the other side of that perturbation's region. This results in a propagation of the perturbation:

$$-i\omega n_i = -\frac{ik_y \phi}{B} \frac{n_{0,i}}{L_n}. \quad (2.25)$$

Assuming quasineutrality  $n_i = n_e$  and Eq. (2.23), the frequency of the drift wave is given as

$$\omega = \frac{k_y T_{0,e}}{e B L_n}. \quad (2.26)$$

A sketch of the drift wave process is shown in Fig. 2.8. Note that in reality, this process (and also the process described in the following) is not a successive, but rather a simultaneous process, as quasineutrality has to be satisfied.

For the ITG instability to arise from drift waves, in addition to the density gradient, an ion temperature gradient and a magnetic field gradient (and a curved magnetic field), as found in toroidal configurations, have to be present. When the ion temperature gradient is parallel to the density gradient, the drift wave mechanism pulls dense and also hot plasma, and similarly, less dense and also cold plasma into the corresponding regions of the perturbation. Consequently, the density perturbation of the drift waves coincides with an  $\pi/2$  out of phase temperature perturbation  $T_i$ . As described in Sec. 2.1, the  $\nabla B$  drift (and the curvature drift)  $\mathbf{v}_d$  lead to a temperature dependent motion of a particle's gyrocentre in the poloidal (corresponds to  $\mathbf{e}_y$ ) direction. The drift velocity  $v_d$  depends on the velocity of the particles, thus  $v_d$  depends on the plasma temperature. Therefore,

### 2.3. Turbulence due to the Ion Temperature Gradient instability

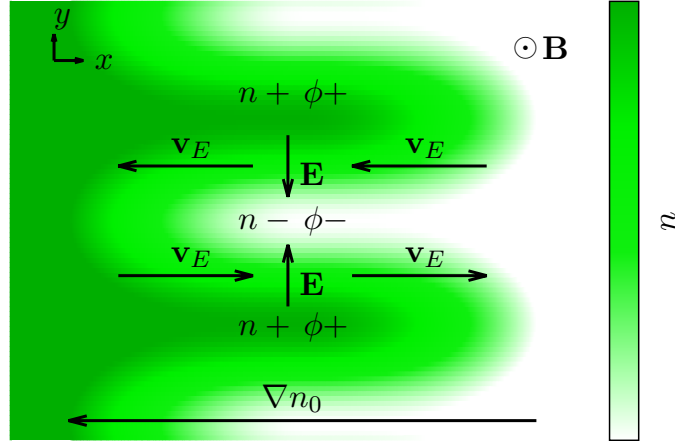


Figure 2.8.: Sketch of the density  $n$  of a drift wave in slab geometry (with  $\mathbf{B} = B\mathbf{e}_z$ ) with a background density gradient  $\nabla n_0$ . A perturbation of the ion density ( $n+$ ,  $n-$ ) leads to a potential perturbation ( $\phi+$ ,  $\phi-$ ) due to the electron dynamic. The electric field results in an  $E \times B$  drift of the ions, which is aligned to the background density gradient. From the high (low) background density region, plasma is moved to the upper side of a high (low) density region of the perturbation. The perturbation moves upwards.

more particles are moved from a hot region of the temperature perturbation than from a cold region. On the outboard side of the torus, the magnetic field gradient is parallel to the other gradients and the plasma of a hot region (cold region) is moved towards a high density region (low density region). Then the perturbations grow due to the favourable phase difference, the drift waves become unstable (and have a complex frequency) and the ITG is observed. If the magnetic field gradient is anti-parallel, as found on the inboard side, the  $\nabla B$  drift is reversed, which leads to a stabilization of the drift waves through the described mechanism. A schematic synopsis of this process is given in Fig. 2.9. The (adiabatic) ITG does not lead to a time averaged particle flux in the radial (corresponds to  $\mathbf{e}_x$ ) direction. However, the time averaged heat flux  $Q$  in the radial direction is non-zero, as the temperature perturbation and the  $E \times B$  drift due to the perturbation is out of phase:

$$Q = \langle T_e \mathbf{v}_E \cdot \mathbf{e}_x \rangle_t. \quad (2.27)$$

The calculation of  $Q$  requires the knowledge of the fluctuations, which are obtained through nonlinear simulations.

ITG turbulence exhibits a threshold in the temperature gradient, with the ITG developing only for temperature gradients above the critical value. In fact, several thresholds are known: the linear threshold, the nonlinear threshold and the finite-heat-flux-threshold. The linear threshold is calculated from linear theory with the ITG developing only for temperature gradients above the critical value. The nonlinear threshold, described in

## 2. Plasmas and Tokamaks

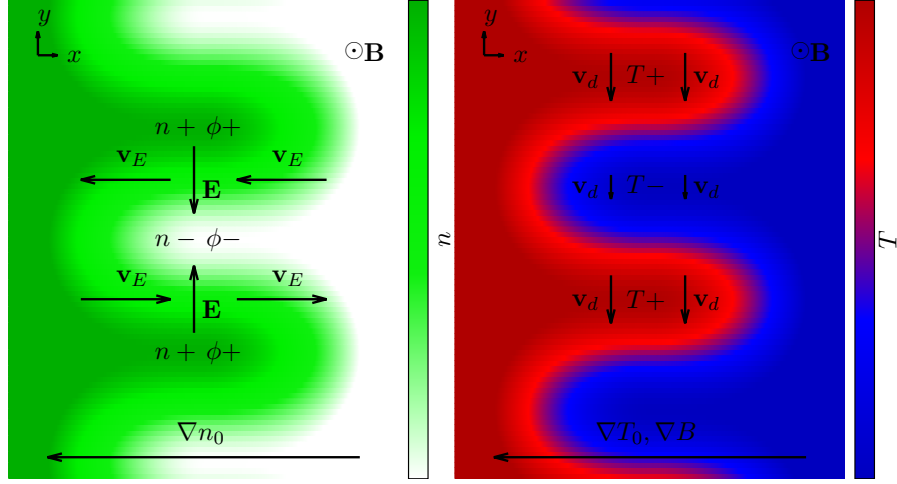


Figure 2.9.: Sketch of the ITG instability. The density  $n$  is shown on the left, the (ion) temperature  $T$  is shown on the right. Drift waves are augmented with a gradient of the background temperature and background magnetic field. A temperature perturbation  $\pi/2$  out of phase with the density perturbation is observed. The gradient of the magnetic field leads to a temperature dependent  $\nabla B$  drift, that reinforces the density perturbation, which renders the drift waves unstable.

Ref. [21], lies at a higher temperature gradient and is found in nonlinear turbulence studies. The up-shift in the threshold compared to the linear theory is caused by the zonal flow, a secondary mechanism that stabilizes the turbulence, which will be explained in the next section. The finite-heat-flux-threshold [11] shifts the observed threshold further upwards and is related to structure formation in the zonal flow.

An important numerical test case for ITG turbulence is the so-called cyclone base case (CBC). It represents a parameter set from an ITER-relevant DIII-D [17] high confinement shot (shot #81499,  $t = 4000\text{ms}$ , Ref [22]). Its importance stems from the use in Ref. [21], where the several physical models and also different numerical implementations were compared towards their prediction of ITG turbulence and the resulting transport. From then on, the cyclone base case has served as a common benchmark for many models and applications, further consolidating its relevance. For these reasons it is often employed in the studies of this thesis.

### 2.4. Zonal flows and turbulence suppression thereby

Zonal flows are latitude parallel, toroidally symmetric shear flows, i.e. being only a function of the radial coordinate. In the radial direction bands are formed, as sketched in Fig. 2.10. This band structure is reminiscent of the atmospheric phenomena, paradigmatic being the distinct belt structure perceptible in the Jovian atmosphere [23]. Zonal flows

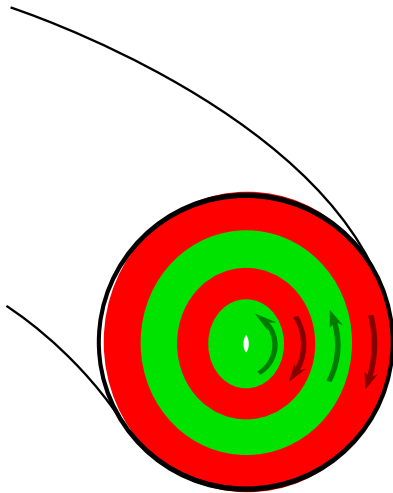


Figure 2.10.: Sketch of zonal flows in a plasma.

are linearly stable, but are nonlinearly driven by turbulence. To describe the evolution of the zonal flow, the momentum balance equation can be used (for a more elaborate derivation see for example Ref. [24]). Using the Reynolds decomposition, assuming incompressibility and taking the flux surface average (denoted as  $\langle \dots \rangle$ ) one obtains for the zonal flow velocity  $v_{ZF}$

$$\frac{\partial v_{ZF}}{\partial t} = -\frac{\partial}{\partial \psi} \tau. \quad (2.28)$$

Here,  $\tau$  denotes the flux surface averaged Reynolds stress

$$\tau = \langle v_\psi v_\theta \rangle, \quad (2.29)$$

determined with the radial and binormal component of the  $E \times B$  flow,  $v_\psi$  and  $v_\theta$  respectively. The zonal flow is related to a potential  $\phi_{ZF}$  that is only a function of the radial coordinate

$$v_{ZF} = \frac{1}{B} \frac{\partial \phi_{ZF}(\psi)}{\partial \psi}. \quad (2.30)$$

A heuristic picture of the zonal flow drive can be given as follows. Isotropic turbulence, which can be visualized with perfectly circular turbulent vortices, leads to a vanishing Reynolds stress as the products  $v_\psi v_\theta$  cancel in the flux surface average due to symmetry. However, a small shearing of the turbulent vortex breaks the symmetry and results in a non-vanishing averaged Reynolds stress and a net flow leading to a further shearing of the turbulent vortex. The mechanism outlined above represents an instability known as the modulation instability [25, 26]. A more elaborate quantitative approach assumes a multi-mode-interaction, the so-called four-wave approach, which is treated for example in Refs. [25–29]. Although the evolution of zonal flows is governed by nonlinear processes, significant insights can be gained from their linear response to perturbations akin to turbulence [30]. The response kernel  $\mathcal{K}(t)$  for the evolution of the (spectral) zonal

## 2. Plasmas and Tokamaks

potential after an initial perturbation is given as [30–32]:

$$\mathcal{K}(t) = \frac{\phi_{k_\psi}(t)}{\phi_{k_\psi}(0)} = \mathcal{K}_{\text{GAM}}(t)(1 - \mathcal{K}_{\text{R}}) + \mathcal{K}_{\text{R}}. \quad (2.31)$$

Early on, a damped Geodesic Acoustic Mode (GAM) [33] with frequency  $\omega_{\text{GAM}}$  is found, which is described with

$$\mathcal{K}_{\text{GAM}}(t) = \cos(\omega_{\text{GAM}}t) \exp(-\gamma_{\text{GAM}}t), \quad (2.32)$$

with the damping rate  $\gamma_{\text{GAM}}$ . At later times, after the GAM has decayed, a residual potential remains:

$$\mathcal{K}_{\text{R}} = \frac{1}{1 + 1.6q^2/\varepsilon^{1/2}}, \quad (2.33)$$

valid for collisionless ITG turbulence.

Zonal flows can be damped by various effects. The damping due to collisions [32, 34, 35] is investigated in this thesis. It occurs through the friction force between the trapped and passing particles enhancing the shielding of the zonal potential through the neoclassical polarization and the relaxation of the (velocity) distribution function towards a Maxwellian. In the response kernel it can be accounted for with a decaying residual [32, 35], i.e.  $\mathcal{K}_{\text{R}} \rightarrow \mathcal{K}_{\text{R}}(t)$ . Ref. [35] proposes to use

$$\mathcal{K}_{\text{R}}(t) = \frac{\varepsilon^2/q^2}{1 + \varepsilon^2/q^2} \left[ 1 + \frac{1 - \Theta}{\Theta + \varepsilon^2/q^2} \exp\left(-\frac{(1 + \varepsilon^2/q^2)\Gamma}{\Theta + \varepsilon^2/q^2} \frac{t}{\tau_{ii}}\right) \right] \quad (2.34)$$

instead of Eq. (2.33). Here,  $\Theta \approx 1.635\varepsilon^{3/2}$  and  $\Gamma \approx 0.6\sqrt{\varepsilon}$  describe the aspect ratio corrections. Furthermore, the damping due to turbulent momentum transport should be noted [36].

Zonal flows lead to the suppression or regulation of turbulence [37–43]. A direct effect of this suppression is the already mentioned nonlinear up-shift of the ITG turbulence threshold, observed in Ref. [21], the so-called Dimits-shift. As this has a strong influence of the resulting transport and thus the quality of the confinement of a tokamak, zonal flows are considered with strong interest. The suppression of turbulence can be attributed to the shear decorrelation of the turbulent fluctuations, described in Refs. [44, 45] and is proposed as an explanation for the high confinement regime (H-mode) found in Tokamaks (first observed in ASDEX) [46]. Here, a sheared background flow  $\mathbf{v}_{\text{ZF}}$  is added to a generic fluid model where a fluctuating field  $\zeta$  evolves according to

$$\left( \frac{\partial}{\partial t} + (\mathbf{v}_{\text{ZF}} + \mathbf{v}) \cdot \nabla + L_d \right) \zeta = S, \quad (2.35)$$

with the a free energy source  $S$  and a sink  $L_d$ . It leads to a reduced radial correlation length of the fluctuations and as a consequence, the fluctuation level is reduced compared

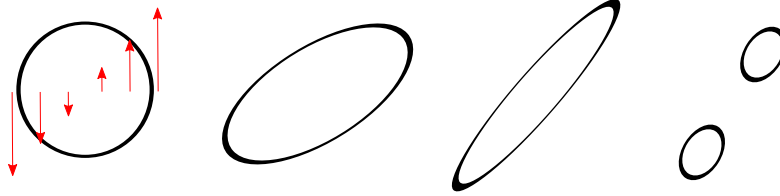


Figure 2.11.: A sheared  $E \times B$  flow leads to a tilting of turbulent vortices and eventually to the suppression of these structures.

to its ambient level. Furthermore, the shear leads to a damping of the turbulence due to a tilting of the vortices [47], depicted in Fig. 2.11. The vortices are sheared due to the  $E \times B$  flow in the background, which leads to a tilted elongation. If elongated sufficiently, a vortex breaks into smaller vortices, i.e. the turbulent structures are suppressed and the resulting transport is reduced. Structures with a large radial extend are affected more and fast temporally varying shear flows do not contribute significantly [48]. The general idea is condensed in the so-called Waltz rule/criterion [49, 50]. It states that effective turbulence suppression will occur if the zonal flow shear rate is comparable to the growth rate of the ITG instability:

$$\omega_{E \times B} \approx \gamma_{\text{ITG}}. \quad (2.36)$$

Hereby the shear rate of the zonal flow, i.e. the radial variation of the flow velocity, abbreviated  $E \times B$  shear rate, is related to the zonal potential via

$$\omega_{E \times B} = \frac{1}{B} \frac{\partial^2 \phi_{\text{ZF}}}{\partial \psi^2}. \quad (2.37)$$

## 2.5. Structures in the zonal flow

Recent studies [8–11, 51] describe the appearance of radial structures, so-called ( $E \times B$ ) staircases, in the zonal flow and the corresponding shear. First indications of these structures are found in Ref. [8], where staircases are observed in global gyrokinetic simulations. First indications are found in the non-local/non-diffusive transport behaviour, which stems from an avalanche mediated transport related to the staircase structures, i.e. avalanche like structures strongly dominate the transport in the radial direction but are confined between the staircase flanks. The study in Ref. [9] further investigates this topic and shows first experimental indications of these structures in the Tore Supra tokamak [52]. In Ref. [10], a comparison of gradient and flux driven simulations leads to the observation of staircases in local simulations and first indications of the turbulent threshold are found. The analysis of Ref. [11] detailed the influence of the staircase structures on the threshold of the ITG turbulence. It was found that the emergence of  $E \times B$  staircases coincides with a further up-shift of the turbulence threshold, the so-called finite heat flux threshold. This threshold also differs from the nonlinear threshold in a qualitatively different behaviour of the heat flux as a function of the temperature

## 2. Plasmas and Tokamaks

gradient. Whereas the heat flux goes smoothly to zero at the nonlinear threshold, the heat flux has a finite value up to the finite heat flux threshold, where a jump to zero is observed.

$E \times B$  staircases are characterized by distinct forms in the  $E \times B$  shear  $\omega_{E \times B}$  and corresponding quantities as show in Fig. 2.12. Their exact form is found to be dependent

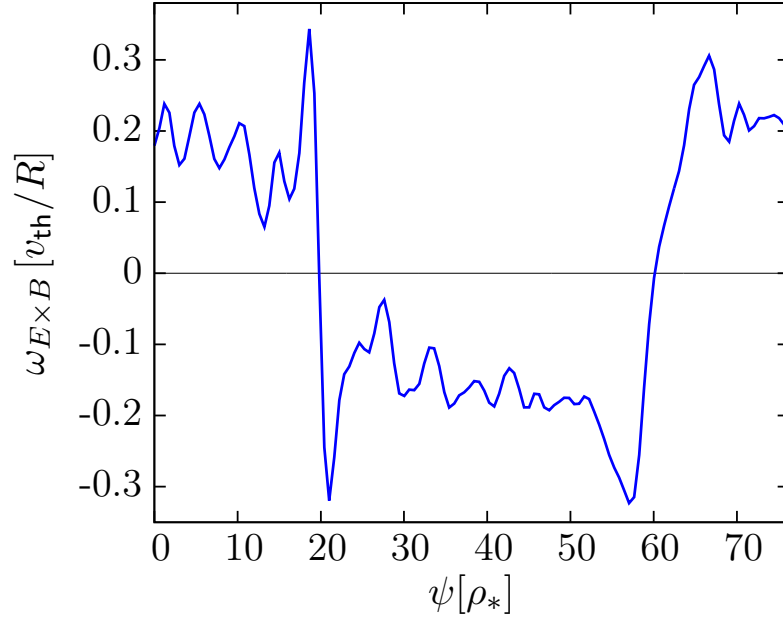


Figure 2.12.: Example of a (fully developed) staircase structure in  $\omega_{E \times B}$  (in gradient driven simulations).

on the type of the simulation. For flux-driven local simulations (see Chap. 3), triangular shaped structures are found. Gradient-driven simulations, as in the case of Fig. 2.12, exhibit box-shaped structures, which are generally more distinct than in flux-driven simulations. Here, a correlation between a partial opening of the box-shape and a decreased suppression of turbulence can be observed. In global simulations, “valley”-like structures in the shear are observed [51]. The appearance of staircases leads to an ordering of the turbulence on the mesoscale in the radial direction: Transport avalanches are found in the heat flux. They mostly originate at distinct radial positions correlated with the staircase structure and propagate up to the barriers formed by the staircases. This leads to transport barriers that hinder long scale avalanches, effectively reducing transport. Furthermore, the distinct staircase structure allows a high shear over most of the radial domain, best seen in gradient driven simulations, which allows to fulfil the Waltz rule (Eq. (2.36)) effectively.

## 2.6. Collisions

Collisions between particles in a plasma can have an impact on the quality of the confinement. As particles in a plasma are charged, one could handle all interactions between them using the Coulomb force for a particle-particle interaction (neglecting electromagnetic influences). However it is convenient to split the treatment into a macroscopic and microscopic part, where a rough threshold length is given by the Debye length [12]. The macroscopic treatment governs large scale movements, i.e. drifts etc., using collectively calculated fields and their influence on the particles as described above. The microscopic treatment governs the particle's interactions on a small scale, dubbing these interactions collisions. This separation allows a sensible analytic and numerical treatment.

Collisions are relatively scarce in most of the plasma and can sometimes be neglected, nonetheless they often do play a crucial role. A prominent example of such a case is the bootstrap current, a pressure driven current closely related to the collisional coupling of trapped and passing particles [53]. Another notable example is the damping of the zonal flow due to collisions [32, 34], which is investigated in this thesis.



## 3. Simulating Plasma

This chapter presents the gyro-kinetic model, which is used to describe small scale turbulence in a Tokamak fusion reactor's plasma in this thesis. It also details on the implementation of this model into the code GWK (Gyro-Kinetic Workshop) [54], the code used throughout this thesis. Sec. 3.1 presents an overview of the gyro-kinetic model. The adiabatic electron response, a widely used approximation of the electron dynamics, is discussed in Sec. 3.2. The description of the non-trivial field line geometry of a Tokamak is discussed in Sec. 3.3. The spectral treatment of this system is touched upon in Sec. 3.4. Sec. 3.5 gives details on the employed simulation domains. Sec. 3.6 concludes with details specific to GWK, in particular its gyro-kinetic equation.

### 3.1. Gyro-kinetics

A typical reactor plasma consists of about  $10^{22}$  particles<sup>1</sup>, which is vastly out of scope for an individual particle description / simulation [30]. Therefore, reduced physical models are used, the choice depending on the physical effects that are examined. This thesis focuses on the investigation of turbulence, which has typical length scales comparable to the ion Larmor radius, i.e. of  $\sim 10^{-3}\text{m}$  to  $\sim 10^{-2}\text{m}$ . Typical timescales are of the order of the ion transit time which is  $R/v_{\text{th}} \approx 10^{-5}\text{s}$ . For a conclusive description of the turbulence, it is required to follow the evolution of many turbulent structures over a considerable time ( $\sim 10^{-4}\text{s}$  to  $\sim 10^{-3}\text{s}$ ). This means length scales of  $\sim 100$  Larmor radii perpendicular to the magnetic field. Furthermore, parallel to the field, the dynamic is fast and the whole field line (several meters) has to be considered. Thus the description of turbulence involves a vast range of spatio-temporal scales. Consequently, a simulation requires a sophisticated model to keep the computational resources at a manageable amount, while at the same time retaining the defining physical characteristics of the system. This is achieved with the gyro-kinetic model, which will be briefly presented in the following, reviews of this topic can be found for example in Refs. [30, 56, 57].

#### 3.1.1. Kinetic description of a plasma

As the vast amount of particles does not enable a feasible description of a plasma as individual particles, a kinetic- or a fluid-model has to be used instead. The (simplest) fluid model, magnetohydrodynamics (MHD), does not allow the description of ITG-turbulence. It does not properly depict the required scales [30]. Also, MHD lacks several features

---

<sup>1</sup>ITER:  $\sim 10^{23}$ , ASDEX Upgrade:  $\sim 10^{21}$ , JET:  $\sim 10^{21}$  [3, 16, 18, 55].

### 3. Simulating Plasma

relevant for (ITG-)turbulence, examples being an energy balance equation or kinetic effects. Consequently, for the tasks of this thesis, a kinetic model has to be chosen. Therein, the plasma is described via a particle density distribution function  $f_p(\mathbf{x}, \mathbf{v})$  in phase space, the space spanned by the possible degrees of freedom, here the position  $\mathbf{x}$  and the velocity  $\mathbf{v}$ .  $f_p$  describes the density of particles in phase space:

$$N = \int \int f_p d\mathbf{v} d\mathbf{x}, \quad (3.1)$$

where  $N$  denotes the total number of particles. The distribution function is evolved in time via the Vlasov equation:

$$\frac{\partial f_p}{\partial t} + \{f_p, H_p\} = \frac{\partial f_p}{\partial t} + \frac{d\mathbf{x}}{dt} \cdot \frac{\partial f_p}{\partial \mathbf{x}} + \frac{d\mathbf{v}}{dt} \cdot \frac{\partial f_p}{\partial \mathbf{v}} = 0, \quad (3.2)$$

where  $H_p$  is the Hamiltonian and the curly brackets denote the Poisson-bracket. This leads to a reduced description of the many particle system, as the particles are uncorrelated. As a plasma consists of charged particles, the interactions between particles are assumed to be electromagnetic. They are split into short range, particle-particle-interactions and long range interactions through a “smoothed out” electric and magnetic field (see Sec. 2.6). The short range interactions are described with a collision operator at the r. h. s of Eq. (3.2). Then, the evolution of the distribution function of a species  $s$  due to collisions with the species  $S'$  is governed by

$$\frac{\partial f_{p,s}}{\partial t} + \{f_{p,s}, H_{p,s}\} = C(f_{p,s}, f'_{p,s}). \quad (3.3)$$

Using the Maxwell equations to calculate the electric and magnetic fields and considering the Lorentz force, it is possible to describe the long range interactions. The combination of Eq. (3.2) and the Maxwell equations forms the Vlasov-Maxwell system, which is used to describe a plasma. However, to describe turbulence in a (reactor) plasma, it is beneficial to use characteristic properties of such a plasma, which lead to a further reduction of the description.

#### 3.1.2. Gyro-kinetic ordering

In the turbulence of Tokamak fusion reactor’s plasma, a characteristic separation of spatial and temporal scales is observed. The presence of a strong magnetic field leads to a gyro-motion with a Larmor radius  $\rho_i \approx 10^{-3} \dots 10^{-2}\text{m}$ , which is small compared to the device size ( $\sim 1 \dots 10\text{m}$ ) and related characteristic length scales, for example the density gradient length  $L_n = 1/|\nabla n|$ . However, the length scales of turbulence can be comparable to  $\rho_i$ , which requires one to cover these length scales for a physically correction description of plasma turbulence. The time scale of the gyro-motion  $1/\Omega_{i,e} \approx 10^{-8}\text{s}$  is smaller than times characteristic for turbulence, which evolves on the transit or Alfvén time scale  $a/v_A \approx 10^{-6}\text{s} < 1/\omega_{\text{turb}} < R/v_{\text{th}} \approx 10^{-5}\text{s}$ . Therefore, it is not a necessity to cover time scales comparable to  $1/\Omega_{i,e}$  to describe turbulence. Furthermore, perturbation of

plasma quantities (like the perturbed density  $\delta n$ ) can be considered small compared to their background (background density  $n_0$ ). Similar assumptions can be made for the fields (for example the perturbed magnetic field  $B_1$  and the background magnetic field  $B_0$ ). The strong magnetic background field introduces a characteristic anisotropy in to a Tokamak plasma: The particle velocity perpendicular to a field line (caused by drifts  $v_d$ ) is small compared to the velocity along the field line  $v_{th}$ . Consequently, quantities exhibit strong variations in the direction perpendicular to a field line ( $\nabla_{\perp}, k_{\perp}$ ) compared to the variation along the field line ( $\nabla_{\parallel}, k_{\parallel}$ ). This ordering can be summarized (see for example Ref. [30]):

$$1 \gg \frac{\rho_i}{L_n} \sim \frac{\omega_{\text{turb}}}{\Omega_i} \sim \frac{\delta n}{n_0} \sim \frac{B_1}{B_0} \sim \frac{v_d}{v_{th}} \sim \frac{\nabla_{\parallel}}{\nabla_{\perp}} \sim \frac{k_{\parallel}}{k_{\perp}} \sim \varepsilon_g, \quad (3.4)$$

where it is assumed that all smallness-relations are comparable which is related to a smallness parameter  $\varepsilon_g$ . Taking advantage of this ordering allows a much more efficient use of computational resources.

### 3.1.3. The gyro-kinetic transform

To use the aforementioned separation of scales, the gyro-centre transform is employed on the kinetic model. This transform is best motivated in guiding-centre coordinates (see for example Ref. [58] and references therein), which takes advantage of the gyro-motion. Here the position of a particle in six dimensional phase space is defined in relation to the position of its gyro-centre with spatial coordinates  $\mathbf{X}$  in conjunction with the velocity parallel to the magnetic field  $v_{\parallel}$  and the magnetic moment  $\mu = m_s v_{\perp}^2 / 2B_0$  of the gyration. The actual position of the particle is determined with the gyro-phase-angle  $\zeta$ . As argued above, the time scale of the gyro-motion is small compared to time scales relevant for turbulence. Therefore, one can “average out” the gyro-motion, which is done with the so-called gyro-centre transform [59, 60], sketched in Fig. 3.1. It eliminates the

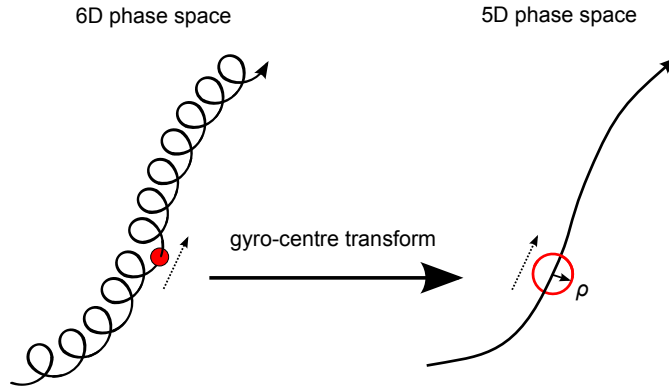


Figure 3.1.: Schematic presentation of the gyro-centre transform.

fast gyro-motion and further high-frequency phenomena while retaining essential kinetic

### 3. Simulating Plasma

effects that are required to describe turbulence. This allows to increase the time step of a simulation which saves computational resources. Also, the dimensionality of the problem is reduced as the dependence on the gyro-phase-angle  $\zeta$  is removed. However, as typical length scales of the turbulence are comparable to the scale of the Larmor-radius, this variation of the fields on this scale has to be accounted for in the averaging process to allow a correct investigation of plasma turbulence. The gyro-centre transform is based on a Hamiltonian formalism with Lie perturbation theory [61] and it requires that the perturbation of the treated quantities are small (as shown with  $\varepsilon_g$  in Eq. (3.4)). A rigorous derivation of the gyro-centre transform can be found in Ref. [56]. This transformation ensures that the Hamilton structure of the system is kept, which retains the conservation properties of the Vlasov-Maxwell system. Formally it represents a transformation from standard phase space coordinates over guiding-centre coordinates to the position of the gyro-centre:

$$(\mathbf{x}, \mathbf{v}) \rightarrow (\mathbf{X}, v_{\parallel}, \mu, \zeta) \rightarrow (\mathbf{X}, v_{\parallel}, \mu). \quad (3.5)$$

#### 3.1.4. The gyro-kinetic equation

Applying the gyro-centre transform on the Vlasov equation (Eq. (3.2)) leads to an equation for the evolution of the distribution function of the gyro-centre  $f$ . Taking into account that the gyro-centre magnetic moment is constant  $\dot{\mu} = 0$  [56] and that in gyro-centre phase space the gyro-angle can be neglected, allows to write the (collisionless) gyro-kinetic equation

$$\frac{\partial f}{\partial t} + \frac{d\mathbf{X}}{dt} \cdot \frac{\partial f}{\partial \mathbf{X}} + \frac{dv_{\parallel}}{dt} \frac{\partial f}{\partial v_{\parallel}} = 0. \quad (3.6)$$

The second term can be expanded to

$$\frac{d\mathbf{X}}{dt} = v_{\parallel} \mathbf{b} + \mathbf{v}_E + \mathbf{v}_D, \quad (3.7)$$

where  $\mathbf{b}$  denotes the unit vector along the magnetic field. It describes the motion along the field line, the motion due to the  $E \times B$  drift and the combined  $\nabla B$  and curvature drift. The third term in Eq. (3.6) can be evaluated using the relation

$$\frac{dv_{\parallel}}{dt} = -\frac{1}{mv_{\parallel}} \frac{d\mathbf{X}}{dt} \cdot (\mu \nabla B + Ze \nabla \langle \phi \rangle), \quad (3.8)$$

which models the influence of an inhomogeneous magnetic and electric field.

To calculate the electromagnetic fields, the gyro-kinetic Poisson and Ampère equations are required. In a plasma, no large electric fields are present (on the scales relevant for gyro-kinetics), therefore not the Poisson equation, but the quasineutrality constraint

$$\sum_s Z_s n_s(\mathbf{x}) = 0 \quad (3.9)$$

is considered. This requires the species particle density  $n_s(\mathbf{x})$  (in particle phase space), which has to be obtained from  $f_s$ , the gyro-centre distribution function by inverting the gyro-centre transform with the operator  $\mathcal{T}$  averaged over the gyro-angle (denoted with angle brackets):

$$0 = -2\pi B \sum_s q_s \int dv_{\parallel} \int d\mu \langle \mathcal{T} f_s \rangle = - (e(\bar{n}_i - \bar{n}_e) + \rho_{\text{pol}}) = -(\bar{\rho} + \rho_{\text{pol}}), \quad (3.10)$$

with the gyro-centre densities  $\bar{n}_s$ . The polarization density  $\rho_{\text{pol}}$  is used to describe the difference (at a point in real space) between the actual charge density and the charge density of the gyro-centres  $\bar{\rho}$ :

$$\rho_{\text{pol}}(\mathbf{X}) = 2\pi B \sum_s q_s \int dv_{\parallel} \int d\mu (\langle \mathcal{T} f_s \rangle(\mathbf{X}) - f_s(\mathbf{X})) \propto \phi(\mathbf{x}) - \langle \phi \rangle(\mathbf{X}). \quad (3.11)$$

Ampère's law requires a similar treatment:

$$\nabla^2 A_{\parallel} = 2\pi B \sum_s Z_s \int dv_{\parallel} \int d\mu \langle \mathbf{v} \mathcal{T} f_s \rangle. \quad (3.12)$$

The gyro-kinetic equation and the accompanying field equations in the form in which they are implemented in GKW are found in Sec. 3.6.1.

## 3.2. Adiabatic electron response

Due to their lower mass, the electrons move rapidly along the magnetic field lines. on the time scale of the ion dynamics, the movement of the electrons traces out the flux surface, resulting in an almost constant electron temperature on the surface and a density response that is only connected to the electric field [6]. This allows the approximation of the electron dynamics with the so-called adiabatic electron response / limit, which is sufficient for many numerical experiments. In that case, only the ion dynamics are simulated, whereas the electrons of the plasma are not simulated as a kinetic species. Instead, the influence of the electrons is calculated with an analytical expression, which leads to a large reduction of computational resources. The main reason is that, as ions have a smaller thermal velocity than electrons, the simulation of the ions in the adiabatic electron limit allows a larger time step to satisfy the Courant-Friedrichs-Lewy condition [62] (the condition that particles / perturbations have to move less than the grid width within a time step). The relation of the thermal velocities of both species (protons/electrons) is

$$\frac{v_{\text{th},e}}{v_{\text{th},i}} = \sqrt{\frac{m_i}{m_e}} \approx 43, \quad (3.13)$$

so a significant reduction is possible, when the explicit simulation of electrons can be omitted. The adiabatic electron response is often abbreviated as “adiabatic electrons”, whereas the explicit simulation of electrons as a kinetic species is abbreviated as “kinetic electrons”.

### 3.3. Field aligned coordinates and background magnetic field configuration

Here, the field aligned coordinates used by GKW, the Hamada coordinates [63, 64], are presented. Also an overview of the models to describe the equilibrium magnetic field, called geometries, is given.

#### 3.3.1. Hamada Coordinates

It is easily understood that using coordinates which are aligned with the magnetic field holds many benefits for the simulation of a tokamak plasma. Most quantities show only a small variation along the direction of the magnetic field, whereas a strong variation is found perpendicular to the field. Consequently, if the coordinate grid is aligned with the magnetic field, for nearly all problems, along the field a coarser resolution can be employed, strongly reducing the computational cost [65]. As the form of the magnetic field in a tokamak fusion reactor is winding helically, as shown in Fig. 3.2, the chosen coordinates are not trivial. The so-called (field aligned) Hamada coordinates [63, 64]

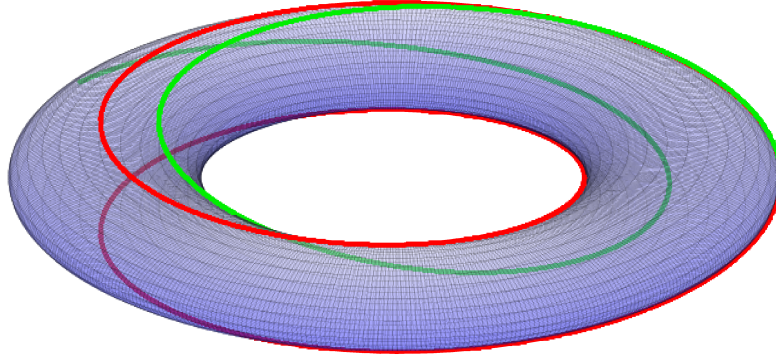


Figure 3.2.: Flux surface (blue) and magnetic field lines with  $q = 1,4$  (green) and  $q = 2.0$  (red).

are used in GKW. Their features are straight magnetic field lines and also straight current-density lines [66], where the coordinates are aligned with the magnetic field lines.

Here, a brief overview of the required transformation to obtain the coordinates shall be given. For this transformation, it is required that the magnetic field is known. One starts with an orthogonal toroidal coordinate system  $(\psi, \theta, \varphi)$ , sketched in Fig. 3.3. Here,  $\psi$  is the radial coordinate (direction of the minor radius) and taken as a label for flux surfaces, so that

$$\mathbf{B} \cdot \nabla \psi = 0 \quad (3.14)$$

holds. The major radius is denoted with  $R$  and  $\psi = 0$  is located at  $R_{\text{ref}}$ .  $\theta$  denotes the poloidal angle and  $\varphi$  denotes the toroidal angle. The transform is split into two parts, the

### 3.3. Field aligned coordinates and background magnetic field configuration

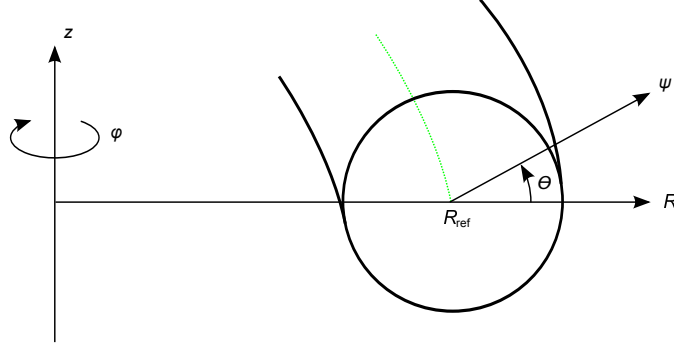


Figure 3.3.: Schematic of the initially used toroidal coordinates.

first obtaining straight magnetic field lines and the second part aligning the coordinates with the magnetic field lines. With the intermediate coordinates it reads

$$(\psi, \theta, \varphi) \rightarrow (\psi, s, \gamma) \rightarrow (\psi, \zeta, s), \quad (3.15)$$

where  $\zeta$  labels magnetic field lines on a flux surface and  $s$  parametrizes the magnetic field line,  $\gamma$  being a subsidiary coordinate.

The first part of the transformation is motivated in the sketch shown in Fig. 3.4. Starting

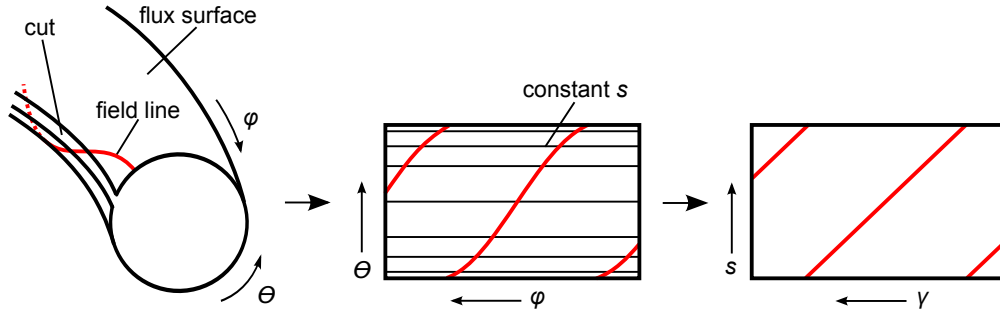


Figure 3.4.: Schematic of the initial part of the transformation, which straightens the field lines. The radial coordinate is going outwards in the left picture and out of the drawing plane on the others.

with a flux surface of a torus (left), a surface which is equivalent if correct boundary conditions are taken, can be found (middle). In this surface, the magnetic field lines wiggle due to the curvature on a torus in the  $(\psi, \theta, \varphi)$  system (Eq. (3.14) still holds). To compensate this, new coordinates  $(\psi, s, \gamma)$  are introduced. In that system, the field lines are straight, as shown in the rightmost surface of Fig. 3.4. To construct the transformation, one starts with the magnetic field written in terms of its contravariant components

$$\mathbf{B} = s_B R B_t \nabla \varphi + \nabla \varphi \times \nabla \Psi, \quad (3.16)$$

### 3. Simulating Plasma

where  $\Psi$ , the poloidal flux with  $\psi = \psi(\Psi)$ , is used for generality and  $s_B$  denotes the sign of  $B$ . For the new coordinates it is required that

$$s(\psi, \theta), \quad \gamma(\psi, \theta, \varphi). \quad (3.17)$$

The requirement that the field lines are straight, i.e. that

$$\frac{B^\gamma}{B^s} = \text{const.} \quad (3.18)$$

for any fixed  $\psi$ , can be achieved if the contravariant components of the magnetic field are flux functions

$$B^s = B^s(\psi), \quad B^\gamma = B^\gamma(\psi). \quad (3.19)$$

Requiring toroidal symmetry and Eq. (3.14) leads to

$$B^s = \mathbf{B} \cdot \nabla s = \mathbf{B} \cdot \nabla \theta \frac{\partial s}{\partial \theta}. \quad (3.20)$$

Integrating in  $\theta$  and using that  $B^s = B^s(\psi)$  yields

$$s = B^s \int \frac{1}{\mathbf{B} \cdot \nabla \theta} d\theta. \quad (3.21)$$

Constraining  $s$  to the domain  $[-1/2, 1/2]$  as one poloidal turn

$$1 = \oint \frac{\partial s}{\partial \theta} d\theta \quad (3.22)$$

gives

$$B^s = 1 \left/ \oint \frac{1}{\mathbf{B} \cdot \nabla \theta} d\theta, \quad (3.23)$$

resulting in the expression for  $s$

$$s = s(\psi, \theta) = \int_0^\theta \frac{d\theta'}{\mathbf{B} \cdot \nabla \theta'} \left/ \oint \frac{d\theta'}{\mathbf{B} \cdot \nabla \theta'}. \quad (3.24)$$

To obtain  $\gamma$ , one starts with a subsidiary function  $g(\theta, \psi)$

$$\gamma = \frac{\varphi}{2\pi} + g, \quad (3.25)$$

so that  $\gamma \in [0, 1]$  corresponds to a toroidal turn. Here

$$B^\gamma = \frac{s_B B_\varphi}{2\pi R} + \mathbf{B} \cdot \nabla \theta \frac{\partial g}{\partial \theta} \quad (3.26)$$

### 3.3. Field aligned coordinates and background magnetic field configuration

gives the contravariant component of the magnetic field along  $\gamma$ . This allows to determine  $g$ :

$$g = \int_0^\theta \frac{d\theta'}{\mathbf{B} \cdot \nabla\theta'} \left[ B^\gamma - \frac{s_B B_\varphi}{2\pi R} \right]. \quad (3.27)$$

$B^\gamma$  can be determined through the periodicity of  $g$

$$0 = \oint \frac{d\theta'}{\mathbf{B} \cdot \nabla\theta'} \left[ B^\gamma - \frac{s_B B_\varphi}{2\pi R} \right], \quad (3.28)$$

which results in

$$B^\gamma = \left\{ \frac{s_B B_\varphi}{2\pi R} \right\}, \quad (3.29)$$

where the curly brackets denote the flux surface average. Taking into account that  $B_\varphi \propto 1/R$  leads to

$$\gamma(\psi, \theta, \varphi) = \gamma(\psi, \theta, \varphi) = \frac{\varphi}{2\pi} + s_B \frac{RB_t}{2\pi} \int_0^\theta \frac{d\theta'}{\mathbf{B} \cdot \nabla\theta'} \left[ \left\{ \frac{1}{R^2} \right\} - \frac{1}{R^2} \right], \quad (3.30)$$

which completes the first transformation.

The result of the second transformation to align the coordinates with the magnetic field lines is sketched in Fig.3.5. This is done via the transformation

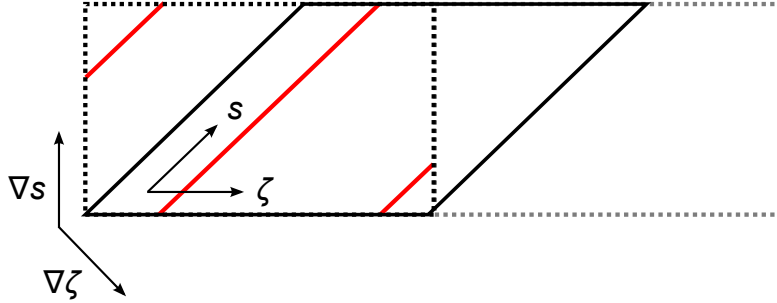


Figure 3.5.: Aligning the coordinates with the magnetic field lines leads to a non-orthogonal coordinate system. The toroidal angle is flipped, so that the coordinate system can be defined as  $(\psi, \zeta, s)$ .

$$\zeta = qs - \gamma, \quad (3.31)$$

where  $q$  is the safety factor  $q = B^\gamma/B^s$ . This transform changes the sign of the toroidal angle, so that the coordinate system can be defined with  $(\psi, \zeta, s)$  as a right handed coordinate system. A relatively extensive treatment of this transformation and some possible caveats are discussed in Refs. [67, 68].

### 3. Simulating Plasma

#### 3.3.2. Background magnetic field configuration

To simulate a plasma while using the coordinates described above, the shape of the background magnetic field has to be specified. Several models, in this context called geometries, can be employed to describe the background field. The shape of the field is determined by the force balance. For a toroidally symmetric system, this equilibrium configuration is described by the Grad-Shafranov equation [69, 70]. It can be solved, for example, with the equilibrium solver code CHEASE [71] and subsequently fed to into GKW. However, the exact geometry of the magnetic field can be cumbersome in an analytical or numerical analysis and therefore several approximations exist.

One of the most common geometries for an axisymmetric tokamak is the so-called  $s - \alpha$  geometry. It is a simplified model where the flux surfaces are taken to be circular and concentric. Furthermore, it is the model approximating the Grad-Shafranov-equilibrium in the lowest order of the inverse aspect ratio  $\epsilon$ . The variation in the first order of  $\epsilon$  is kept only in the amplitude of the magnetic field itself, in all other quantities the dependence is neglected. Consequently, this model is only valid for a large aspect ratio tokamak ( $\epsilon \rightarrow 0$ ). It can be seen as the crudest model that still reproduces trapping effects. Nevertheless it holds significance at present due to its vast prevalence in the scientific field.

The model that will be referred to as “circular geometry” fixes the aforementioned problems because it retains the modulation of the magnetic field in all geometric quantities. In this model, again circular concentric flux surfaces are assumed, leading to a deviation from the exact equilibrium obtained through the Grad-Shafranov-equation. This assumption of circular concentric flux surfaces is valid for small  $\epsilon$  and low plasma- $\beta$ , allowing to neglect poloidal variations of the flux surface  $\propto \epsilon^2$  or the Shafranov-shift (the displacement of the flux surface’s centre) [72]. However, as all orders of  $\epsilon$  are kept in the derivation of the circular geometry, a completely consistent description of the geometry is ensured in this model, which is the important factor for the analysis of many effects. It proves to be sufficient for the problems studied in the scope of this thesis [73]. The field aligned coordinates are given with Eq. (3.24) as

$$s = \frac{1}{2\pi}(\theta + \epsilon \sin \theta) \quad (3.32)$$

and with Eq. (3.30) and Eq. (3.31) as

$$\zeta = -\frac{\varphi}{2\pi} + \frac{q}{\pi} \arctan \left[ \sqrt{\frac{1-\epsilon}{1+\epsilon}} \tan \frac{\theta}{2} \right]. \quad (3.33)$$

As radial coordinate, the minor radius of the flux surface is used. The deficits of the  $s - \alpha$  model compared with the circular model do have significant influences on the obtained results, however they are mostly quantitative. An in-depth comparison of both models and their influence on turbulence analysis can be found in Ref. [73]. Relevant for this thesis, Ref. [11] shows the differences of the obtained heat flux in the  $s - \alpha$  and the circular geometry.

### 3.4. Spectral representation

Due to the symmetries of a torus, a spectral representation of the quantities proves to be beneficial. Here, the term spectral is used in the sense that the relevant quantities, for example the distribution function, are Fourier transformed in a designated direction. Instead of examining the quantities on a grid in real space, the Fourier coefficients of the quantities, dubbed modes, are used in the code. This leads to an increase in efficiency, as the finite difference scheme required for a derivative can be replaced by a multiplication with the corresponding wave vector, which saves the memory access to the quantities' adjacent grid points. In all cases, GWK treats the binormal direction spectrally and the direction along the magnetic field non-spectral. The treatment of the radial direction can be chosen, with the choice depending on what radial domain is used and on the physical problem that is examined. Due to the available choices, the adverb ‘‘radially’’ will be omitted in the following. The distribution function is represented by a sum of Fourier modes:

$$f(\psi, \zeta, s) = \sum_{k_\zeta k_\psi} \hat{f}(k_\psi, k_\zeta, s) \exp[ik_\zeta \zeta / \rho_* + ik_\psi \psi / \rho_*]. \quad (3.34)$$

As  $f(\psi, \zeta, s)$  is a real quantity, the amplitude of the mode with  $(k_\psi, k_\zeta)$  must equal the complex conjugate of the amplitude of the mode  $(-k_\psi, -k_\zeta)$ . This can be exploited by limiting the sum to positive wave vectors. For the numerical treatment with GWK one limits  $k_\zeta \geq 0$  to be compliant to common FFT routines [74]. It results in

$$\begin{aligned} f(\psi, \zeta, s) = & \\ & \sum_{k_\zeta > 0, k_\psi} \left[ \hat{f}(k_\psi, k_\zeta, s) \exp[ik_\zeta \zeta / \rho_* + ik_\psi \psi / \rho_*] + \hat{f}^\dagger(k_\psi, k_\zeta, s) \exp[-ik_\zeta \zeta / \rho_* - ik_\psi \psi / \rho_*] \right] \\ & + \sum_{k_\zeta = 0, k_\psi} \hat{f}(k_\psi, k_\zeta = 0, s) \exp[ik_\psi \psi / \rho_*]. \end{aligned} \quad (3.35)$$

### 3.5. Simulation domains in a Tokamak

For the simulation of the (turbulent) plasma in a Tokamak, several types of simulation domains can be used. In the scope of this thesis two options are used: simulations on the flux-tube domain and simulations on the global domain.

#### 3.5.1. Flux-tube simulation

The flux-tube domain represents a radially thin tube confined by flux-surfaces. When this domain is used, it is assumed that key features of the desired plasma behaviour have a small radial extend compared to the system size or the length scales of background

### 3. Simulating Plasma

quantities. This is often given for turbulence (far from the edge), as discussed in the gyro-kinetic ordering in Sec. 3.1.2. Therefore a radially small simulation domain can be used and the variation of the background quantities in the radial direction can be neglected. As a consequence, the turbulence is taken to be homogeneous, which allows the use of periodic boundary conditions. These boundary conditions also require a statistical assumption, as it is assumed that the turbulence in the simulation domain is (exactly) similar to the one in the adjacent domain. This assumption can lead to unphysical effects that overestimate the correlation, as turbulence can be homogeneous but not necessarily correlated over longer distances. To prevent these effects, it must be ensured that the correlation length of the turbulence is smaller than the size of the simulation domain [65]. The small radial extent leads to the assumption of the local limit. Here, the set of normalized equations becomes independent of  $\rho_*$ . Flux-tube simulations lead to a reduction in the required computational resources. Beside the obvious reduction due to a smaller domain size, several factors come into play. Due to the constant background quantities and the assumption of homogeneous turbulence, it is possible to treat the radial direction spectrally. This leads to a decrease in computation costs, because the finite difference scheme representing a derivative can be replaced by an analytic expression, as described in Sec. 3.4. Due to the toroidal symmetry, the spectral representation alongside of periodic boundary conditions is used in the binormal direction (not limited to the flux-tube domain). As one can assume that the turbulence is homogeneous in the binormal direction, the domain can be restricted. Again, care has to be taken, not to overestimate the correlation in the binormal direction. As a result, instead of the full torus, only a thin quadrilateral tube is simulated, for clarification a sketch is shown in Fig. 3.6.

Due to the helical winding of the flux-tube, part of the boundary conditions become

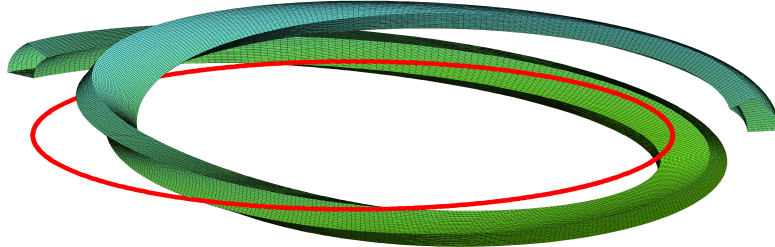


Figure 3.6.: Sketch of a flux tube domain in a torus with  $q = 1.4$ . The magnetic axis is indicated in red.

non-trivial. In the radial direction, periodic boundary conditions apply to a quantity  $f$

$$f(\psi + l, \zeta, s) = f(\psi, \zeta, s) \quad (3.36)$$

for a box of length  $l$ . Similarly in the binormal direction, the condition of toroidal periodicity is formulated:

$$f(\psi, \zeta + 1, s) = f(\psi, \zeta, s), \quad (3.37)$$

### 3.5. Simulation domains in a Tokamak

here, the box is normalized to unity. When using Fourier harmonics (Sec. 3.4), this leads to the following condition for the smallest (non-zero) binormal wave vector  $k^{\min}$ :

$$\frac{k_{\zeta}^{\min}}{\rho_*} = 2\pi N, \quad (3.38)$$

where  $N$  denotes an integer.  $1/N$  can be interpreted as the fraction of the poloidal domain that is covered by the simulation. Due to the smallness of  $\rho_*$ , the constraint can be satisfied with very small changes in  $\rho_*$  or  $k_{\zeta}$ . Because the equations are independent of  $\rho_*$  in the local limit, the periodicity constraint is satisfied. In the  $s$  direction, assuming  $s = 0$  to be located at the outboard mid plane, the helical winding has to be accounted for:

$$f(\psi, \zeta + q/2, 1/2) = f(\psi, \zeta - q/2, -1/2). \quad (3.39)$$

In the case of a spectral simulation this leads to

$$\begin{aligned} \sum_k \hat{f}(k_{\psi}, k_{\zeta}, 1/2) \exp\left[i\left(\frac{k_{\psi}\psi}{\rho_*} + \frac{k_{\zeta}\zeta}{\rho_*} + \frac{qk_{\zeta}}{2\rho_*}\right)\right] + c.c. = \\ \sum_k \hat{f}(k_{\psi}, k_{\zeta}, -1/2) \exp\left[i\left(\frac{k_{\psi}\psi}{\rho_*} + \frac{k_{\zeta}\zeta}{\rho_*} - \frac{qk_{\zeta}}{2\rho_*}\right)\right] + c.c. \end{aligned} \quad (3.40)$$

With an expansion of  $q$  up to first order at a reference value  $q_0$  taken at the centre of the radial domain

$$q(\psi) \approx q_0 + \frac{\partial q}{\partial \psi} \Big|_0 \psi, \quad (3.41)$$

and the magnetic shear (Eq. (2.13)) the boundary condition becomes

$$\hat{f}(k_{\psi}, k_{\zeta}, 1/2) = \hat{f}(k_{\psi} + k_{\zeta} \hat{s} q/r, k_{\zeta}, -1/2). \quad (3.42)$$

This formulation is close to the so-called ballooning transform [75–77] and leads to a connection between the radial and the binormal modes. As it is generally desired to have the mode to which the reconnection takes place to be in the grid, a constraint for the spacing of the modes is generated.

#### 3.5.2. Global simulation

The arguments for the use of flux-tube simulations are consistent with the gyro-kinetic ordering, however their validity depends on the smallness of  $\rho_*$ . For a comprehensive description of turbulence, domains with a larger extend are required, which can invalidate the assumption of constant background quantities if  $\rho_*$  is not small. In such a case, a so-called global simulation domain is used, where the background quantities are not assumed to be constant and instead, profiles are specified or are taken from experimental data. Furthermore, the periodicity in the radial direction is dropped and boundary conditions at both sides have to be given, where generally, Dirichlet boundary conditions are chosen. Due to these restrictions, the radial direction can only be treated non-spectrally.

### 3. Simulating Plasma

However the binormal direction is still treated spectrally and the aforementioned boundary conditions, Eq. (3.37), apply. In the direction along the magnetic field, the boundary conditions, Eq. (3.39), lead to a phase factor

$$\hat{f}(\psi, k_\zeta, 1/2) = \hat{f}(\psi, k_\zeta, -1/2) \exp(2\pi i q(\psi) k_\zeta). \quad (3.43)$$

In general, these simulations become computationally much more demanding than flux-tube simulations.

## 3.6. Gyro-Kinetic Workshop (GKW)

In this section, several of the less general aspects of the nonlinear Eulerian gyro-kinetic code GKW, i.e. the gyro-kinetic equation, the normalization of GKW, the implementation of the finite-difference scheme and the collision operator are presented. More details on these topics can be found in Ref. [78].

### 3.6.1. Gyro-kinetic equation of GKW

Here, a brief overview of the gyro-kinetic equation and the corresponding field equations that are implemented in GKW is given. The tedious derivation of these equations will not be repeated here, but it can be found in Refs. [30, 56]. To obtain the gyro-kinetic equation in the form in which it will be solved in GKW, the gyro-centre transform is applied to the Poisson-bracket in Eq. (3.2), which is expanded in its individual contributions, i.e. in the drifts described in Chap. 2 and further contributions and is employed in a co-moving frame, i.e. a frame of reference moving along with the plasma bulk rotation. Furthermore, following from the gyro-kinetic ordering (Eq. (3.4)), the distribution function is split in a background part and a perturbed part  $\delta f$ . For the background, a Maxwellian distribution  $F_M$  is assumed:

$$F_M = \frac{n_{R_0}}{\pi^{3/2} v_{\text{th}}^3} \exp \left[ -\frac{(v_{\parallel} - (RB_t/B)\omega_\phi)^2 + 2\mu B/m}{v_{\text{th}}^2} - \mathcal{E}_\Omega/T \right], \quad (3.44)$$

where  $n_{R_0}$  is the reference density at the middle of the radial domain,  $\omega_\phi$  is the plasma rotation and  $\mathcal{E}_\Omega$  the centrifugal energy (defined in Eq. (3.51)). From the gyro-kinetic ordering it follows that  $\delta f/F_M \sim \rho_*$ , which leads to the so-called  $\delta f$ -approximation, where higher orders in  $\delta f$  are neglected in the nonlinear terms. Solving the field equations requires to address a further problem: The calculation of the electric field requires a time derivative of the magnetic field, and consequently, a time derivative of the vector potential  $A_{\parallel}$ . Therefore, apart from  $\partial f/\partial t$ , an additional time derivative appears in the equation system. To circumvent this problem, the distribution function and the vector potential are merged into a new quantity

$$g = f + \frac{Ze}{T} v_{\parallel} \langle A_{\parallel} \rangle F_M, \quad (3.45)$$

which is evolved in GKW with the gyro-kinetic equation for the electrostatic case [78]

$$\frac{\partial g}{\partial t} + \mathbf{v}_\chi \cdot \nabla g + (v_\parallel \mathbf{b} + \mathbf{v}_D) \cdot \nabla f - \frac{\mathbf{b}}{m} \cdot (\mu \nabla B + \nabla \mathcal{E}_\Omega) \frac{\partial f}{\partial v_\parallel} = S. \quad (3.46)$$

$\mathbf{v}_\chi$  is the combination of the  $E \times B$  drift and the parallel motion along the perturbed magnetic field line:

$$\mathbf{v}_\chi = \frac{\mathbf{b} \times \nabla \chi}{B}, \quad (3.47)$$

where  $\chi$  is the combined field

$$\chi = \langle \phi \rangle - v_\parallel \langle A_\parallel \rangle, \quad (3.48)$$

consisting of the electric potential  $\phi$  and the parallel component of the gyro-averaged vector potential  $\langle A_\parallel \rangle$ . The motion along the unperturbed magnetic field is described with the term  $v_\parallel \mathbf{b} \cdot \nabla f$ . The drift due to the inhomogeneous magnetic field and inertial terms is described with  $\mathbf{v}_D$ , which is given as:

$$\mathbf{v}_D = \frac{1}{Ze} \left[ \frac{mv_\parallel^2}{B} + \mu \right] \frac{\mathbf{B} \times \nabla B}{B^2} + \frac{mv_\parallel^2}{2ZeB} \beta' \mathbf{b} \times \nabla \psi + \frac{2mv_\parallel}{ZeB} \boldsymbol{\Omega}_\perp + \frac{1}{ZeB} \mathbf{b} \times \nabla \mathcal{E}_\Omega. \quad (3.49)$$

The first term represents the  $\nabla B$ - and the curvature drift (see Sec. 2.1 in Chap. 2). The second term is a correction of the curvature drift due to a finite radial pressure gradient  $\partial p / \partial \psi$ , where  $\beta'$  is defined as

$$\beta' = \frac{2\mu_0}{B^2} \frac{\partial p}{\partial \psi}. \quad (3.50)$$

The third term describes the Coriolis drift due to the co-moving frame with  $\boldsymbol{\Omega}_\perp$  denoting the angular rotation vector. The fourth term represents the combined centrifugal drift and influence of the background potential  $\Phi$ . Therefore, the centrifugal energy  $\mathcal{E}_\Omega$  is defined:

$$\mathcal{E}_\Omega = Ze\Phi - \frac{1}{2} m \Omega^2 (R^2 - R_0^2). \quad (3.51)$$

The last two terms in Eq. (3.46) describe the forces along the magnetic field lines due to an inhomogeneous magnetic field, the co-moving frame and  $\Phi$ . The source term is given as

$$\begin{aligned} S = & -(\mathbf{v}_\chi + \mathbf{v}_D) \\ & \cdot \left[ \frac{\nabla n_{R_0}}{n_{R_0}} + \left( \frac{v_\parallel^2}{v_{th}^2} + \frac{(\mu B + \mathcal{E}_\Omega)}{T} - \frac{3}{2} \right) \frac{\nabla T}{T} + \frac{mv_\parallel}{T} \frac{RB_t}{B} \nabla \omega_\phi \right] F_M \\ & - \frac{Ze}{T} [v_\parallel \mathbf{b} + \mathbf{v}_D] \cdot \nabla \langle \phi \rangle F_M. \end{aligned} \quad (3.52)$$

The fields are calculated with the Poisson equation and Ampère's law. The Poisson equation in spectral representation to calculate  $\hat{\phi}$  is

$$\sum_s Z_s n_{R_0,s} \left[ 2\pi B \int dv_\parallel d\mu J_0(k_\perp \rho_s) \hat{g}_s + \frac{Z_s}{T_{Rs}} [\Gamma(b_s) - 1] \exp(-\mathcal{E}_s) \hat{\phi} \right] = 0, \quad (3.53)$$

### 3. Simulating Plasma

with the combined energy

$$\mathcal{E}_s = Ze\langle\Psi\rangle - \frac{m}{2}\Omega_\phi^2(R^2 - R_0^2) \quad (3.54)$$

of the plasma's kinetic rotational energy and the energy of the equilibrium electric field. Eq. (3.53) is in fact a quasi-neutrality equation, as described in Sec. 3.1.4. To reconstruct the charge density in real space from the density distribution function from the gyro-centres, the Bessel function  $J_0(k_\perp\rho_s)$  [79] and the modified Bessel function  $\Gamma(b_s)$  [80] are required in the integral over the distribution function and the polarization of the Maxwell background. The species dependent argument  $b_s$  is defined as

$$b_s = \frac{m_s}{2}T_s k_\theta \rho_* \frac{R_{\text{ref}}}{Z_s B^2}. \quad (3.55)$$

The spectral version of Ampère's law to calculate the vector potential  $A_\parallel$  is

$$\left( k_\perp^2 + \beta \sum_{sp} \frac{Z_{sp}^2 n_{R_0,sp}}{m_{Rsp}} \exp(\mathcal{E}_s) \Gamma(b_{sp}) \right) \hat{A}_\parallel = \beta \sum_{sp} Z_{sp} v_{Rsp} n_{R_0,sp} 2\pi B \int dv_\parallel \int d\mu v_\parallel J_0 \hat{g}_{sp}. \quad (3.56)$$

Similarly to the Poisson equation, the Bessel and the modified Bessel function are required to obtain the current density in real space. The second term of the l. h. s. of Eq. (3.56) is a correction, as the current carried by the unmodified density distribution function  $f$ , and not  $g$ , determines the vector potential.

#### 3.6.2. Normalization

The quantities in the code are normalized with a reference major radius  $R_{\text{ref}}$ , a reference magnetic field,  $B_{\text{ref}}$ , a reference mass  $m_{\text{ref}}$ , a reference thermal velocity  $v_{\text{th,ref}}$ , a reference density  $n_{\text{ref}}$ , a reference temperature  $T_{\text{ref}}$  and a reference Larmor radius  $\rho_{\text{ref}}$ , where

$$T_{\text{ref}} = \frac{m_{\text{ref}}}{2} v_{\text{th,ref}}^2, \quad \rho_{\text{ref}} = \frac{m_{\text{ref}} v_{\text{th,ref}}}{e B_{\text{ref}}} \quad (3.57)$$

holds. They are taken at a reference position in the middle of the simulational domain, except the magnetic field which is taken at the magnetic axis. A dimensionless, normalized Larmor radius is defined as

$$\rho_* = \frac{\rho_{\text{ref}}}{R_{\text{ref}}}. \quad (3.58)$$

With these, it is possible to relate to the dimensionless quantities required by the code as

$$m = m_N m_{\text{ref}}, \quad v_{\text{th}} = v_{\text{th},N} v_{\text{th,ref}}, \quad n = n_N n_{\text{ref}}, \quad T = T_N T_{\text{ref}}, \quad (3.59)$$

### 3.6. Gyro-Kinetic Workshop (GKW)

where  $m$  denotes the physical quantity and  $m_N$  the normalized mass used in the code. Using  $\rho_*$  to ensure that the normalized perturbed quantities are of order of unity,

$$\phi = \rho_* \frac{T_{\text{ref}}}{e} \phi_N, \quad A_{\parallel} = B_{\text{ref}} R_{\text{ref}} \rho_*^2 A_{\parallel N}. \quad (3.60)$$

Consequently, the time is normalized as

$$t = R_{\text{ref}} \frac{t_N}{v_{\text{th,ref}}} \quad (3.61)$$

and the coordinates of the velocity space as

$$v_{\parallel} = v_{\parallel, N} v_{\parallel, \text{ref}}, \quad \mu = \frac{m_{\text{ref}} v_{\text{th,ref}}^2}{B_{\text{ref}}} \mu_N. \quad (3.62)$$

The perturbed distribution function and the background are normalized as

$$f = \rho_* \frac{n_{\text{ref}}}{v_{\text{th,ref}}} f_N, \quad F_M = \frac{n_{\text{ref}}}{v_{\text{th,ref}}} F_{M, N}. \quad (3.63)$$

For the gradient of the temperature and density

$$-\frac{1}{T} \frac{\partial T}{\partial \psi} = \frac{R_{\text{ref}}}{L_T} = \frac{1}{L_{T, N}}, \quad -\frac{1}{n} \frac{\partial n}{\partial \psi} = \frac{R_{\text{ref}}}{L_n} = \frac{1}{L_{n, N}} \quad (3.64)$$

and for the plasma- $\beta$

$$\beta_N = \frac{n_{\text{ref}} T_{\text{ref}}}{B_{\text{ref}}^2 / 2\mu_0}, \quad (3.65)$$

is given. Note that, following common practice, for convenience in this thesis the subscript  $N$  is omitted, except for ambiguous situations.

#### 3.6.3. Implementation

Before the gyro-kinetic equation is implemented in GKW, is brought in a form where the time derivative of the distribution function is set against the terms that represent its evolution. The terms are sorted by their physical meanings, the complete set of equations can be found in Ref. [78]. This has the advantage that it is possible to switch of distinct physical effects. An important case of this is the suppression of all nonlinear terms, allowing a linear stability analysis. It will be called “linear simulation”, whereas the contrary will be called “nonlinear simulation” or “turbulence simulation”.

To implement the gyro-kinetic equation in GKW, a combination of finite-differences schemes and spectral methods is used. As the order of the finite-difference scheme is important for the observations of some effects examined in this thesis, it will be presented

### 3. Simulating Plasma

in more detail. Generally, the fourth order finite-difference scheme is used for derivatives along the field at a grid point at position  $i$  and a velocity  $v$ :

$$v \frac{\partial f}{\partial s} \rightarrow v_i \frac{f_{i-2} - 8f_{i-1} + 8f_{i+1} - f_{i+2}}{12\Delta s} + Dv_d \frac{f_{i-2} - 4f_{i-1} + 6f_i - 4f_{i+1} + f_{i+2}}{12\Delta s}. \quad (3.66)$$

The second term on the r. h. s. is the upwind-dissipation term, with the diffusion parameters  $D$  and  $v_d$ . It is the main source of numerical dissipation, which stabilizes the solution numerically. However, the dissipation can also have an unwanted influence on physical effects if these are susceptible to (numerical) dissipation. This is for example the case in the ‘‘Rosenbluth-Hinton’’-test (see for example Sec. 4.1). Therefore it is often desired to keep the numerical dissipation at a minimum. One way to reduce the numerical dissipation is to increase the number of grid points, however this also increases the required computational resources. To circumvent this, the order of the finite-difference scheme can be increased, which decreases the dissipation. It also increases the required computational resources due to a bigger stencil, i.e. an increased memory access, however, this increase is negligible compared to increase due to a larger grid. A recent study [11] found that the (numerical) dissipation of the zonal flow suppresses the formation of staircases. To reduce the dissipation and allow an investigation of the effect, a sixth order scheme for the zonal mode has been implemented. A derivative along the magnetic field line is calculated with

$$\begin{aligned} v \frac{\partial f}{\partial s} \rightarrow v_i & \frac{-f_{i-3} + 9f_{i-2} - 45f_{i-1} + 45f_{i+1} - 9f_{i+2} + f_{i-3}}{60\Delta s} + \\ Dv_d & \frac{f_{i-3} - 6f_{i-2} + 15f_{i-1} - 20f_{i+1} + 15f_{i+1} - 6f_{i+2} + f_{i-3}}{60\Delta s}. \end{aligned} \quad (3.67)$$

This scheme allows the investigation of zonal flow structure formation with reasonable computational requirements and is used for most of the simulations of this thesis.

#### 3.6.4. Modelling Collisions

To model collisions between particles, GKW uses a collision operator  $C(f_a)$ . It appears as an additional term on the r. h. s of the gyrokinetic evolution equation, Eq. (3.46).  $C$  operates on the distribution function of the particle species  $a$ , modelling the influence of collisions with the species  $b$ . Starting from the Landau collision integral depending on the velocity  $v$  and the pitch angle  $\vartheta$ , under the assumption of a Maxwellian background, a linearised collision operator is derived [81]:

$$C(f_a) = \sum_b \frac{1}{v^2} \frac{\partial}{\partial v} \left[ v^2 \left( D_{vv}^{a/b} \frac{\partial f_a}{\partial v} - F_v^{a/b} f_a \right) \right] + \frac{1}{v \sin \vartheta} \frac{\partial}{\partial \vartheta} \left[ \sin \vartheta D_{\vartheta\vartheta}^{a/b} \frac{1}{v} \frac{\partial f_a}{\partial \vartheta} \right]. \quad (3.68)$$

The coefficient for pitch angle scattering is  $D_{\vartheta\vartheta}^{a/b}$ , the coefficient for the energy scattering is  $D_{vv}^{a/b}$  and the coefficient for the relaxation towards a Maxwellian is  $F_v^{a/b}$ . Respectively

to these, the collision operator is split into three parts

$$C(f_a) = C_{\vartheta\vartheta}(f_a) + C_{vv}(f_a) + C_v(f_a), \quad (3.69)$$

which can be used individually in GKW. The three coefficients  $D_{\vartheta\vartheta}^{a/b}$ ,  $D_{vv}^{a/b}$ ,  $F_v^{a/b}$  are (for each species  $b$ ) proportional to a constant  $\Gamma^{a,b}$ , which describes the collision frequency of two species  $a$  and  $b$ :

$$\Gamma^{a,b} = \frac{R_{\text{ref}} n_b Z_a^2 Z_b^2 e^4 \ln \Lambda^{a,b}}{4\pi \epsilon_0^2 m_a^2 m_b^2 v_{\text{th},a}}. \quad (3.70)$$

(Here,  $n_b$  is the density of species  $b$ ,  $Z_{a/b}$  is the corresponding charge number,  $e$  the elementary charge,  $\epsilon_0$  the vacuum permittivity,  $m_{a/b}$  the corresponding mass and  $v_{\text{th},a}$  the thermal velocity of species  $a$ .) The Coulomb logarithm  $\ln \Lambda^{a,b}$  depends on the combination of ions or electrons chosen for  $a$  and  $b$ . For ion-ion collision of the same species  $i$ , as used in this thesis, the Coulomb logarithm is

$$\ln \Lambda^{i,i} = 17.3 - \ln\left(\frac{Z_i^2}{T_i T_{\text{ref}}}\right) - \frac{1}{2} \ln\left(0.1 \frac{n_{\text{ref}}}{T_{\text{ref}}}\right) - \frac{1}{2} \ln\left(2 \frac{n_i Z_i^2}{T_i}\right). \quad (3.71)$$

The parameter  $T_i$  denotes the temperature normalized to  $T_{\text{ref}}$  and  $n_i$  the density normalized to  $n_{\text{ref}}$ . For ion-ion collisions,  $\Gamma^{i,i}$  becomes

$$\Gamma^{i,i} = \frac{R_{\text{ref}} n_i Z_i^4 e^4 \ln \Lambda^{i,i}}{4\pi \epsilon_0^2 m_i^2 v_{\text{th}}} \approx 1.18 \cdot 10^{-3} \frac{R_{\text{ref}} n_i Z_{\text{eff}}}{T_i^2}, \quad (3.72)$$

where  $Z_{\text{eff}}$  is the effective charge number. The linearised Fokker-Planck collision operator conserves the particle number but does not conserve particle momentum or energy [81]. To reintroduce momentum conservation, the term

$$C_{\text{mom}} v_{\parallel} F_M \quad (3.73)$$

is added to the collision operator. The constant  $C_{\text{mom}}$  is calculated through

$$2\pi C_{\text{mom}} \int dv_{\parallel} \int d\mu v_{\parallel}^2 F_M + 2\pi B \int dv_{\parallel} \int d\mu v_{\parallel} C(f_a) = 0, \quad (3.74)$$

which follows from the first moment of the collision operator. Energy conservation is achieved by adding

$$C_{\text{ene}}(v_{\parallel}^2 + 2\mu B - A) F_M, \quad (3.75)$$

where

$$2\pi C_{\text{ene}} \int dv_{\parallel} \int d\mu v_{\parallel}^2 (v_{\parallel}^2 - A) F_M + 2\pi B \int dv_{\parallel} \int d\mu (v_{\parallel}^2 - A) C(f_a) = 0, \quad (3.76)$$

is used to calculate  $C_{\text{ene}}$ . The factor  $A$  ensures particle conservation and is determined via

$$A = \frac{\int dv_{\parallel} \int d\mu v_{\parallel}^2 F_M}{\int dv_{\parallel} \int d\mu F_M}. \quad (3.77)$$



## 4. Influence of collisions on the Finite Heat Flux Threshold

In tokamaks, turbulence generated by the ion temperature gradient (ITG) instability is regulated by so-called zonal flows [82]. These poloidal flows are nonlinearly driven by the turbulence through the Reynolds stress and, in turn, reduce the turbulence through shear decorrelation [44]. The influence of the zonal flows is most prominent close to the threshold for turbulence generation, given by a specific temperature gradient length ( $R/L_T \equiv -R\nabla T/T$ ). In a landmark paper [21], it was shown that this threshold is not determined by the linear stability of the ITG, but rather is nonlinearly up-shifted. For gradient lengths ( $R/L_T$ ) in between the threshold for linear stability  $R/L_{T,\text{lin}}$  and the so-called Dimits threshold  $R/L_{T,\text{Dim}}$ , the ITG is linearly unstable, but as the turbulence develops it drives zonal flows that are sufficiently strong to suppress the turbulence, resulting in a state with a vanishing heat flux. The results of Ref. [21] were obtained in the collisionless case. Indeed, the collisional case is qualitatively different due to the collisional damping of the zonal flow. The heat flux below the Dimits threshold for the collisional case has been discussed in Ref. [34]. It was found that also for the collisional case the zonal flow spins up and suppresses the turbulence below the Dimits threshold, but due to the collisional damping of the zonal flows the lifetime of the phase with vanishing heat flux is limited and turbulence reappears again. This leads to an oscillatory behaviour in the heat flux, and a rise of the time averaged heat flux with collisionality [34].

It has recently been shown [10, 11] that the picture given above is incomplete, at least for the collisionless case. The nonlinear threshold for turbulence generation is not given by the Dimits threshold, i. e. the threshold obtained by interpolating the turbulent heat flux to zero. Rather, the threshold is given by the so-called finite heat flux threshold ( $R/L_{T,\text{fh}}$ ) that is significantly up-shifted compared with the Dimits threshold. At the finite heat flux threshold, the heat flux does not change continuously, but rather shows a jump from a state where turbulence is suppressed and the heat flux vanishes to a state where a finite heat flux is present. The latter heat flux can be larger than the heat fluxes obtained under experimental relevant conditions, and suggests that experimental heat flux calculations must, at least in some cases, be obtained from flux rather than gradient driven simulations [10]. The jump in the heat flux is shown to be related to the formation of staircases [11], which were first observed in fully developed turbulent simulations in Refs. [7–9]. In the state where turbulence is not suppressed, the finite heat flux is induced by avalanches [8, 83]. The simulations in Ref. [11], also show that sufficiently small dissipation is necessary to observe the finite heat flux threshold, and that in the region

#### 4. Influence of collisions on the Finite Heat Flux Threshold

$R/L_{T,\text{Dim}} < R/L_T < R/L_{T,\text{fn}}$  the turbulent system takes a considerable amount of time to settle in the vanishing heat flux state, particularly close to the finite heat flux threshold. This raises the question if the observation of the finite heat flux threshold is of mere academic interest. Does a significant change in the behaviour compared to the results presented in Refs. [10, 11] occur for experimentally relevant collision frequencies and how does this relate to previous understandings [34, 82]? It is this question this chapter will address.

The chapter is structured as follows. Section 4.1 presents an analysis of the zonal flow damping by collisions. Then in Section 4.2 the influence of the collision frequency on the turbulence and the finite heat flux threshold is examined. The corresponding behaviour of the (radially averaged) shear intensity is shown in Section 4.3. In Section 4.4 the interpretation of the correlation between the heat flux and staircases is explained. Section 4.5 gives a concluding discussion.

The content of this chapter has been published in Ref. [84].

### 4.1. Collisional damping of zonal flows

Before the influence of collisions on the finite heat flux threshold is examined, the collisional damping of the zonal flows is investigated in more detail. To this extent, linear simulations with an initial radial charge separation, equivalent to the (undamped) residual zonal flow “Rosenbluth-Hinton”-test [30–32], are carried out with GWK [54]. Collisions are included in this test and the time evolution of the electrostatic potential  $\phi$  connected with the zonal flow is examined. The potential consists of a decaying oscillation of a geodesic acoustic mode (GAM) and a slower decay of the residual potential. The latter contribution to the potential is thought to be responsible for turbulence suppression, and its decay is related to the collisional damping of the zonal flow. The collisional damping rate of the residue is measured and compared with an analytic model [35].

In the Rosenbluth-Hinton test, care has to be taken to mitigate the influence of the so-called recurrence-problem [41, 85]. Over time, the Landau damping [86] of the GAM generates fine structures of the distribution function in the velocity space [87–89]. Since in eulerian codes, the phase space is discretized with a fixed grid, this so-called phase space filamentation causes an under resolving of the distribution function after a certain time [90, 91]. This lack of resolution leads to an unphysical recurrence of an earlier structure of the distribution function and consequently, to the incorrect reappearance of the GAM-oscillation. The duration for which a simulation is physically correct, is determined by its grid-resolution, and therefore, long simulation times are connected with high computational resource demands.

To examine the relevance of the recurrence problem for the analysis of the damping of the zonal flow, simulations with the following parameters are carried out with GWK [54]:

A geometry with circular concentric flux-surfaces is used, with safety factor  $q = 1.3$ , magnetic shear  $\hat{s} = 0.1$ , and inverse aspect ratio  $\varepsilon = 0.15$ . The following grid sizes are used:  $N_s = 128$ ,  $N_\mu = 16$ , and  $N_{v_\parallel} = 128$ , where  $N_s$  is the number of grid points along the field line,  $N_\mu$  in the magnetic moment and  $N_{v_\parallel}$  in the parallel (to the magnetic field) velocity direction. A spectral representation is used for the directions perpendicular to the field, and only one radial wave vector with  $k_r \rho \ll 1$  is retained. No numerical dissipation is applied in all directions and for this preliminary examination, collision are not included. All simulations neglect plasma rotation, and use the electrostatic limit with the adiabatic electron response. The results are shown in Fig. 4.1. The thick blue line depicts the

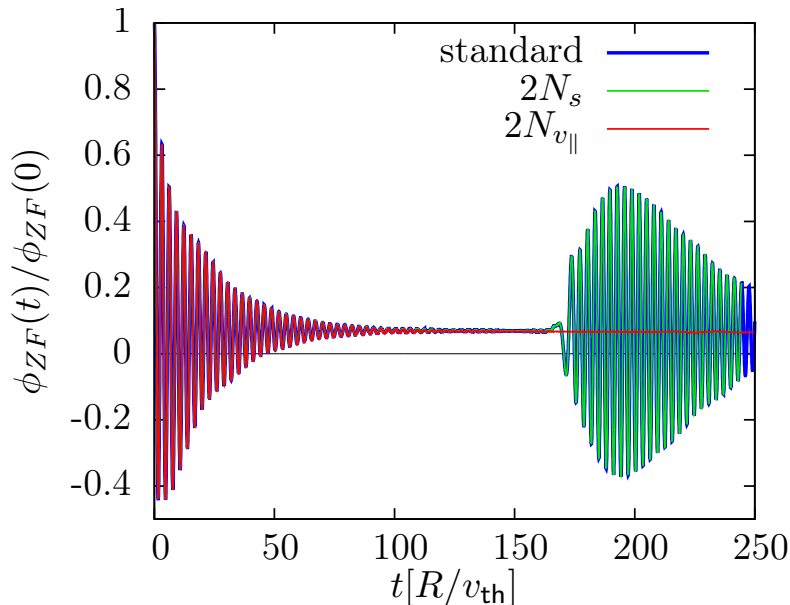


Figure 4.1.: Evolution of the normalized electrostatic potential in the Rosenbluth-Hinton-test. Results from a simulation with a standard test case parameter set and simulations with a doubled number of grid points along the magnetic field  $N_s$  or doubled points in the parallel velocity  $N_{v_\parallel}$  are shown. Note that different line widths are used to depict the (partly) similar data.

result of the simulation carried out with these parameters. Here, the initial perturbation of  $\phi$  leads to a decaying oscillation. However, the unphysical recurrence of the oscillation is observed at  $t \approx 160R/v_{th}$ . This effect does not allow physically correct interpretations at later times. It has to be mitigated, either by suppressing the phase-space-filamentation or by increasing the resolution in the velocity space. A common method to suppress the filamentation is to use a form of dissipation in the velocity space. Often a small, sometimes artificial collisions frequency is chosen [87]. If however, this dissipation would lead to an unwanted distortion of the results, which is exactly the case in this analysis, this option cannot be used and the resolution in the velocity space has to be increased. This is shown with the red line in Fig. 4.1, where a doubling of the grid points in the

#### 4. Influence of collisions on the Finite Heat Flux Threshold

parallel velocity leads to a later onset of the recurrence (not visible). A doubling of the points along the magnetic field line (green line) has no effect on the onset of the recurrence.

The simulations used to examine the collisional damping of the zonal flow have parameters similar to the aforementioned ones, with the following annotations: The grid is adapted to  $N_\mu = 96$  and  $N_{v_\parallel} = 512$ . It has to be noted that, as phase-space-filamentation is suppressed by dissipation, the recurrence problem appears mainly in the low collisionality-regime. But to ensure compatibility, the same grid sizes are used for all collision frequencies in this analysis. The values of  $q = 1.3$ ,  $\hat{s} = 0.1$ , and  $\varepsilon = 0.15$  are chosen to feature a relatively quick decay of the GAM, which allows to observe a larger part of the decay of the zonal potential unobstructed by the recurrence. To prevent vitiation of the collision's influence, no numerical dissipation is applied. Ion-ion collisions are included and are modelled with a pitch-angle scattering collision operator. The corresponding normalized collision frequency is defined as

$$\nu_{ii} = \frac{RnZ_i^4 e^4 \ln \Lambda^{i/i}}{4\pi\epsilon_0^2 m_i^2 v_{th}} \approx 1.18 \cdot 10^{-3} \frac{Rn^{19} Z_{eff}}{T_k^2}, \quad (4.1)$$

where  $R$  is the major radius in meters,  $n$  the density,  $Z_i$  the nuclear charge number,  $e$  the elementary charge,  $\ln \Lambda^{i/i}$  the coulomb logarithm,  $m_i$  the ion-mass,  $v_{th}$  the ion-thermal speed,  $n^{19}$  the density in units of  $10^{19} m^{-3}$ ,  $Z_{eff}$  the effective nuclear charge number and  $T_k$  the ion temperature in units of keV. The collision frequency in the equation above is normalized to  $v_{th}/R$ , where  $v_{th} = \sqrt{2T/m_i}$  is the thermal velocity. To give a relation to experiments, some values have been calculated for typical cases: ITER-prediction [92] ( $R_{ref} = 6$ ,  $n_{ref}^{19} = 12$ ,  $Z_{eff} = 1.9$ ,  $T_{ref} = 15$ ):  $\nu_{ii} = 6 \cdot 10^{-4}$ , simulated ITER discharge in DIII-D, shot 81499, cyclone base case [21, 22] ( $R_{ref} = 1.7$ ,  $n_{ref}^{19} = 5$ ,  $Z_{eff} = 1.9$ ,  $T_{ref} = 3$ ):  $\nu_{ii} = 2 \cdot 10^{-3}$ , DIII-D shot 128913, shortfall-case at edge [93, 94] ( $R_{ref} = 1.7$ ,  $n_{ref}^{19} = 1.2$ ,  $Z_{eff} = 1.3$ ,  $T_{ref} = 0.27$ ):  $\nu_{ii} = 4 \cdot 10^{-2}$ .

A sample result, a simulation with  $\nu_{ii} = 1.2 \cdot 10^{-3}$ , is shown in Fig. 4.2. The already described behaviour of the zonal potential  $\phi$  can be seen: an initial charge perturbation leads to a decaying GAM-oscillation revealing a zonal flow potential that is slowly damped by collisions. As the time in which the evolution of the potential can be observed is limited, the following method is used to obtain the evolution of the collisionally damped residual potential for early times, where the oscillation of the GAM are present: The mean value of two neighbouring maxima of the GAM-oscillation is used together with the value of the intermediate minimum (cyan + in Figures 4.2) to estimate the value of the potential (red x in Figures 4.2) at the time of the minimum. A similar calculation is made using two minima and one maximum to estimate the potential at the time of the corresponding maximum. Using all possible values, a good approximation of the potential is obtained, which is depicted (dashed red curve) in Fig. 4.2. This approximation is valid if the change in the GAM's oscillation and in its decay are sufficiently small, which is already given very early in the simulation. For very late times, when the GAM has been

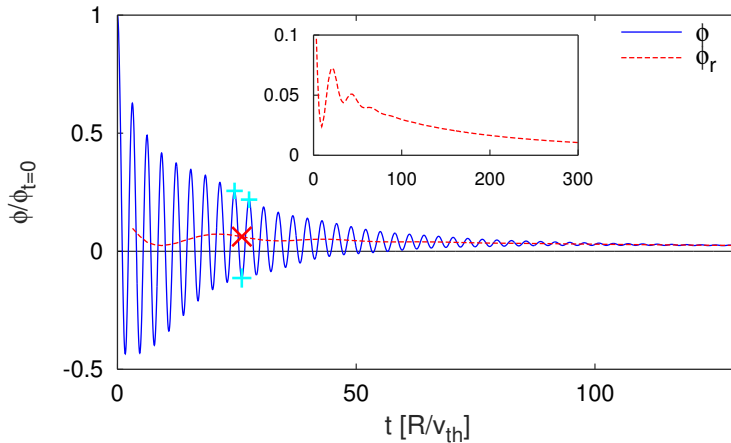


Figure 4.2.: Time evolution of the electrostatic potential  $\phi$  (blue) and the collisionally damped residual potential, where the influence of the GAM is removed (dashed red line), for a simulation with  $q = 1.3$ ,  $\varepsilon = 0.15$  and a collision frequency of  $\nu_{ii} = 1.2 \cdot 10^{-3}$ . To provide an example for the method to remove the GAM-influence several points are marked: To calculate one point of the potential, two maxima and one minima are marked (cyan “+”). The small box shows the long time decay of the potential.

strongly damped, a time average of the potential evolution over the GAM’s oscillation’s period is taken to ensure compliance with the data from early times.

Following this procedure, an analysis of the collisional damping of the zonal flow is undertaken varying the collision frequency  $\nu_{ii}$  between  $10^{-5}$  and  $10^{-1}$ . Also the influence of inverse aspect ratio and safety factor is studied, varying  $\varepsilon$  at  $q = \{1.3, 1.4\}$ . The time evolution of the potential can be roughly described with an exponential decay, i.e.  $\phi(t) = \phi_a \exp[-\nu_D t]$ , and a zonal flow damping rate ( $\nu_D$ ) can be determined. This damping rate is shown in Fig. 4.3 as a function of the collision frequency, showing a nearly linear relation  $\nu_D \approx \alpha \nu_{ii}$ .

The agreement between the analytic model and the numerical simulations is good at sufficiently low collision frequencies, and less satisfactory at higher collision frequencies. The predicted influence of  $\varepsilon$  and  $q$  on the collisionless residual and the residual at moderate collision frequencies can be reproduced numerically, which is shown in Fig. 4.4 (see also Ref. [54]).

Furthermore, for high collision frequencies the damped residual zonal flow converges to a finite stationary value within the simulated time interval. The latter undamped zonal flow corresponds to a purely toroidally rotating plasma, with the numerically obtained result in good agreement with the prediction of Ref. [35].

#### 4. Influence of collisions on the Finite Heat Flux Threshold

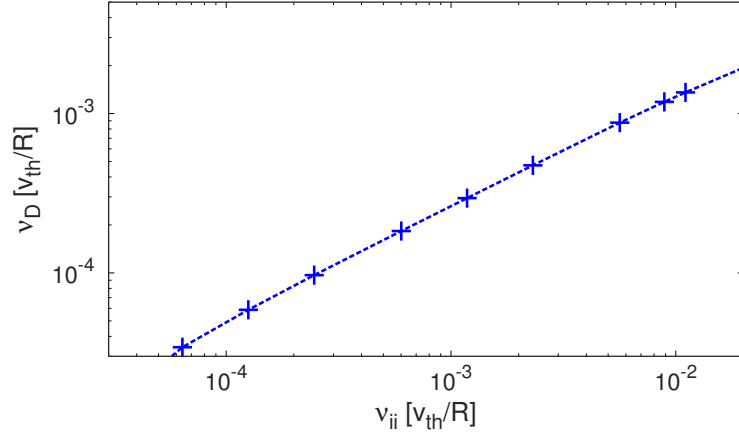


Figure 4.3.: Zonal flow damping rate as a function of the collision frequency following Ref. [35].

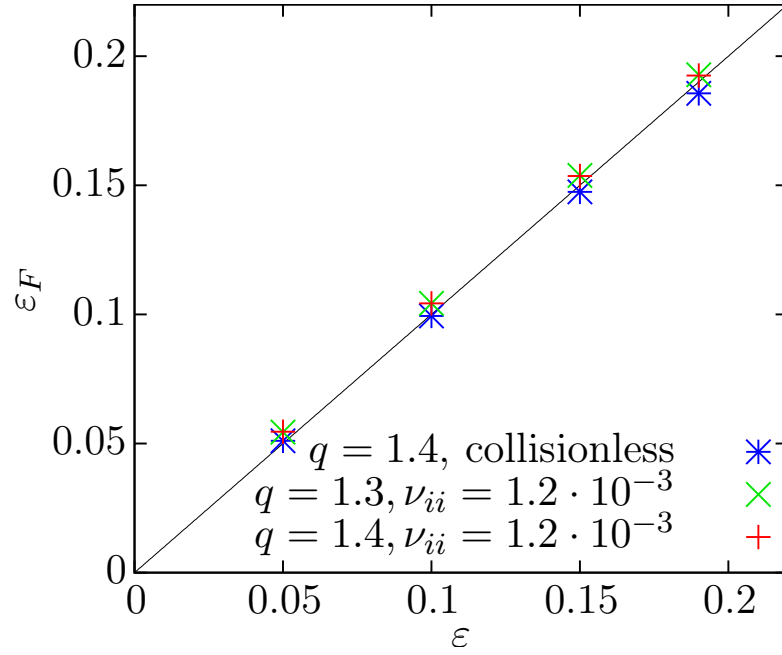


Figure 4.4.: Recovered inverse aspect ratio  $\varepsilon_F$  for collisionless simulations and simulations with a collision frequency of  $\nu_{ii} = 1.2 \cdot 10^{-3}$  at different values of  $q$ .

## 4.2. Analysis Of The Finite Heat Flux Threshold

To examine the influence of collisions on the heat flux and the finite heat flux threshold, a set of nonlinear flux-tube simulations is carried out with GKW. For this task, the

## 4.2. Analysis Of The Finite Heat Flux Threshold

parameters are chosen to be compliant to the well known cyclone base case: safety factor  $q = 1.4$ , magnetic shear  $\hat{s} = 0.78$ , inverse aspect ratio  $\varepsilon = 0.19$ , density gradient  $R/L_n = 2.2$ , and electron to ion temperature ratio  $T_e/T_i = 1$ . The geometry, however, is not modelled by the  $\hat{s} - \alpha$  geometry as in Ref. [21], but rather through the use of a circular flux surface geometry that keeps all orders in the inverse aspect ratio. This choice leads to a change in the Dimits shift (from 6.0 for  $\hat{s} - \alpha$  to 4.7 for the circular geometry) and also influences the finite heat flux threshold [11]. The grid is chosen as follows: number of radial modes  $N_x = 83$ , number of toroidal modes  $N_y = 21$ , number grid points along the field line  $N_s = 16$ , number of magnetic moment grid points  $N_\mu = 9$ , and number of parallel velocity grid points  $N_{v_\parallel} = 64$ . For the zonal mode the sixth order scheme along the magnetic field is used, and the dissipation coefficients are  $D_x = 0.1$ ,  $D_y = 0.1$ ,  $D_s = 1$ , and  $D_{v_\parallel} = 0.1$ . A detailed description of the implementation and its effect on the dissipation can be found in Ref. [11]. Following this analysis, the exponential damping rate due to the chosen grid is expected to be  $|\gamma_d^{(6)}| = 1.9 \cdot 10^{-4}$  normalized to  $v_{th}/R$  and might only have an influence on the simulations with lower collision frequencies. A comparison of the zonal flow damping due to this resolution with the one due to the resolution used in Section 4.1 shows no significant differences in the damping. The temperature gradient is varied in a range of  $R/L_T \in [3.0, 16.0]$ , where the main part of the simulations is focused on the area around the finite heat flux threshold. Ion-ion collisions are, similar to the above study, treated with pitch-angle scattering, varying the collision frequency in a range of  $\nu_{ii} \in [10^{-5}, 1]$ .

Previous studies of collisionless ITG turbulence have shown that there are three specific ion temperature gradient lengths in the zonal-flow / ITG system that are relevant for the description of the heat flux near the threshold: the gradient length of linear stability  $R/L_{T,lin}$ , the Dimits gradient length  $R/L_{T,Dim}$  [21], and the finite heat flux threshold  $R/L_{T,fh}$  [10, 11], with  $R/L_{T,lin} < R/L_{T,Dim} < R/L_{T,fh}$ . Here, the Dimits threshold is defined as the gradient length for which the extrapolated heat flux goes through zero, with the heat fluxes used in the extrapolation being obtained for gradient lengths well above the threshold. The finite heat flux threshold is the temperature gradient length below which a vanishing heat flux is found, i.e. it is the temperature gradient length at which the heat flux is discontinuous. In light of the findings outlined above, it is natural to divide the gradient length parameter space into three zones: I  $R/L_{T,lin} < R/L_T < R/L_{T,dim}$ , II  $R/L_{T,dim} < R/L_T < R/L_{T,fh}$ , and III  $R/L_T > R/L_{T,fh}$  (see Fig. 4.8a). Indeed it will be shown below that the influence of collisions on the heat flux is very different in these three regions.

In general, the observed time evolution of the flux surface averaged heat flux can be described as follows (some examples are presented in Fig. 4.5a): After a short initial "linear" growth due to the ITG-instability, a turbulent state with a finite heat flux develops. If the temperature gradient length is far below the finite heat flux threshold (i.e. in region I and to some extent in region II close to the border with region I), the turbulent state hardly develops. Zonal flows quickly suppress the turbulence, and a state of vanishing

#### 4. Influence of collisions on the Finite Heat Flux Threshold

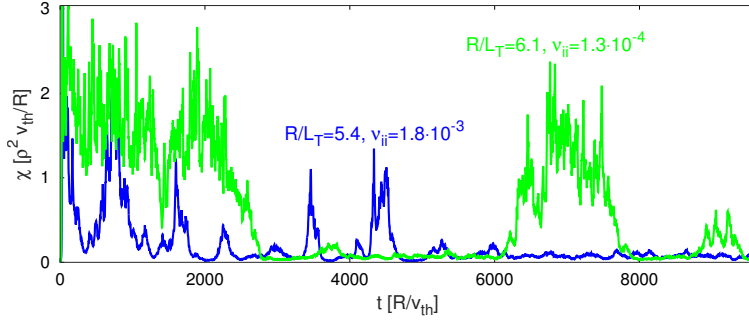
heat flux results. This is the physics picture described in Ref. [21]. Closer to the finite heat flux threshold (region II), the turbulent state can persist for a long time before the turbulence is eventually suppressed. Additionally, a temporary inversion of states, from a high to a low heat flux state and vice versa, can be observed. Thus, for the evaluation of the heat flux and the heat conductivity, care has to be taken that the simulation has reached a proper stationary state. For gradient lengths above the finite heat flux threshold (region III), the turbulence remains in a high heat flux state for the entire duration of the simulation.

It should be noted that only two states are properly discernible. Below the finite heat flux threshold a state where turbulence is suppressed and the heat flux is close to zero, is found. Only a small baseline turbulence that drives the zonal flow against the collisional dissipation remains. Above, a state where turbulence is only partially suppressed and the heat flux is finite (heat conduction  $\chi \gtrsim 1$ ) due to mediation by avalanches, is present. The physics picture that even in the low heat flux state the zonal flow can be driven against the collisional dissipation is confirmed by a study of the free energy transfer. For the low heat flux state with a collision frequency  $\nu_{ii} = 1.3 \cdot 10^{-4}$ , the free energy source due to the heat flux in the ion temperature gradient ( $Q_i R/L_t$ ) is well in excess of the free energy transferred to the zonal flow through the nonlinear interaction. The latter energy transfer, in turn is larger than the collisional dissipation. Nevertheless, an in-depth analysis, as carried out in Ref. [95] appears as a rewarding topic for future investigations.

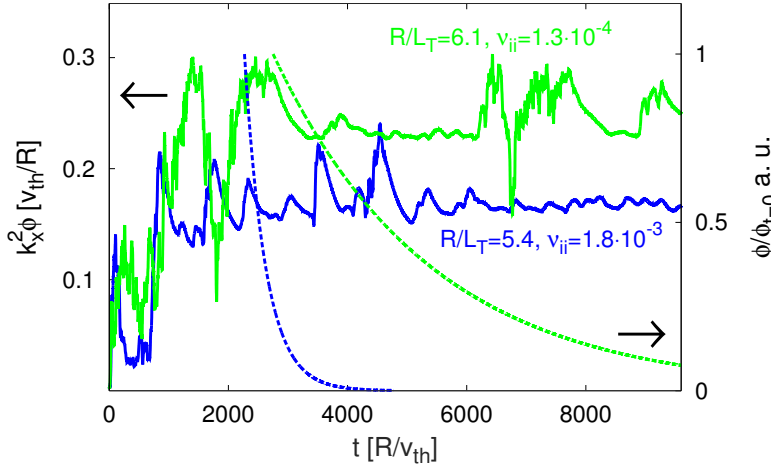
If parameters close to the finite heat flux threshold are chosen, fragile states with a transpositions of the two states are found. This transposition appears below and above the finite heat flux threshold and was already observed in Ref. [11]. Slightly below the threshold, these simulations show flares where a finite heat flux appears for a reasonable time interval ( $\gtrsim 1000R/v_{th}$ ). Slightly above the threshold, short periods with a suppressed heat flux are found, but the transposed state appears less pronounced as below the threshold. Generally, this transposition is found to appear at lower collision frequencies.

Two examples of simulations with such a transposition below the finite heat flux threshold are presented in Fig. 4.5a, where the time evolution of the heat conductivities for two simulations at  $R/L_T = 5.4$ ,  $\nu_{ii} = 1.8 \cdot 10^{-3}$  and at  $R/L_T = 6.1$ ,  $\nu_{ii} = 1.3 \cdot 10^{-4}$  are shown. The latter simulation nicely shows the transposition: the turbulence is suppressed at  $t \approx 3000$  (time is normalized to  $R/v_{th}$ ) and the simulation remains in the suppressed state for 3000 time units before a flare in  $t \in [6000, 8000]$  appears, afterwards the simulation remains in the suppressed state until the end of the simulation (a period of 6000, not depicted in Fig. 4.5a). In the evolution of the heat conductivity of the simulation at  $\nu_{ii} = 1.8 \cdot 10^{-3}$  this behaviour, albeit less pronounced, can also be seen: a relatively quiet time in  $t \in [1800, 3400]$  is followed up by two flares at  $t \approx 3400$  and  $t \approx 4200$ .

## 4.2. Analysis Of The Finite Heat Flux Threshold



(a) Time evolution of the heat conductivity  $\chi$  of simulations at  $R/L_T = 5.4$  with  $\nu_{ii} = 1.8 \cdot 10^{-3}$  (blue), and at  $R/L_T = 6.1$  with  $\nu_{ii} = 1.3 \cdot 10^{-4}$  (green). These simulations are located in zone II and are close to the finite heat flux threshold.



(b) Time evolution of the shearing rate  $k_x^2\phi$  for simulations at  $R/L_T = 5.4$ ,  $\nu_{ii} = 1.8 \cdot 10^{-3}$  and at  $R/L_T = 6.1$ ,  $\nu_{ii} = 1.3 \cdot 10^{-4}$  (both zone II), represented on the left  $y$ -axis. To give an idea for the estimated decay of the zonal flow potential, the results from the linear analysis in Section 4.1 are added at the corresponding times, being represented on the right  $y$ -axis. Data from simulations with collision frequencies of  $\nu_{ii} = 1.3 \cdot 10^{-4}$  and  $\nu_{ii} = 2.3 \cdot 10^{-3}$  are used respectively. The data was adapted to the parameters used in this analysis according to the model of Ref. [35].

Furthermore, these simulations can be used to demonstrate the influence of the avalanches. Therefore the time evolution of the radial profile of the heat conductivity is presented in Fig. 4.6.

The structure and radial propagation of the avalanches is visible, for example in the inlet depicting the time period  $t \in [6600, 6900]$  (note the periodic boundary conditions). Similar to the results of Ref. [11], corresponding structures are also found in the perturbed temperature gradient. As previously observed, the perturbed temperature gradient, averaged over the turbulent period, shows a decrease in the area where the avalanches are generated and also a decrease where the avalanches disappear (these areas correspond with the flanks of the staircases, as discussed further below). A clear correlation of the

#### 4. Influence of collisions on the Finite Heat Flux Threshold

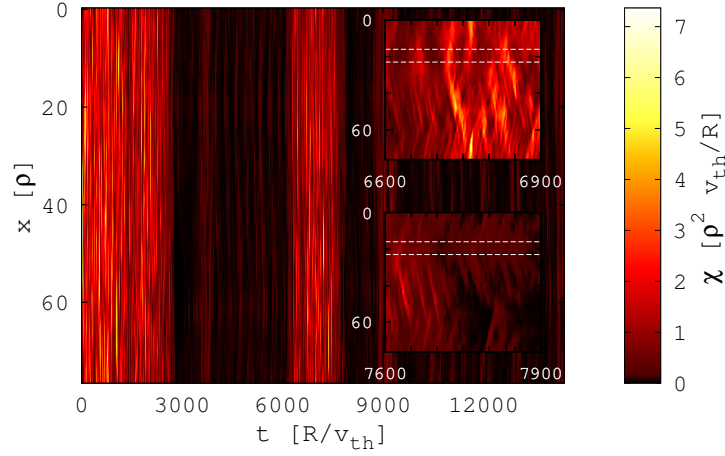
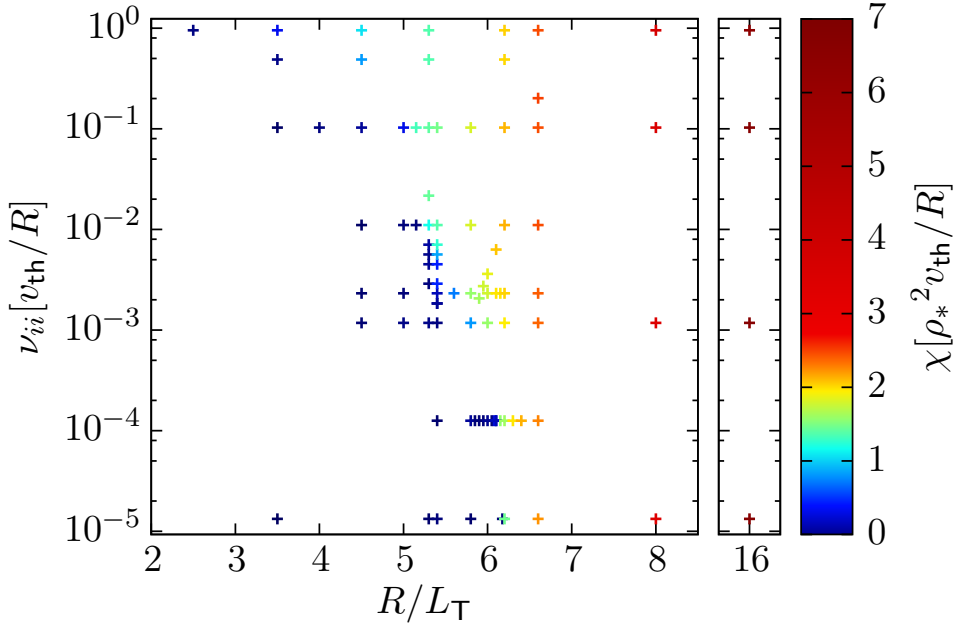


Figure 4.6.: Time evolution of the radial profile of the heat conductivity  $\chi$  for a simulation at  $R/L_T = 6.1$  and  $\nu_{ii} = 1.3 \cdot 10^{-4}$ . The insets show a short turbulent time period (top) and a period at the transition to the suppressed state (bottom). The area where avalanches emerge is marked with dashed white lines and is located radially at approximately  $20\rho$ .

avalanche activity with the time evolution of the averaged heat conductivity in Fig. 4.5a can be seen. The correlation between avalanches and a finite heat flux is paradigmatic not only for the transposing simulations, but for all simulations. For gradient lengths just above the finite heat flux threshold as well as for the transposing states, avalanches are identified as the main reason for a finite heat flux. Further examinations of these simulations follow in Section 4.3 and 4.4.

Fig. 4.7 shows the heat conduction coefficient  $\chi$  depending on the gradient length  $R/L_T$  and the collision frequency  $\nu_{ii}$ . The heat conduction coefficients in this figure have been averaged over sufficient long time intervals to address possible intermittent behaviour of the heat flux. For visual convenience Fig. 4.8a depicts  $\chi$  as a function of the gradient length for certain values of  $\nu_{ii}$ . For vanishing  $\nu_{ii}$  the results of a collisionless study [11] are reproduced, with only slight differences which are connected with the different resolution used in this analysis. It can be directly observed that the susceptibility towards collisional effects is very different in the three regions. In region I and III, i.e. below the Dimits gradient length or above the finite heat flux threshold, collision frequencies  $\nu_{ii} > 0.1$  are required to generate a still relatively small change in the heat flux. To put this in perspective, at  $R = 1.7$  m,  $n = 4 \cdot 10^{19} \text{ m}^{-3}$ , this corresponds to a temperature  $T \approx 250$  eV. Therefore, collisional damping of the zonal flows above the finite heat flux threshold or below the Dimits threshold is in present day experiments important only in the outer edge of L-mode discharges. The influence of collisions is, however, much larger in the region II. Already at moderate collision frequencies the finite heat flux threshold gradient length ( $R/L_{T,\text{fh}}$ ) is reduced with increasing  $\nu_{ii}$ . A clear step in the heat flux, with no

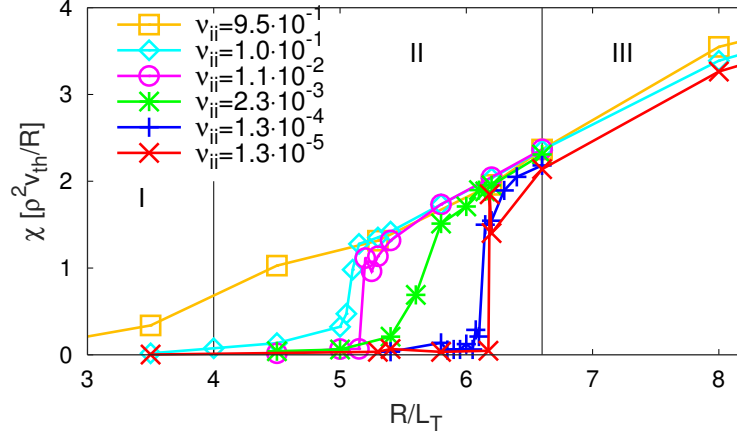
Figure 4.7.: Averaged heat flux in the  $R/L_T$ - $\nu_{ii}$ -plane.

clear sign of a flattening of the heat conduction versus temperature gradient length curve, however, remains visible up to high collision frequencies ( $\nu_{ii} > 0.1$ ). Only at very high values of the collision frequency ( $\nu_{ii} \approx 1$ ) does the heat flux go smoothly to zero.

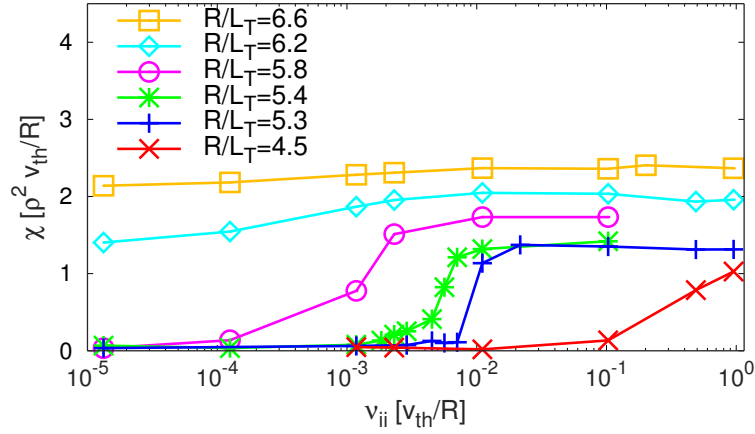
A steep threshold is also observed in the heat conduction coefficient ( $\chi$ ) as a function of collision frequency as shown in Fig. 4.8b. As stated before, the heat conduction coefficient obtained in the region I and III ( $R/L_T = 4.5, 6.2$  and  $6.4$ ) only changes at high collision frequencies. For  $R/L_T$  in region II,  $\chi$  shows a threshold, which changes its position towards lower  $\nu_{ii}$  and considerably softens for increasing  $R/L_T$ . Here also a slight increase of the heat flux below the finite heat flux threshold can be observed, which manifests both in the mean value of the baseline turbulence and also in an increased appearance and markedness of small unsuppressed turbulence flares in the (not shown) time traces. Above the finite heat flux threshold, the influence of the collisions becomes less pronounced.

Fig. 4.9 shows the finite heat flux threshold as a function of  $\nu_{ii}$ . Here, the threshold for each  $\nu_{ii}$  is determined as the lowest value of  $R/L_T$  where  $\chi$  has a (proper) finite value. For  $\nu_{ii} = 9.5 \cdot 10^{-1}$  the threshold is set to the value where the heat flux vanishes ( $R/L_T = 3.5$ ). It follows that the difference between the finite heat flux threshold and the Dimits threshold is significant up to relatively high collision frequencies. In collisionless simulations it was found that it can take a considerable time for the heat flux to settle in the low heat flux state, especially close to the finite heat flux threshold [11]. Indeed close to this threshold a very small collision frequency is sufficient to generate a finite heat flux. However further below the collisionless finite heat flux threshold, the system settles in a considerable shorter time, and a higher collision frequency is required to

#### 4. Influence of collisions on the Finite Heat Flux Threshold



(a) Heat conduction coefficient  $\chi$  depending on  $R/L_T$  for different  $\nu_{ii}$ .



(b) Heat conduction coefficient  $\chi$  depending on  $\nu_{ii}$  for different  $R/L_T$  chosen from region II.

generate a high heat flux. In modern day experiments and certainly in ITER the heat flux is predicted to have a discontinuous behaviour as a function of  $R/L_T$ . However it should be noted that, as seen if the temperature gradient is considered a function of the heat flux, this behaviour should be contemplated cautiously as an exact analysis and flux driven simulations might be employed. Nevertheless the gradient driven simulations provide important conclusions on the collisional behaviour.

The analysis of the dependence of the heat flux on the collision frequency allows a comparison with the work presented in Ref. [34]. In the latter reference a rise of the heat flux with increasing collision frequency was found. The results presented here suggest a somewhat steeper, discontinuous transition, from a state with vanishing heat flux to a state with a finite heat flux. Although the rise in the heat flux with collision frequency is

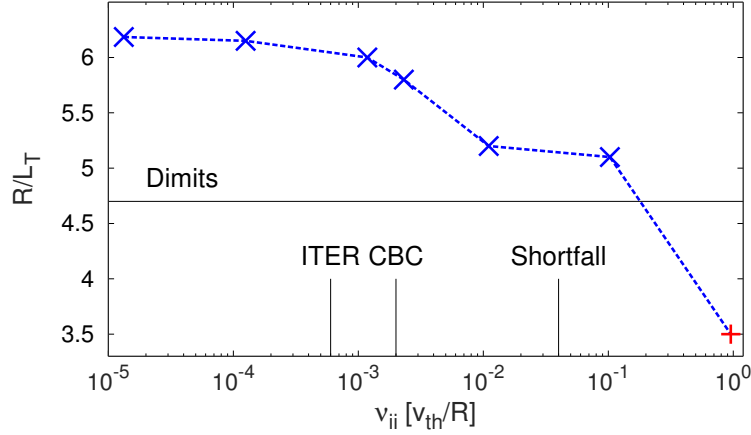


Figure 4.9.: Position of the finite heat flux threshold as a function of the collision frequency marked as blue "x". The estimated threshold for very high  $\nu_{ii}$  is added as red "+". The position of the three sample collision frequencies given in Section 4.1 are depicted. Also the value of the Dimits threshold  $R/L_{T,Dim} = 4.7$  is indicated.

qualitatively similar, it should be noted that the interpretation of the turbulent state is rather different. In Ref. [34] it is assumed that the value  $R/L_T = 5.3$  lies below the Dimits threshold, whereas in this chapter this value is shown to lie above the Dimits threshold but below the finite heat flux threshold. It is furthermore noted that much larger time intervals have been used in this chapter. It has been found that these long time intervals are essential to obtain the correct heat flux at values close to the threshold.

### 4.3. Analysis of the shear intensity

The finite heat flux threshold is connected with a radial structure formation known as staircase. Before investigating the radial profiles of the shearing rate, in this section the magnitude of the shearing rate as a function of the parameters is investigated. The focus is on the shearing rate ( $\omega_{E \times B}$ ) of the lowest radial wave vector in the computational domain since it is the wavelength of this mode that sets the radial scale length of the staircase close to the finite heat flux threshold.

In Fig. 4.10, this shearing rate  $\omega_{E \times B} = k_x^2 \phi$  of the simulations presented above (Fig. 4.7 etc.), normalized with  $v_{th}/R$ , is depicted in the  $R/L_T - \nu_{ii}$ -plane. To ease the discussion of these results, Fig. 4.11 shows the values of  $\omega_{E \times B}$  as a function of the gradient length  $R/L_T$  for selected  $\nu_{ii}$ . The shearing rate as a function of  $R/L_T$  shows a similar behaviour for all values of the collision frequency. The rate is small for values of the temperature gradient length well below the finite heat flux threshold and increases almost linearly with  $R/L_T$ , having the same value for all collision frequencies. At the corresponding

#### 4. Influence of collisions on the Finite Heat Flux Threshold

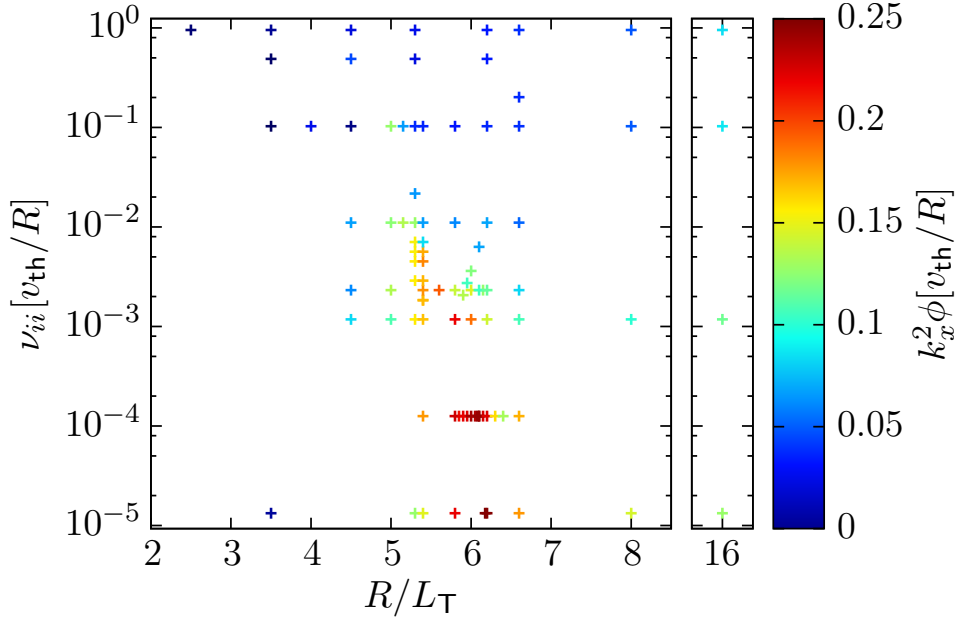


Figure 4.10.: Zonal flow shear strength of the zero mode in the  $R/L_T$ - $\nu_{ii}$ -plane.

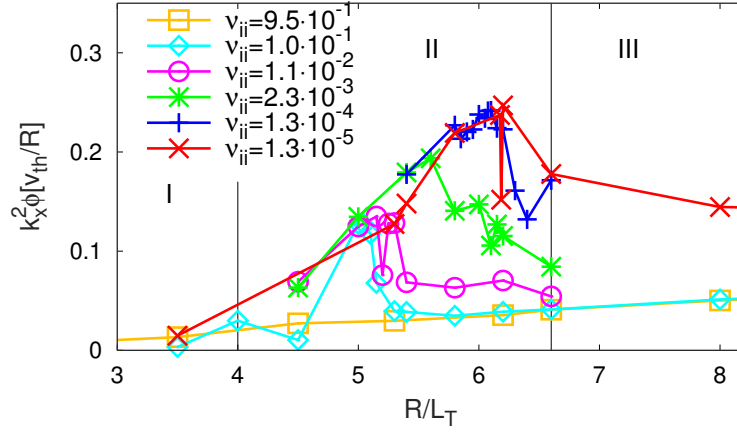


Figure 4.11.: Zonal flow shear strength of the zero mode depending on  $R/L_T$  for various  $\nu_{ii}$ .

collisional finite heat flux threshold a change in slope of the shearing rate as a function of the gradient length is observed, with the shearing rate decreasing when further increasing the gradient length. In accordance with the behaviour of the finite heat flux threshold, the gradient length of this change is reduced if the collision frequency is raised. As a consequence of this behaviour a lower maximum shearing rate is found for higher collision frequencies. It is noted, that a small parameter region in  $R/L_T$  exists, where a relatively

high value of the shearing rate is paired with a finite heat flux. This shows that the absolute value of the long wave length zonal mode amplitude is not the only factor that determines turbulence suppression. The simultaneous occurrence of a high heat flux and a high ExB shear is relatively insensitive to the collision frequency, but the region in  $R/L_T$  where it occurs shifts downward with increasing collision frequency which signals that the proximity to the finite heat flux threshold is important.

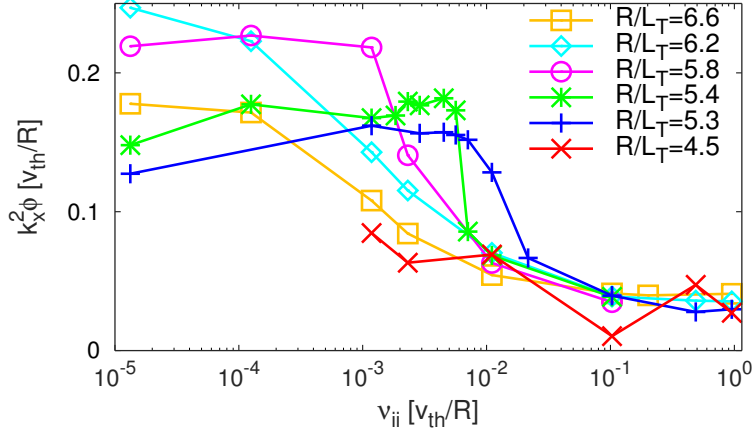


Figure 4.12.: Zonal flow shear strength of the zero mode depending on  $\nu_{ii}$  for various  $R/L_T$ .

Fig. 4.12 shows the shearing rate as a function of collision frequency for various values of the temperature gradient length. For intermediate  $R/L_T$  (below the collisionless threshold at  $R/L_T = 6.2$ ), the shearing rate shows a slight increase when  $\nu_{ii}$  is increased. At collision frequencies that correspond to the finite heat flux threshold, the shearing rate drops quickly and finally slowly decays towards a finite value for high collision frequency. The latter value appears to be almost independent of the gradient length. At high  $R/L_T$ , above the collisionless threshold, the shearing rate decays more smoothly towards the same finite value for high  $\nu_{ii}$ . It is noted, that the latter simulations show a smaller shearing rate when compared with the shearing rate that is obtained at the finite heat flux thresholds in simulations with smaller temperature gradient lengths.

We interpret the results shown above as follows: Below the finite heat flux threshold (but above the Dimits threshold) the turbulence drives the long wave length zonal flow mode connected with staircase formation until it is large enough to suppress the turbulence. Since the growth rate ( $\gamma$ ) of the ITG depends on the gradient length, but is, at these values of the collision frequency, relatively insensitive to the collision frequency, the shear values required for turbulence stabilization ( $\omega_{E \times B} \approx \gamma$ ) scales roughly linear with the gradient length. For this reason the shearing rate is observed to increase with  $R/L_T$  independent of the collision frequency. Above the finite heat flux threshold, the shearing

#### 4. Influence of collisions on the Finite Heat Flux Threshold

rate is observed to decay with increasing  $R/L_T$ , despite the increase in turbulence intensity and heat flux. This result is quite contrary to the usual discussion on zonal flow development, where the zonal flow is driven by the modulation instability and saturates over collisional damping or nonlinear terms connected with the zonal flow amplitude. In the latter scenario one would not predict a reduction in the zonal mode amplitude with increasing  $R/L_T$  at constant collision frequency. Here, it appears that the increase in turbulence intensity leads to a reduction in the zonal flow. The reason for this is at present unknown. Either the turbulence directly acts to decrease the zonal flow amplitude or the turbulence drives the zonal flow less effectively. There does not appear to be a satisfactory physics picture for either of these explanations. Also it should be noted, however, that the results shown in Fig. 4.12 concern the long wave length zonal flow only, and do not reflect on the shorter wavelength shear layers. The physics governing the different length scales of the zonal flow are possibly very different. The reduction in the finite heat flux threshold with the collision frequency can be explained as follows: In collisionless simulations it is observed that the time the system takes to settle in the low heat flux state increases as the finite heat flux threshold is approached. The long wave length zonal flows take longer to develop as the gradient length is increased and, therefore, collisions affect the heat flux most strongly at gradient lengths closer to the threshold.

Evidence for the influence of staircases can be seen in an examination of the shearing rate of the simulations showing a transposition of states mentioned in Section 4.2. In Fig. 4.5b (in Section 4.2), the time evolution of the shear intensities for simulations at  $R/L_T = 5.4$ ,  $\nu_{ii} = 1.8 \cdot 10^{-3}$  and at  $R/L_T = 6.1$ ,  $\nu_{ii} = 1.3 \cdot 10^{-4}$  are depicted next to their heat conduction coefficients shown in Fig. 4.5a. There are several noteworthy observations. As commonly known the initial turbulence leads to a growth of the shear intensity. Following the interpretation [34, 82], a suppression of the turbulence with a subsequent collisional decay of the shear intensity and the emergence of an oscillatory behaviour should be observed. For the simulation at  $R/L_T = 5.4$ ,  $\nu_{ii} = 1.8 \cdot 10^{-3}$ , this behaviour can be roughly made out for early times  $t \lesssim 5000$ , but not for later times. In the data of the simulation with a lower collision frequency at  $R/L_T = 6.1$ ,  $\nu_{ii} = 1.3 \cdot 10^{-4}$ , this behaviour is hardly recognisable at all. Furthermore, for later times in all simulations below the finite heat flux threshold, the state with the vanishing heat flux is present and does not show an oscillating behaviour of the turbulence. The simulations showing the transposing behaviour are also in this state in between two flares, for example  $t \in [3000, 6000]$  in Fig. 4.5a and 4.5b for  $R/L_T = 6.1$ ,  $\nu_{ii} = 1.3 \cdot 10^{-4}$  or less pronounced in the simulation with higher collision frequency in the period where  $t \in [1800, 3400]$ . Also, the time the simulation is in this state is considerably longer than one would expect if the decay of the zonal flow potential is considered. To point this out, the expected decay of the zonal flow potential is depicted at the according position in Fig. 4.5b. It is calculated with the results obtained in Section 4.1 for collision frequencies of  $\nu_{ii} = 1.3 \cdot 10^{-4}$  and  $\nu_{ii} = 2.3 \cdot 10^{-3}$  to match the frequencies respectively. The data is adapted to the parameters used in this analysis (described in Section 4.2) according to the model of Ref. [35]. Although the data was obtained with a much higher resolution, it is still relevant (see discussion

in Section 4.2). Here it can be seen, that the zonal potential from the linear analysis already would have been significantly decayed before another flare erupts. Although the intensity of the shear shows a decay resembling the one predicted by the linear analysis, it does so only for a very short time and then stays rather constant at a relatively high value due to a baseline turbulence before another flare appears. This shows that the potential does not follow the proposed decay. This becomes exceptionally clear, when not the period between two flares is considered, but the period after the last flare:  $t \geq 5000$  for the simulation with a higher collision frequency and  $t \geq 8000$  for the simulation with lower collision frequency (here the simulation ran until  $t = 14400$ ). In that time the zonal flow should have decayed and turbulence reappeared, which is not the case.

#### 4.4. Analysis Of the radial shear profile

Further insight can be gained from the shape of the radial shear profile. Nearly all of the simulations described in this chapter show so-called staircases in their radial shear profile, i.e. self-organized shear flow structures [7–9], which require long timescales to develop properly. They have been classified [11] into fully (box-shaped in gradient-driven simulations) and partially developed (sawtooth shaped in gradient-driven simulations) staircases. A fully developed staircase is thought to suppress turbulence as it allows a sufficiently high shear over nearly all of the radial domain. A partial developed staircase has a wider region with a low shearing rate (compared with the associated ITG growth rate) and allows heat flux avalanches to originate from such regions, leading to a finite heat flux. An example of these forms can be seen in Fig. 4.13: a fully developed staircase at  $\nu_{ii} = 4.5 \cdot 10^{-3}$ , a partially developed staircase at  $\nu_{ii} = 1.1 \cdot 10^{-2}$ . We assume that staircases form with specific radial extends and are not affected by the boundary conditions imposed in the radial direction due to the box-size test carried out in Ref. [10].

In the simulations carried out in this analysis, the expected correlation with the finite heat flux threshold is found not only, as already previously examined, in the direction of the temperature gradient length, but also if the finite heat flux threshold is passed in the collision frequency. As an example for this, Fig. 4.13 presents the radial shear profiles averaged over a substantial time period of simulations with different collision frequencies for a fixed temperature gradient length of  $R/L_T = 5.3$ . For the chosen temperature gradient length, the finite heat flux threshold (in  $\nu_{ii}$ -direction) is located at  $\nu_{ii} = 1.1 \cdot 10^{-2}$  following the definition given in Section 4.2. Below the finite heat flux threshold, fully developed staircases are present at times when turbulence is suppressed, for example the shear profile at  $\nu_{ii} = 4.5 \cdot 10^{-3}$  in Fig. 4.13. Slightly above the threshold, partially developed staircases are present, as visible in the shear profile at  $\nu_{ii} = 1.1 \cdot 10^{-2}$  in Fig. 4.13. Here, avalanches emerge from the region where shear is low  $\omega_{E \times B} \ll \gamma$  and propagate through the regions where shear is high  $\omega_{E \times B} \approx \gamma$ , which leads to a finite heat flux. It should be noted, that in all simulations with a partial staircase, it was observed that the softening of the flank occurred at the transition where the shear

#### 4. Influence of collisions on the Finite Heat Flux Threshold

changes its value from approximately  $+\gamma$  to  $-\gamma$ . At very high collision frequencies, no discernible structures are found, an paradigmatic radial profile is shown for  $\nu_{ii} = 1.0 \cdot 10^{-1}$ . Furthermore it should be noted that the simulations above the finite heat flux threshold show significantly higher fluctuations in the radial shear profile. This is thought to be a consequence of the turbulent activity.

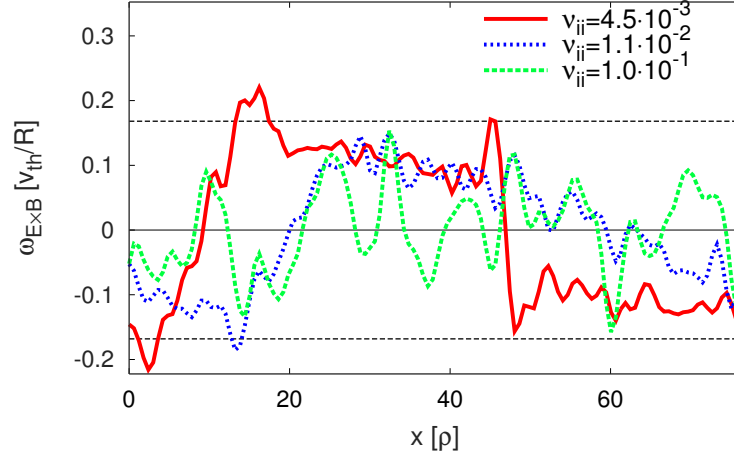


Figure 4.13.: Radial shear profile for different  $\nu_{ii}$  at a fixed temperature gradient length of  $R/L_T = 5.3$ . The dashed black line represents the corresponding growth rate for the most unstable ITG-mode.

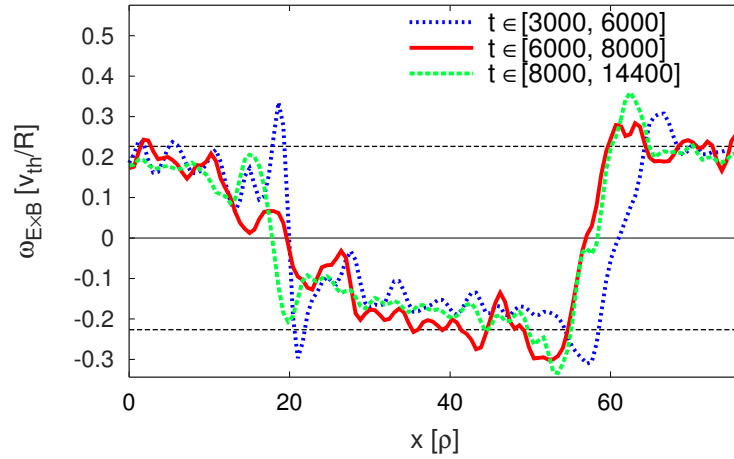


Figure 4.14.: Radial shear profile of the simulation at  $R/L_T = 6.1$ ,  $\nu_{ii} = 1.3 \cdot 10^{-4}$ . The shear is averaged in different times representing the different states, visible for example in the heat conduction coefficient depicted in Fig. 4.5a. The dashed black line represents the corresponding growth rate for the most unstable ITG-mode.

As already pointed out in Ref. [11], the change of the staircase type can also be seen in the different time periods of the simulations which show a transposition of states. To exemplify this, the radial shear profile of the simulation at  $R/L_T = 6.1$ ,  $\nu_{ii} = 1.3 \cdot 10^{-4}$ , averaged in time periods representing the different states, is shown in Fig. 4.14. If the profiles of the different times are related to the time evolution of the heat conduction coefficient presented in Fig. 4.5a, the correspondence between times, where a fully developed staircase is present and periods where the heat flux is suppressed, and vice versa, is clearly visible. In the periods  $t \in [3000, 6000]$  and  $t \in [8000, 14400]$ , where the heat flux is suppressed, the radial shear profile shows a fully developed (box-shaped) staircase structure. Whereas in the time range  $t \in [6000, 8000]$ , a finite heat flux is present and the radial shear profile shows the structure of a partial staircase. This can also be seen in the avalanche activity visible in the radial profile of the heat conduction coefficient presented in Fig. 4.6. Here it can also be nicely seen that the avalanches emerge from the softened flank of the staircase. The softened flank of the staircase for  $t \in [6000, 8000]$  lies at approximately  $20\rho$  and leads to an area of low shear around it, as visible in Fig. 4.14. This area corresponds to the area where the avalanches emerge, indicated with the dashed white lines in Fig. 4.6.

We interpret the results as follows: The form of staircase stands in direct correlation to the heat flux. A fully developed staircase allows a high shear, meaning about the same magnitude as the growth rate of the fastest growing corresponding ITG mode, over nearly the whole radial domain. This effectively suppresses turbulence. Also, for this form, the regions where the shear is low are considerably small and thus, heat flux avalanches cannot emerge from these regions. If the structure changes to a partial staircase i.e. the flank softens, the region where the shear is low is wide enough to allow heat flux avalanches to be generated. They propagate through the regions where the shear is high and thus lead to a finite heat flux over nearly the whole radial domain. As the transition appears both if  $R/L_T$  or the collision frequency is increased, the mechanism causing this structure appears to be susceptible to both effects. Furthermore, the transposition of states over a significant time shows that the staircase structure has an, albeit small, stability. Very high collision frequencies do not allow the formation of even only a partial staircase. This is thought to explain the second shift at high collision frequencies in the threshold seen in Fig. 4.9 and the corresponding linear behaviour.

## 4.5. Conclusion

In this chapter the influence of collisions on the ion temperature gradient driven heat flux, close to the nonlinear threshold is examined. In particular the impact of collisions on the finite heat flux threshold is investigated, and the following results are obtained.

The decay of the zonal potential is examined in the Rosenbluth-Hinton test, and is compared with the analytical model of Ref. [35]. The numerically obtained zonal flow decay rates agree well with the analytic prediction for low collision frequencies, while higher frequencies yield somewhat less satisfactory results. Furthermore, the influence of

#### 4. Influence of collisions on the Finite Heat Flux Threshold

the safety factor and the inverse aspect ratio, and the remaining residual zonal flow not affected by collisions are reproduced.

The behaviour of the finite heat flux threshold is examined by an extensive scan in the temperature gradient length and the collision frequency. In the simulations generally two distinct states are visible: a state where turbulence is suppressed and the heat flux almost vanishes, and a state with a finite heat flux. For some parameters, a transposition of both states for a considerable time period is observed. Three different temperature gradient lengths that characterize the near threshold dynamics are identified: the gradient length of linear stability  $R/L_{T,\text{lin}}$ , the Dimits gradient length  $R/L_{T,\text{Dim}}$  and the finite heat flux threshold  $R/L_{T,\text{fh}}$ , where  $R/L_{T,\text{lin}} < R/L_{T,\text{Dim}} < R/L_{T,\text{fh}}$  applies. It is found that the influence of the collisions is most prominent in the region where  $R/L_{T,\text{Dim}} < R/L_T < R/L_{T,\text{fh}}$ . Here, only small changes in the collision frequency lead to a noticeable shift of the finite heat flux threshold towards lower  $R/L_T$ , while outside of this region, the influence of collisions is minimal and very high collision frequencies are required to produce a significant change of the heat flux. A comparison of the time spent in the vanishing heat flux state and the collisional zonal flow decay time, reveals that in the linear analysis the potential would have decayed substantially long before the end of the state is reached. For sufficiently small collision frequencies the zonal flow can, therefore, be driven against the collisional dissipation even when the heat flux is vanishingly small. Despite the reduction of the finite heat flux threshold with increasing collision frequency, it remains considerably larger compared to the interpolated Dimits threshold for collision frequencies relevant to current experiments.

For a fixed collision frequency, the shear rate of the longest wave length radial mode increases almost linearly with  $R/L_T$  up to the value of the finite heat flux threshold, for larger values a decay is observed. Only very high collision frequencies lead to a suppression of this behaviour. The latter decay suggests a saturation mechanism of the zonal flow directly related to the turbulence intensity. If the collision frequency is increased for a fixed  $R/L_T$ , the shear intensity stays relatively constant until the finite heat flux threshold is reached, then decays to a finite value for high collision frequencies. A small region, in temperature gradient lengths, above the finite heat flux threshold is found, where a high shear intensity is paired with a finite heat flux, indicating that the contemplation of only the shear intensity is not sufficient for an explanation of the finite heat flux threshold.

The radial profile of the  $E \times B$  shearing rate exhibits staircase formation. Fully developed staircases (i.e. box shaped shearing rates) are observed below the finite heat flux threshold and lead to a suppression of turbulence with a vanishing heat flux. Partially developed staircases (which have a sawtooth shape) allow the appearance of avalanches and lead to a finite heat flux. The latter are observed above the finite heat flux threshold, both in the direction of  $R/L_T$  and collision frequency. It was also observed that, although the transition from fully developed to partially developed staircase requires only small changes in the collision frequency at the corresponding  $R/L_T$ , very high collision frequencies were required to suppress the formation of partial staircases themselves. The examination of staircases provided a satisfying explanation for the behaviour of the finite heat flux

#### 4.5. Conclusion

threshold. Nevertheless, a model to explain the influence of collisions on the formation and behaviour of the staircases remains to be desired.



## 5. Zonal flow generation through self-interaction

Recent work [8, 9] has revealed that zonal flows in global ITG turbulence with adiabatic electrons self-organize in so-called staircase structures. These structures have subsequently been observed in gradient as well as flux driven flux tube simulations, and have been shown to affect the dynamics close to the nonlinear threshold of ITG turbulence [10, 11]. Furthermore, collisions at levels relevant to the experiment, do not prevent staircase formation [51]. However, to our knowledge, the existence of staircases has not been verified in turbulence simulations with kinetic electrons. Indeed, their existence in this case is non-trivial, since zonal flows are then generally found to be weaker compared with the adiabatic electron case. Consequently, it is unclear if staircases form under these more experimentally relevant conditions. In this chapter it will be shown that staircases are also obtained with kinetic electrons, but not for all cases. In studying the staircase formation with kinetic electrons a new mechanism for zonal flow drive is revealed: the self-interaction of a turbulent mode due to the double periodicity of a toroidal flux surface. The self-interaction is connected with the parallel boundary conditions and is not necessarily physical when obtained in a flux tube simulation with a small normalized Larmor radius. It will be shown that, when it does occur, it can have a profound effect on staircase formation and the heat flux behaviour close to the threshold. Furthermore, it will be argued that the self-interaction can indeed occur under some conditions.

This chapter is structured as follows. In Sec. 5.1, the self-interaction mechanism is discussed in detail. In Sec. 5.2 an initial numerical investigation of the heat conduction as a function of the temperature gradient length is presented. Small scale structures in the  $E \times B$  shearing rate are observed and their physical nature is discussed in Sec. 5.3, where they are linked to the self-interaction. Sec. 5.4 then investigates the parameter dependence of the self-interaction, and Sec. 5.5 exploits the gained knowledge to confirm the existence of staircases with kinetic electrons. In Sec. 5.6, the self-interaction mechanism is investigated in global simulations. The influence of collisions is examined in Sec. 5.7 and the use of electromagnetic simulations is detailed and tested in Sec. 5.8. A synopsis and concluding remarks are given in Sec. 5.9. A derivation of the drive due to the self-interaction can be found in App. B.

The core of this chapter is based on the publication of Ref. [96].

## 5.1. Zonal flow drive through self-interaction

In a tokamak, when following the field lines, the modes are twisted due to the magnetic shear. The ballooning transform [76], to which the flux tube description is closely related, incorporates this effect through the dependence of the radial wave vector on the poloidal angle. In the flux tube formulation [65] the same effect is present, albeit often hidden in the metric of the field aligned coordinates. For the ballooning transform the field line is extended to infinity, and the radial wave vector keeps increasing after one turn. In the flux tube formulation (employed in this study) the computational domain contains only one turn of the field line, with the parallel boundary conditions at the end point of the field line connecting the mode to a mode with a higher radial wave vector. This boundary condition is in essence equivalent to the increasing radial wave vector of the ballooning transform.

GKW [54], the code employed for the flux-tube simulations of this investigation, uses straight field line Hamada coordinates [63, 64]  $(\psi, \zeta, s)$ . Here  $\psi$  represents the flux label,  $\zeta$  is the binormal coordinate and  $s$  is the coordinate parallel to the field, where  $\zeta$  and  $s$  are normalized to obtain a computational domain  $\zeta \in [0, 1]$  and  $s \in [-1/2, 1/2]$  respectively. The high field side position is given by  $s = \pm 1/2$ . The double periodic boundary conditions for the phase-space distribution function ( $f$ ) on the toroidal flux surface then are

$$\begin{aligned} f(\psi, \zeta, s) &= f(\psi, \zeta + 1, s) \\ f(\psi, \zeta, s) &= f(\psi, \zeta - q, s + 1), \end{aligned} \quad (5.1)$$

where the first represents the periodicity in the toroidal and the second in the poloidal direction. The latter boundary condition takes into account that, when moving over one turn along the field ( $s = +1$ ), the binormal coordinate undergoes a change  $+q$ , where  $q$  is the safety factor.

The distribution function in the radial ( $\psi$ ) and binormal ( $\zeta$ ) direction is represented by Fourier modes

$$f = \sum_{\mathbf{k}} \hat{f}(k_\psi, k_\zeta, s) \exp[ik_\psi \psi + ik_\zeta \zeta] + c. c., \quad (5.2)$$

while the direction along the field line ( $s$ ) is treated in real space. A proper choice of the binormal wave vectors ( $k_\zeta$ ) leads to a periodic solution on the domain  $\zeta \in [0, 1]$  and the first condition of Eq. ((5.1)) is automatically satisfied. To fulfil the second condition, the safety factor is chosen such that  $q(0)k_\zeta = 2k\pi$ , with  $k = 1, 2, \dots$  in the centre ( $\psi = 0$ ) of the radial domain. Then the modes are resonant in the centre of the domain. This choice can be motivated by the high toroidal mode numbers of the ITG turbulence, leading to a resonant surface in close proximity to the local surface considered in the computation. Although the modes are resonant in the centre of the box, the magnetic shear  $\hat{s}$  must be considered. The change in the safety factor, taken as

$$q(\psi) = q(0) + \left. \frac{\partial q(\psi)}{\partial \psi} \right|_{\psi=0} \psi, \quad (5.3)$$

### 5.1. Zonal flow drive through self-interaction

leads to non-resonant modes away from the centre. Using this expression for the safety factor, it is possible to satisfy the second condition of Eq. ((5.1)) by imposing

$$\hat{f}(k_\psi, k_\zeta, \frac{1}{2}) = \hat{f}(k_\psi + k_\zeta \frac{\partial q}{\partial \psi}, k_\zeta, -\frac{1}{2}) \quad (5.4)$$

as the boundary condition in  $s$ -direction. This means that, at the end points of a field line, modes with a different radial wave vector ( $k_\psi$ ) couple. The shift in the radial wave vector is

$$\Delta k_\psi = k_\zeta \frac{\partial q}{\partial \psi} = k_\zeta \hat{s} \frac{q}{\epsilon}, \quad (5.5)$$

where  $\epsilon = r/R$  is the inverse aspect ratio. However, commonly the poloidal wave vector ( $k_\theta$ ) is used. The relation to the binormal wave vector depends on the employed geometry. For the circular concentric flux surfaces used in this work, the shift in terms of  $k_\theta$  becomes

$$\Delta k_\psi = k_\theta 2\pi \hat{s} \frac{q}{\epsilon} \frac{1 + \epsilon}{\left(1 + (q/\epsilon)^2 (1 - \epsilon^2)\right)^{1/2}}. \quad (5.6)$$

This shift is used to set up the  $k_\psi$  grid. In order to allow for equal resolution in radial and binormal direction, an integer  $i_k \approx 2\pi \hat{s}$  is introduced, so that the step size of the radial wave vector is  $\delta k_\psi = \Delta k_\psi / i_k$ . The boundary conditions as formulated above are globally consistent [67, 68].

From the discussion on the boundary conditions, the zonal flow drive through self-interaction can be understood easily. Consider an unstable ITG mode with a wave vector  $(k_\psi, k_\zeta)$ . Over the parallel boundary conditions this mode will connect with the  $(k_\psi \pm \Delta k_\psi, k_\zeta)$  mode, i.e. parallel streaming can transfer energy to higher or lower  $k_\psi$  modes. If a nonlinear interaction between the  $(k_\psi, k_\zeta)$  and  $(k_\psi \pm \Delta k_\psi, k_\zeta)$  modes can occur, it will transfer energy into the  $(2k_\psi \pm \Delta k_\psi, 2k_\zeta)$  as well as the  $(\pm \Delta k_\psi, 0)$  mode. The latter is a zonal mode and, as the shear-periodic boundary condition connects modes with a distinct difference in the radial wave vector, a zonal mode with the distinct radial wave vector  $\Delta k_\psi$  is driven. The self-interaction can therefore directly drive specific zonal modes. Several points should be noted. The self-interaction mechanism uses all radial modes with the same  $k_\zeta$  to drive the same distinct zonal mode. The  $(2k_\psi \pm \Delta k_\psi, 2k_\zeta)$  mode is driven generally only by one pair of modes.

The proposed self-interaction mechanism shares similarities with the familiar modulation instability [25, 97]. Both can be explained with a quadratic nonlinearity leading to wave interaction which drives the zonal mode. However, the physical mechanism of the self-interaction differs from the one of the modulation instability. There, the side bands grow exponentially due to the interaction of the zonal flow with the pump wave, leading to an exponential growth of the zonal flow, which is a smooth function of the radial wave vector. In the self-interaction mechanism, the side bands obtain their energy through the flow along the field lines and the mechanism drives zonal modes at distinct radial wave vectors. As such a mode is driven by all turbulent modes with the same  $k_\zeta$ , an effective invocation of feedback on the driving modes is not possible, so an algebraic rather than

### 5. Zonal flow generation through self-interaction

an exponential growth is observed, which is shown later on. Following from that, a 3D description is a mandatory requirement to obtain the self-interaction. It should also be mentioned that an interaction between the two modes must not necessarily occur in a turbulent plasma. Following a field line over one poloidal turn, it is in general shifted in the toroidal direction. At a fixed toroidal angle, the  $(0, k_\zeta)$  and  $(\pm\Delta k_\psi, k_\zeta)$  mode might be uncorrelated, thus yielding a zero time averaged drive.

As stated above, the boundary conditions applied in a flux tube are consistent with the double periodicity of the toroidal flux surface and a flux tube can describe the dynamics inside the flux surface without approximation. Nevertheless, an additional approximation is usually made in the case of a small normalized Larmor radius. In this case, the description of the turbulence on the whole flux surface would require a large amount of  $k_\zeta$  modes. In order to save computational resources it is assumed that the turbulence on a smaller wedge of the surface is equivalent to all other parts. Then the computational domain is represented by a part of the toroidal circumference and the first boundary condition of Eq. (5.1) is assumed to apply on this smaller domain (renormalizing  $\zeta$  such that the domain is still  $[0, 1]$ ). It must be stressed that this condition is of a different nature compared with the exact double periodic boundary condition described above. The boundary condition on the smaller domain can only be justified using a statistical argument, i.e. on average the turbulence on all the wedges is similar. Such an argument fails if the description of the physics processes demands that no correlation between the turbulence in the different wedges occurs [98]. The self-interaction is an effect that can be overestimated if the statistical argument is applied: If a small wedge is considered, following the field line for one poloidal turn will in general lead to a toroidal shift outside the domain of the wedge. The applied periodic boundary conditions on the  $\zeta$  domain map the perturbation back into the computational domain, possibly generating a spatially localized correlation between modes that do not exist on the full flux surface.

As a consequence, the self-interaction can only be properly calculated if the whole flux surface is considered. Of course, every flux tube simulation can be considered to describe a whole flux surface provided the normalized Larmor radius is large enough. However, experimentally relevant normalized Larmor radii require a large amount of binormal modes. Assuming that the turbulence requires the resolution of wave lengths up to  $k_\theta \rho \approx 1$ , with  $k_\theta \approx nq/r$  where  $n$  is the toroidal mode number,  $\rho$  the Larmor radius and  $r$  the radius of the poloidal flux surface, then a full surface simulation requires

$$N_\theta = \frac{r}{qR\rho_*} \quad (5.7)$$

$k_\theta$  modes. In the equation above  $\rho_* = \rho/R$ , with  $R$  being the major radius. So, for current day experiments  $N_\theta \geq 64$  is commonly assumed.

Furthermore, following the argument above, it might appear that the self-interaction has to be considered unphysical, as commonly, in adiabatic simulations, no correlation of the turbulent modes over long distances in the flux surface is found. However, if kinetic electrons are considered, turbulence does exhibit a correlation over long distances. To show this, the normalized correlation function  $C_N$  is evaluated for an adiabatic and

a kinetic standard simulation (see Sec. 5.2 for details on the numerical setup).  $C_N$  is determined using only the turbulent part (without the zonal mode) of the perturbed electrostatic potential, the values are averaged over a stationary turbulent period.

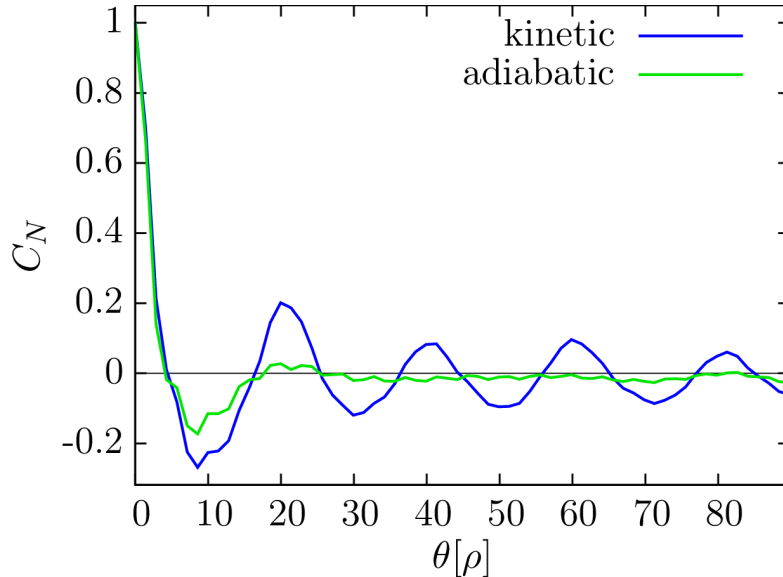


Figure 5.1.: Correlation function  $C_N$  in the binormal/poloidal direction summed over all radial modes for simulations with standard parameters and a grid G3 (see Sec. 5.2).

Fig. 5.1 shows the resulting correlation function in the binormal direction, summed over all radial modes. Here it is evident that, if kinetic electrons are considered,  $C_N$  does not go to (almost) zero, as in the adiabatic simulation. Instead, a finite value for long distances can be assumed. To back up this claim, the local maxima are fitted with a function of the form  $a + \exp(-b\theta)$  where a long range correlation of  $a = 0.052$  is found. This is attributed to the increased electron velocity. Similar results are also found for other simulations with different parameters or resolutions.

In this section the self-interaction mechanism has been discussed in some detail, as it will enter in the simulations discussed in the next section. The reason why it appears in simulations with kinetic electrons, but has not been observed in the simulations using adiabatic electrons, is the long extension of the mode structure along the field line in the kinetic electron case [99, 100]. This leads to an increased connection via the boundary conditions in the  $s$ -direction.

## 5.2. Heat flux near marginal stability

In this section a numerical investigation of the heat transport close to the nonlinear threshold of ITG turbulence with kinetic electrons is presented. The flux-tube version of

## 5. Zonal flow generation through self-interaction

	$N_\psi$	$N_\theta$	$N_s$	$N_\mu$	$N_{v_\parallel}$	$k_{\psi,\max}$	$k_{\theta,\max}$
G1	43	11	32	9	64	3.5	1.4
G2	83	21	32	9	64	3.4	1.4
G2-b	165	21	32	9	64	3.4	1.4
G3	165	41	16	9	64	3.4	1.4

Table 5.1.: Overview of used grid sizes.

the nonlinear Eulerian gyro-kinetic code GWK [54] is used in this study. The simulations are gradient driven, neglect plasma rotation as well as collisions, and have a standard parameter set compliant to the well known cyclone base case: safety factor  $q = 1.4$ , magnetic shear  $\hat{s} = 0.78$ , inverse aspect ratio  $\varepsilon = 0.19$ , and density gradient  $R/L_n = 2.2$ . Electrons are treated kinetically with an electron to ion-mass-ratio  $m_e/m_i = 2.72 \cdot 10^{-4}$  (deuterium). The temperature gradient ( $R/L_T$ ) is varied to investigate the heat flux close to the threshold value, and is in general smaller than the cyclone base case value due to the stronger instability connected with the kinetic electrons. Finally, electron and ion temperature ( $T$ ) as well as their gradients are chosen to have the same value, the standard value being  $R/L_T = 3.5$ . To reduce the computational cost, a small electron plasma beta  $\beta_e = 3 \cdot 10^{-4}$  is assumed so that the simulations retain the shear Alfvén wave physics. With this choice, the shear Alfvén wave propagates at a velocity comparable to the electron thermal speed, thus allowing an optimal time step. The impact of the electro-magnetic effects are checked and no significant differences in the heat flux or zonal flow dynamics compared with the pure electro-static case are found, more detail is given in Sec. 5.8.

To be compliant to the commonly used depictions, numerically obtained spectra are presented as a function of the poloidal rather than the binormal wave vector. The used grid sizes are shown in Tab. 5.1. Here,  $N_\psi$  ( $N_\theta$ ) is the number of radial (binormal/poloidal) modes,  $N_s$  the number of points along the magnetic field,  $N_\mu$  the number of points in the magnetic moment, and  $N_{v_\parallel}$  the number of points in the parallel velocity direction. The maximal radial and poloidal wave vectors are denoted by  $k_{\psi,\max}$  and  $k_{\theta,\max}$ . G1 is a grid with a reduced resolution and is assumed to exhibit some inadequacies. It is used in section 5.4 and section 5.5 as an additional comparison. G2 is the standard resolution used in most of the simulations, and G3 a high resolution case that is computationally demanding. G2-b is a variation used for an individual tests. To counteract the increased computational cost, the parallel resolution in the G3 case is reduced. To ensure that this reduction does not affect the results quantitatively in a noticeable manner, the so-called Rosenbluth-Hinton test [32] is employed. Here, the evolution of the residual zonal potential is investigated. Therefore two linear simulations with comparable parameters and a grid of  $N_\psi = 3$ ,  $N_\theta = 2$ ,  $N_\mu = 16$ ,  $N_{v_\parallel} = 64$  and  $N_s \in \{16, 32\}$  are carried out. The evolution of the zonal potential  $\phi_Z F(t)$  is used to calculate the residual value via an averaging of adjacent peaks of the overlaying GAM oscillation, similar to the procedure detailed in Chap. 4. The resulting residual potentials  $\phi_{\text{res}}$  are shown in Fig. 5.2. It has

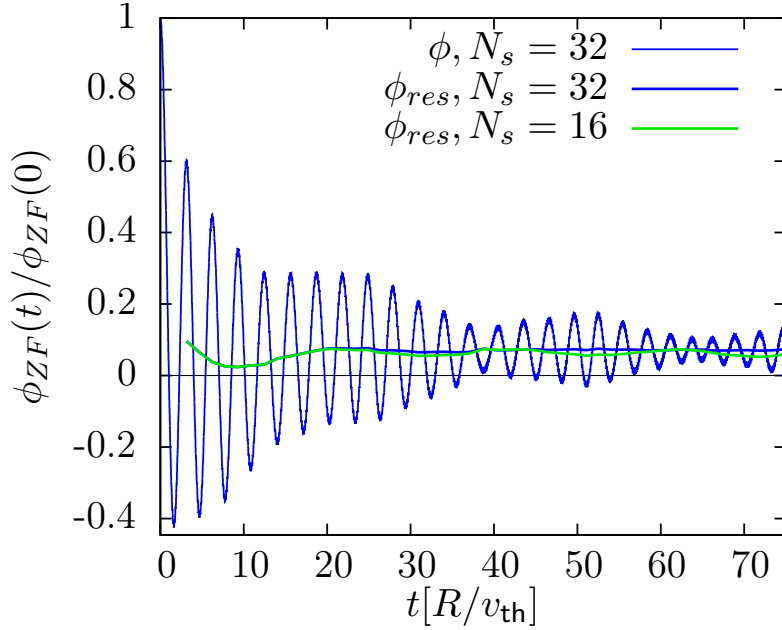


Figure 5.2.: Comparison of the influence of the resolution along the magnetic field. The residual potential  $\phi_{res}$  of linear simulations with  $N_s \in \{16, 32\}$  are shown. As comparison, the complete zonal potential  $\phi$  of the simulation with  $N_s = 32$  is shown.

to be noted that the maximum time range of this analysis is limited by the onset of the recurrence problem, which is determined by the employed resolution. Comparing  $\phi_{res}$  of both simulations, it can be deduced that the reduction of the number of grid points along the magnetic field does not lead to a significant damping of the residual potential. This analysis also guarantees that no over-damping occurs. All the wave vectors are given in relation to the Larmor radius  $\rho = m_d v_{th} / eB$  with  $m_d$  the deuterium mass,  $e$  the elementary charge,  $B$  the magnetic induction and  $v_{th} = \sqrt{2T/m_d}$  is the thermal velocity. Note that a factor two is used in the latter definition, and the thermal velocity is  $\sqrt{2}$  larger compared with the often employed sound speed. The size of the radial wave vector grid is determined by the condition of Eq. ((5.6)), where normally  $i_k = 5$  is used to ensure a comparable resolution in the radial and binormal direction. For the zonal mode the sixth order scheme along the magnetic field is used, the dissipation coefficients are  $D_x = 0.1$ ,  $D_y = 0.1$ ,  $D_s = 1$ , and  $D_{v_{\parallel}} = 0.2$  (see Ref. [11] for details on the implementation of the scheme and dissipation).

Fig. 5.3 shows the normalized ion heat conduction coefficient ( $\chi$ , normalized to  $\rho^2 v_{th} / R$ ) as a function of the ion temperature gradient length ( $R/L_T$ ). It is obtained from the time average over a sufficiently long stationary period. The curve with resolution G1 shows an appreciable difference from the G2 and G3 resolution cases, and it can be concluded that the resolution is insufficient to obtain accurate results. The G2 and G3 cases, however, are in good agreement, showing that the result is converged in these cases. In contrast to the simulations with adiabatic electrons [10, 11, 84], the heat flux

### 5. Zonal flow generation through self-interaction

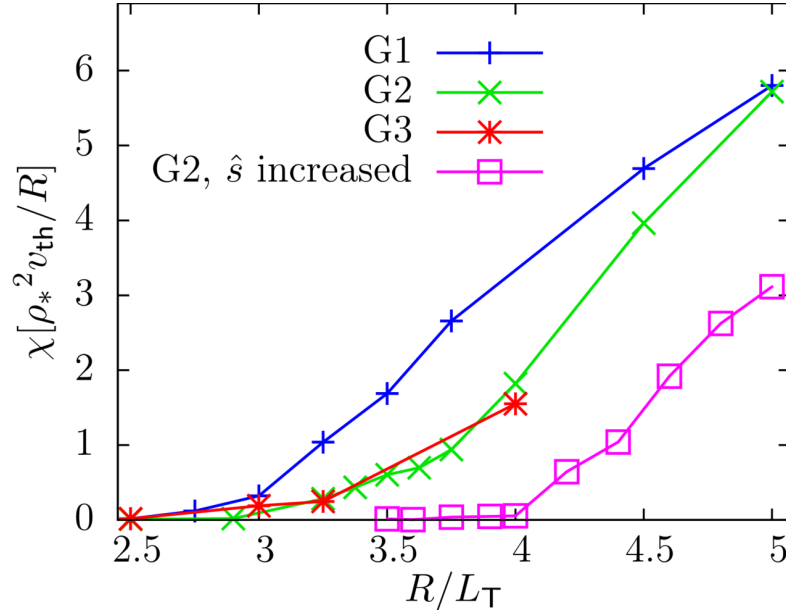


Figure 5.3.: Heat conductivity  $\chi$  averaged over a stationary period as a function of the temperature gradient length  $R/L_T$ . The results of simulations with the three different grid sizes (see table 5.1) are shown. Furthermore the results from simulations with an increased magnetic shear  $\hat{s}$  and resolution G2 are shown, further discussed in Sec. 5.5.

goes smoothly to zero, and there is no sign of a finite heat flux threshold. Note that  $\chi$  does not go linearly (estimated for  $\chi \gtrsim 1$ ) in  $R/L_T$  to zero, instead a flattening for small  $\chi$  is seen. Here, a small but finite heat conduction coefficient is found. In these cases, a late onset of a suppressed turbulent state is not anticipated, as considerably long simulations  $> 7000R/v_{th}$  do not exhibit signs of suppressed turbulence. The appearance of the finite heat flux threshold in the adiabatic electron case, in which a jump in the heat flux is observed at the threshold, is connected with a staircase structure in the  $E \times B$  shearing rate [11]. Just below the threshold, the staircase is fully developed and turbulence suppression occurs over the whole radial domain. At the threshold the radial profile of the structure changes with one of the crossings of the  $E \times B$  shearing rate through zero becoming less steep. At the latter location avalanches form, that then carry the heat through the regions of high  $E \times B$  shear. The smooth functional dependence of the heat conduction coefficient on the gradient length in the case of kinetic electrons suggests that staircases do not form in these cases.

To investigate this, the radial profile of the  $E \times B$  shear rate  $\omega_{E \times B} = \partial^2 \phi / \partial \psi^2 / 2B$  for the standard parameter set with  $R/L_T = 3.5$  is shown in Fig. 5.4. Here,  $\omega_{E \times B}$  is normalized with  $v_{th}/R$ , the potential is normalized with  $e/(\rho_* T)$ ,  $\psi$  is normalized with  $\rho_*$  and  $B$  with the field on the magnetic axis. It can be observed, that small scale fluctuations, that appear in quasi-periodic bunches, dominate the  $E \times B$  shearing profile. These small scale

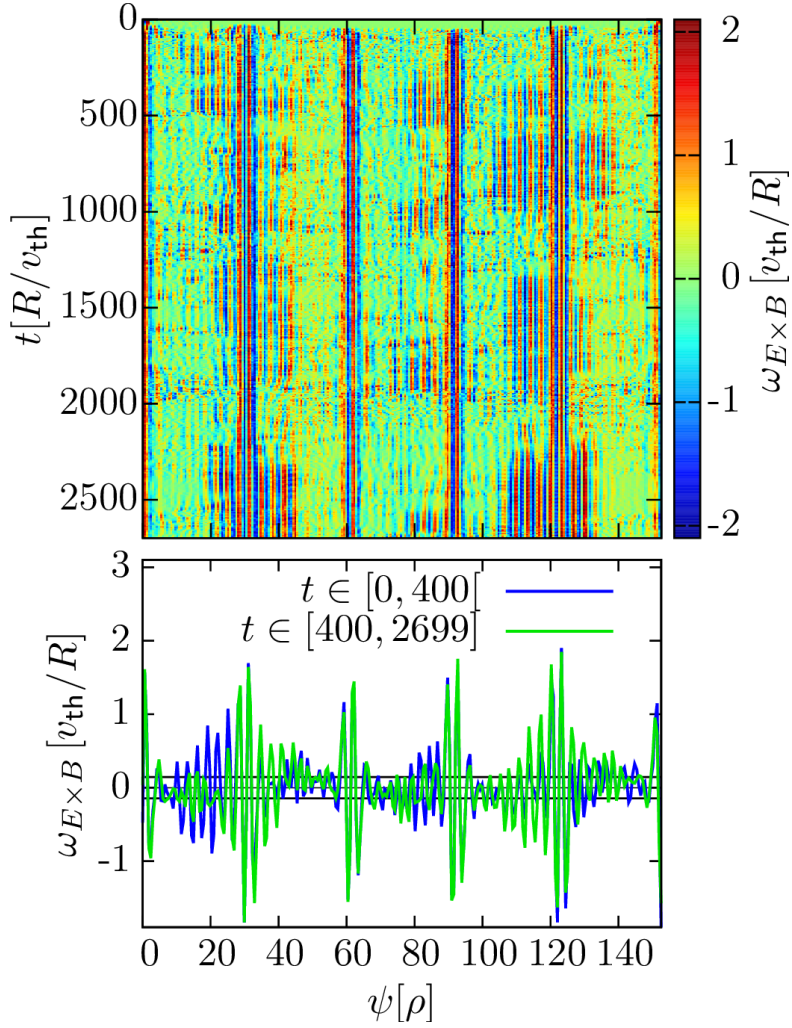


Figure 5.4.: Top: Evolution of the radial  $E \times B$  shearing profile  $\omega_{E \times B}$  for a simulation with the standard parameter set and grid size G3. Bottom: Averaged profiles in the initial and the stationary states respectively. The expected linear ITG growth rate of  $\gamma = 1.5 \cdot 10^{-1} v_{\text{th}}/R$  is indicated with black horizontal lines. Note that periodic boundary conditions apply in the radial direction.

structures are remarkably stationary in time, as is evident from the relatively large time interval over which the signals presented in Fig. 5.4 have been averaged. The amplitude of the small scale  $E \times B$  shearing rate structures is considerably larger than the ITG growth rate ( $\gamma = 1.5 \cdot 10^{-1} v_{\text{th}}/R$ ), indicated by the horizontal lines. These structures, therefore, do not stabilize the ITG as efficiently as the Waltz rule  $\omega_{E \times B} \approx \gamma$  would predict [49, 50], presumably due to their very short wavelength. In fact, it is at present unclear if any appreciable ITG stabilization is generated. It should be noted that the fine scale structure is relatively stationary and the reduced impact of shear stabilization can not

### 5. Zonal flow generation through self-interaction

be explained through a temporal dependence as in Ref. [48].

The behaviour described above is observed in all simulations that use standard parameters. A typical staircase structure cannot be made out in the radial shear profiles, even when attempting to filter out the small scale fluctuations. Although avalanches in the heat flux are observed (but not shown), these do not have starting or ending points at fixed radial positions, as is observed for the staircase structures obtained with adiabatic electrons [9–11, 84]. In conclusion, the dependence of the heat conduction on the gradient, the profile of the  $E \times B$  shear, and the radial distribution of avalanches all indicate that staircases do not form in these cases.

### 5.3. Physical nature of the small scale $\omega_{E \times B}$ structures

The small scale structures in the  $E \times B$  shearing rate are caused by the self-interaction connected with the parallel boundary conditions, which will be shown below. For that task, the results of a simulation with grid resolution G3 and the aforementioned standard parameters (with  $R/L_T = 3.5$ ) are discussed. After an initial linear phase, the simulations exhibits a quasi-stationary, turbulent state in which the self-interaction drives the distinct zonal modes. Fig. 5.5 shows the electric potential  $|\phi|$ , taken as a measurement of the mode intensity, in the  $k_\psi$ - $k_\theta$ -plane (only positive wave vectors are shown).

Here, several observations can be made. The ITG turbulence generates a maximum potential amplitude located at low  $k_\psi$  and  $k_\theta \rho \approx 0.35$ . The extended ITG mode structure along the magnetic field line, connected with the fast passing electrons, leads to the generation of a contribution at higher  $k_\psi$ . That the visible enhancement at higher  $k_\psi$  is due to the parallel boundary conditions is evident from the marks (white circles) indicating  $\Delta k_\psi$  given by Eq. ((5.6)) as a function of  $k_\theta$ . The nonlinear interaction between modes grouped around  $k_\psi \approx 0$  and those at  $k_\psi = \Delta k_\psi$  then drives the zonal mode, which can be seen as a discontinuous band at the bottom of the figure. Here, a correlation between the ITG-maximum and an exceptional strong drive of the zonal modes can be discerned.

The radial spectrum of the absolute value of the electrostatic potential  $|\phi|$  at  $k_\theta = 0$  is shown in Fig. 5.6 (mind the logarithmic scaling of  $k_\psi$  here). As discussed in Sec. 5.1 the self-interaction mechanism drives zonal flows with a distinct radial wave vector. Indeed, the spectrum in Fig. 5.6 shows spikes at distinct positions. Furthermore, these spikes coincide with the radial shift  $\Delta k_\psi$  due to the boundary conditions which are marked by the red vertical lines, indicating the modes driven through self-interaction. Moreover, if the relative size of the spikes is taken into account, the relation to the ITG-maximum is nicely visible. In Fig. 5.6 the radial spectrum of the  $E \times B$  shear rate is also depicted. It can be seen that the spikes at high  $k_\psi$  dominate the  $\omega_{E \times B}$  spectrum. This is consistent to the form of the radial shear profile presented in Fig. 5.4. The wave length of the small scale  $\omega_{E \times B}$  structures shown there is consistent with the shift  $\Delta k_\psi$  and are a direct consequence of the self-interaction mechanism.

### 5.3. Physical nature of the small scale $\omega_{E \times B}$ structures

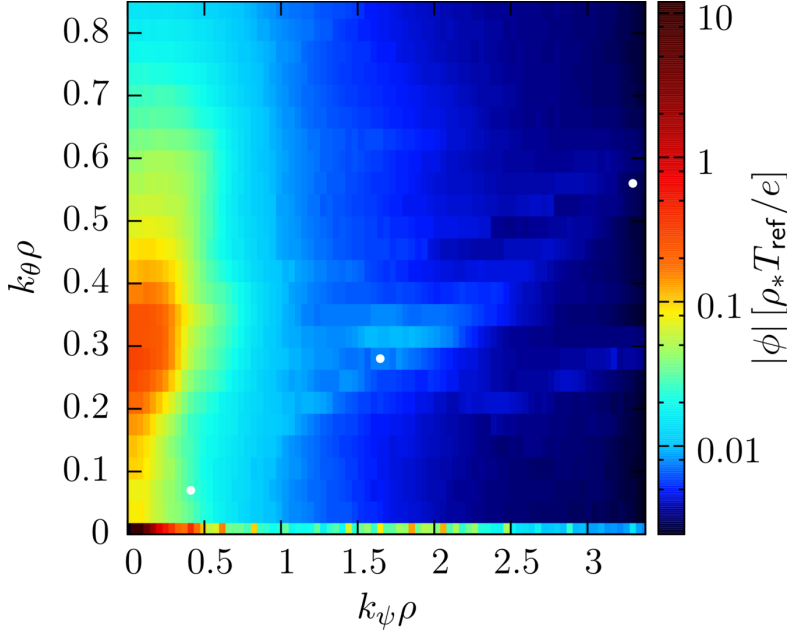


Figure 5.5.: Spectral slice in  $k_\psi$ - and  $k_\theta$ -direction of the electrostatic potential  $|\phi|$ , averaged over the stationary turbulent state. The simulation uses the standard parameter set and grid resolution G3. The radial shift given in Eq. ((5.6)) corresponding to each  $k_\theta$ , is indicated by the white circles. Take notice of the discontinuous behaviour of the zonal mode at the bottom of the figure and that only a portion of the spectral plane is shown.

Furthermore the question arises whether the intensity of the driving modes are in accordance with the growth of the spikes. Therefore, the required growth time  $t_G$  for the individual spikes is coarsely estimated by mimicking the mechanism of the self-interaction. Motivated by an analysis of the momentum balance between the Reynolds stress and the zonal flow vorticity,  $t_G$  for a zonal mode  $\phi_{ZF}$  driven by the modes at  $k_\theta$  is given as

$$t_G = \frac{|\phi_{ZF}(\Delta k_\psi, 0, s)|}{\sum_{k_\psi} k_\psi k_\theta |\phi(k_\psi, k_\theta, s)| |\phi(k_\psi + \Delta k_\psi, k_\theta, s)|}. \quad (5.8)$$

Here,  $\phi_{ZF}$  is taken as the size of the spikes  $\Delta|\phi|$  which are taken as the difference between the potential at the position of the spike and a logarithmic baseline. Generally, the two nearest points in each direction are taken to define the baseline. In a few cases, where this is not possible, only the adjacent points are used. It should be noted that due to turbulent fluctuations, this method becomes less exact for spikes being small in relation to the baseline, which can be anticipated for example in Fig. 5.6. These results are compared to the observed growth rates in a simulations with standard parameters and resolution G2. For this, the spikes are first suppressed, i.e. the modes determined via Eq. ((5.6)) are set to a vanishing value. Then the suppression is lifted and the mode grows to a stationary state. Results of this process are presented in Fig. 5.7. Here, the

### 5. Zonal flow generation through self-interaction

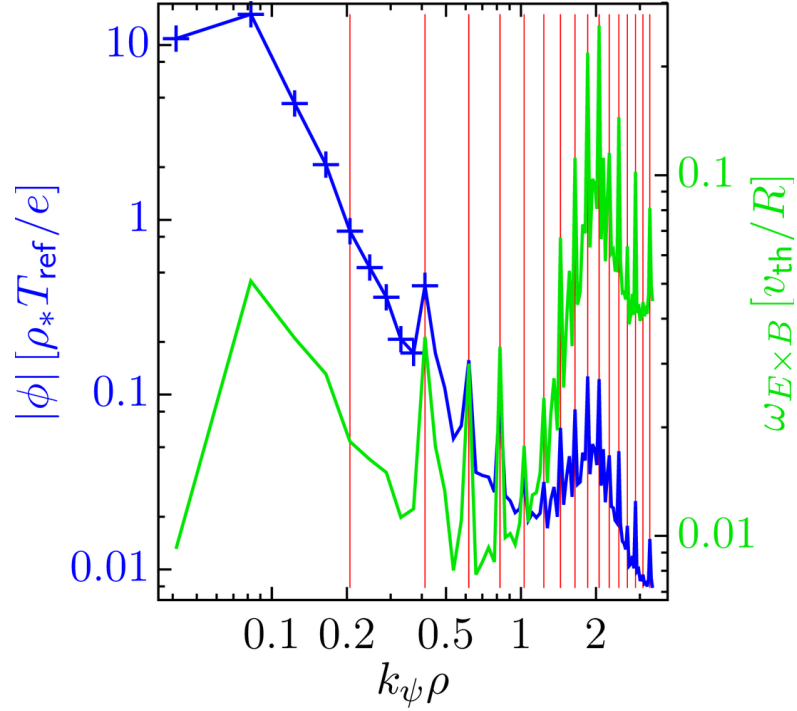


Figure 5.6.: Radial spectrum at  $k_\theta = 0$  of  $|\phi|$  (blue and corresponding to the left axis) and  $\omega_{E \times B}$  (green and corresponding to the right axis). It is averaged over the stationary state of a simulation with the standard parameter set and the grid G3.  $\Delta k_\psi$  is indicated with red vertical lines. Note the logarithmic scaling of  $k_\psi$  in comparison to Fig. 5.5.

evolution of the individually normalized electrostatic potential  $|\phi|/|\phi|_{\max}$  for some of the zonal modes that are resonant to the self-interaction after the suppression are depicted as an example. The end of the suppression occurs at  $t = 900 R/v_{\text{th}}$  and to indicate the later stationary state its average value is depicted as a horizontal line. The time needed for the mode to grow to the stationary state is found to be around  $100 R/v_{\text{th}}$  to  $150 R/v_{\text{th}}$ , which is well above the predicted growth time estimated with Eq. ((5.8)), being  $10 R/v_{\text{th}}$  to  $50 R/v_{\text{th}}$ . So it is concluded that the self-interaction mechanism is able to drive the observed spikes in the zonal mode. In Fig. 5.7 it can also be seen that the self-interaction leads to an algebraic growth and not to an exponential growth, with the latter being expected from the modulation instability.

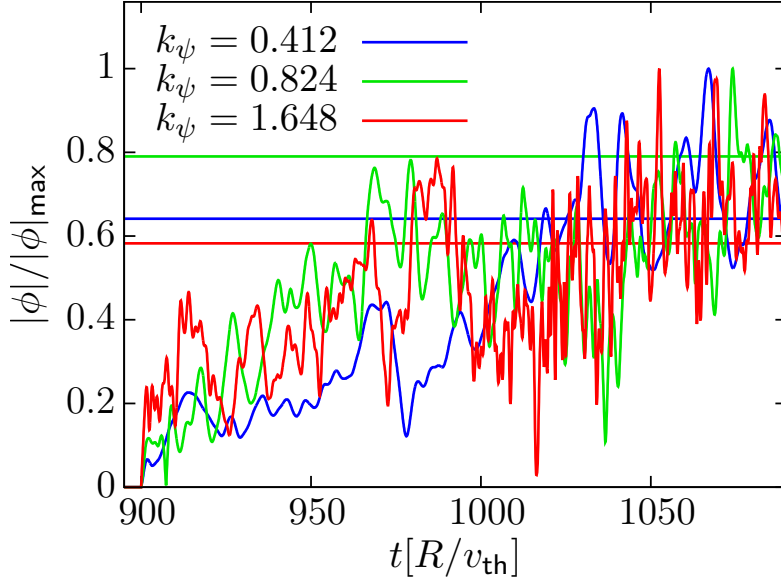


Figure 5.7.: Evolution of the individually normalized electrostatic potential  $|\phi|/|\phi|_{\max}$  after an initial suppression for some of the zonal modes that are resonant to the self-interaction. The end of the suppression occurs at  $t = 900R/v_{\text{th}}$ . As comparison, the corresponding average over the later stationary state is depicted as a horizontal line.

## 5.4. Parameter dependence of the self-interaction

The above result on small scale structures in the  $E \times B$  shearing rate raises several questions: Do they prevent the formation of a staircase structure, or is it merely an additional artefact? Is the self-interaction relevant for any experiment or future reactor? And if it is not relevant, do flux tube calculations produce inaccurate results because of these structures? To answer these questions the parameter dependence of the self-interaction is studied below.

In the discussion in Sec. 5.1 it was argued that every flux tube simulation can be thought of as correctly describing a whole flux surface, provided the normalized Larmor radius is chosen consistent with the computational domain. For the resolutions used in this chapter these normalized Larmor radii are G1:  $\rho_* = \rho/R = 1.9 \cdot 10^{-2}$ , G2:  $\rho_* = 9.5 \cdot 10^{-3}$ , G3:  $\rho_* = 4.75 \cdot 10^{-3}$ . Consequently, if one assumes to describe the entire flux surface, it cannot be assumed that the resolutions of the smaller grids represent current experiments, only the case G3 can be deemed relevant. From the discussion in Sec. 5.1 it is clear that one can expect the self-interaction to decrease with increasing device size, i.e. decreasing normalized Larmor radius. For the flux tube simulations the change in the normalized Larmor radius implies a large amount of modes. The scaling of the self-interaction with the number of modes can also be argued as follows: The potential perturbations are unaffected when the resolution in real space is doubled for a fixed box size. Parseval's

## 5. Zonal flow generation through self-interaction

theorem then states that that the turbulence intensity calculated by summing the Fourier amplitudes of all modes  $I \propto \sum_{\mathbf{k}} |\hat{\phi}|^2$  should be unaffected. If the resolution is doubled in binormal direction, the higher mode density in  $\mathbf{k}$ -space then implies that each of the modes carries an intensity that is two times smaller. Since the self-interaction is connected to the nonlinearity, it scales proportional to the intensity, and the drive of each of the spikes can be assumed to be two times smaller. Since the number of  $k_\theta$  modes that must be kept in the simulation of a full flux surface scales as  $1/\rho_*$ , it is expected that the intensity of the spikes is roughly proportional to the normalized Larmor radius. Note that the same argument does not directly apply to the doubling of resolution in the radial direction. Although doubling the resolution in this direction leads to a similar decrease in the turbulence intensity, all modes with the same  $k_\theta$  drive the same zonal flow mode with  $k_\psi = \Delta k_\psi$  and, consequently, the same amplitude in this mode can be expected.

The above mentioned scaling with the number of modes is shown in Fig. 5.8 where the resulting spike intensities  $\Delta|\phi|$  (see Sec. 5.3 for calculation) are depicted for the different resolutions (see Tab.5.1) used in this chapter. For the grids G2 and G3, beginning from small  $k_\psi$ , the spike size decreases, after a minimum at  $k_\psi \rho \approx 2$ , another maximum appears and then the  $\Delta|\phi|$  decreases again. The grid G1 has an insufficient  $k_\psi$ -resolution to show this behaviour. The behaviour of the grids G2 and G3 is in accordance with the binormal spectrum of  $\phi$ , summed in the radial direction. As already mentioned, the calculation of the spikes is tainted by turbulent fluctuations. This leads to small discrepancies and is taken as explanation for the (albeit very small) negative spike sizes found. Concluding from that, high spikes located at regions with a low turbulent baseline (region at  $k_\psi \rho \approx 2$ ) are deemed the most expressive in this analysis. If the results of the different grid sizes are compared, the expected decrease of the spike intensities with increasing resolution is observed. Comparing  $\Delta|\phi|$  for corresponding  $k_\psi$ , the relation between the grids G1 and G2 does exhibit an averaged relation of  $\Delta|\phi|_{G1}/\Delta|\phi|_{G2} \approx 2$ , which is found quite consistently over the whole  $k_\psi$  range. For the grids G2 and G3, again an averaged relation of  $\Delta|\phi|_{G2}/\Delta|\phi|_{G3} \approx 2$  is found, however deviations from that value for many points are found. These are attributed to turbulent fluctuations. The reduction in spike size for increasing resolutions suggests that at small  $\rho_*$  no significant self-interaction can occur. Still, at the resolution G3, which corresponds to a normalized Larmor radius of  $\rho_* = 4.75 \cdot 10^{-3}$ , the effect is remarkably strong as seen in Sec. 5.2 and Sec. 5.3, and a significantly large mode density (smaller  $\rho_*$ ) would be required to eliminate the small scale structures in the  $\omega_{E \times B}$  shearing rate. To test the aforementioned argument of the scaling, a simulation with standard parameters and resolution G2-b is used, the results are shown in Fig. 5.8. Here, compared to G2, the number of radial modes is doubled, the number of binormal modes is kept the same. Consequently, the strength of the spikes observed here is expected to be similar to the G2 case. If both results are compared, a sub-par agreement for spikes at lower  $k_\psi$  is found. It is assumed to be caused by the different resolutions in the radial and binormal direction having a higher influence on spikes that are small in relation to the baseline. The results at higher  $k_\psi$  do compare relatively well and are taken to be more credible as the relative spike size

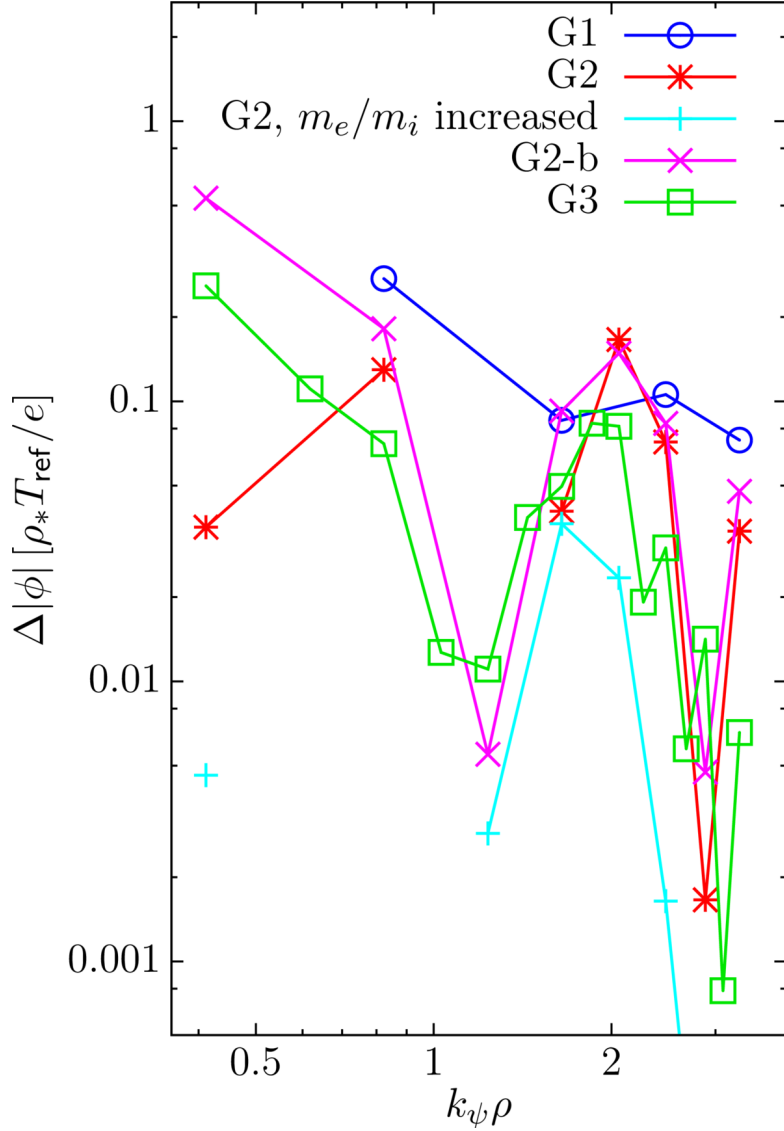


Figure 5.8.: Intensities of the spikes in the zonal mode caused by self-interaction. The simulations are using the standard parameter set, the four different grid sizes shown in table 5.1 are used. Furthermore, the results of a simulation with an increased  $m_e/m_i$  and the grid G2 are shown. Negative values are omitted and the neighbouring points are not connected.

is higher (compare for example in Fig. 5.6). Thus, the argument is assumed to hold in the framework of this analysis.

Furthermore, the influence of the electron-ion-mass-ratio of  $m_e/m_i$  is investigated. The self-interaction is caused by the long extension of the mode along the field line, which is connected to the large mobility of the electrons [99, 100]. As the electron mass is

### 5. Zonal flow generation through self-interaction

increased, the mode is more localized and the self-interaction is assumed be weaker. This is investigated with simulations on the grid G2 with the standard parameter set and an increased electron-ion-mass-ratio of  $m_e/m_i = 1.65 \cdot 10^{-2}$  and  $m_e/m_i = 1.0$ . In these simulations, a reduction in the intensity of the spikes is indeed observed. This is shown for  $m_e/m_i = 1.65 \cdot 10^{-2}$  in Fig. 5.8, where a clear reduction compared to the standard G2 case is visible, which proves the assumption.

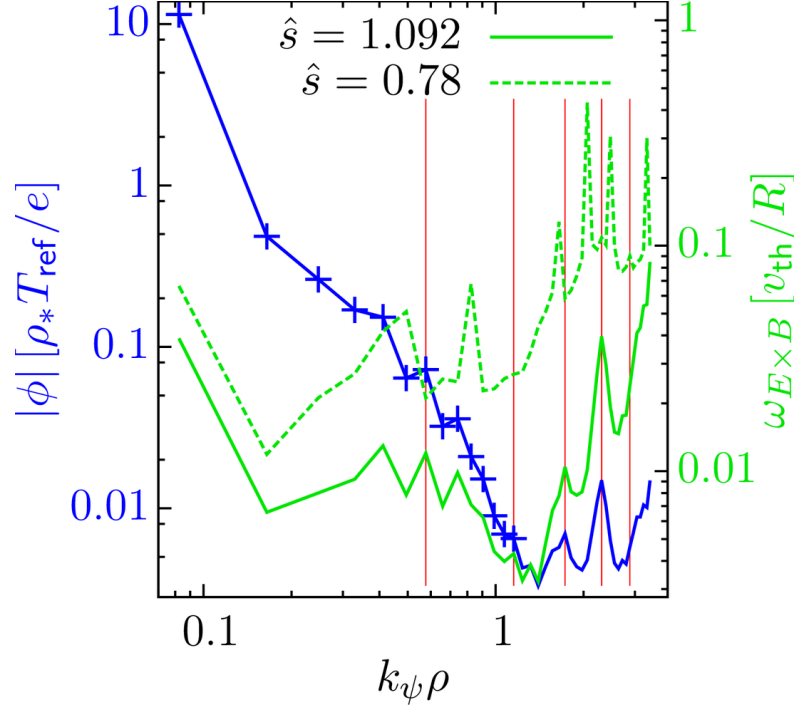


Figure 5.9.: Radial spectrum of the zonal potential (blue, corresponding to the left axis) and  $E \times B$  shear (green, corresponding to the right axis), averaged over a stationary state with suppressed turbulence. The simulations uses the grid G2 and the standard parameter set but with an increased magnetic shear of  $\hat{s} = 1.092$ . As comparison, the  $E \times B$  shear of a simulation with the standard parameter set is depicted.

The wave vectors of the driven zonal modes also depend on the value of the magnetic shear  $\hat{s}$ , as it is clear from Eq. ((5.6)). If the magnetic shear is varied, the wave vectors of the driven zonal flows should vary correspondingly. To test this impact, simulations for magnetic shear values  $\hat{s} \in \{0.156, 0.312, 1.092, 1.404\}$  have been performed with a grid resolution G2. The parameter  $i_{k_\psi}$  has to be adapted accordingly, using  $i_{k_\psi} \in \{1, 2, 7, 9\}$  for the respective shear cases. As an example, the radial spectrum of the electrostatic potential of a simulation with  $\hat{s} = 1.092$  is shown in Fig. 5.9. In this and all other simulations, the expected spike position, calculated following Eq. ((5.6)), is found to be in perfect agreement with the position of the spikes in the  $k_\psi$  spectrum of the zonal flows. Because  $i_{k_\psi}$  has to decrease for smaller values, the overall drive through self-interaction

increases, in turn decreasing the relative spike size (not shown). However, the influence on the radial shear profile remains and strong small scale structures dominate. The simulations with a higher  $\hat{s}$  show a smaller influence of self-interaction, which can be seen in Fig. 5.9. This especially concerns  $\omega_{E \times B}$  at higher  $k_\psi$ . Comparing  $\omega_{E \times B}$  of the simulation with  $\hat{s} = 1.092$  to a corresponding simulation with  $\hat{s} = 0.78$ , a reduction is visible. It is attributed to the lower density of modes that are affected by the self-interaction.

## 5.5. Staircase structures with kinetic electrons

The dependence on the magnetic shear allows the investigation of pattern formation in the  $E \times B$  shear avoiding, to some extent, the small scale structures. To exemplify this, a scan over  $R/L_T$  at  $\hat{s} = 1.092$ , which affects the ITG only slightly [101], is carried out. This leads to a reappearance of the staircase structure and most of the typical traits associated with it [11]. As an example, the evolution of the radial  $E \times B$  shear rate of a simulation at  $R/L_T = 3.6$  is depicted in Fig. 5.10 together with the evolution of the averaged heat conduction coefficient  $\chi$ . A clear correspondence between periods with a marked decrease of the small scale structures and a suppressed heat flux is visible. Eventually, an established stationary state with a suppressed heat flux is reached. Here, a staircase structure in the  $E \times B$  shear can be identified, as shown in Fig. 5.11. Correspondingly, the spikes in the radial spectrum are weak. Compared to adiabatic simulations a higher shear is found in the suppressed state which is attributed to the albeit small but still present small scale fluctuations.

Furthermore, a coincidence between this large scale structure and a radial localization of heat flux avalanches similar to the observations in adiabatic simulations [9–11] can be made out. To show this, the radial profile of the heat conductivity in the period where a staircase structure appears is shown in Fig. 5.11. Here avalanches can be observed, however they are considerably weaker compared to adiabatic simulations, as described in Ref. [102]. Nevertheless, a relation between the avalanche source- and sink-regions and the staircase is visible (mind the periodic boundary conditions): They emerge from the flank of the staircase at  $\psi \approx 15\rho$  and run towards a region at  $\psi \approx 50\rho - 60\rho$ . In accordance with the flattened flank, no exact sink-region can be identified. It should also be noted that the (local) strength of the avalanches coincides with local small scale perturbations of the staircase structure caused by self-interaction, visible for example around  $t \approx 2000v_{th}/R$ .

Also, the heat conductivity in the stationary state for varying  $R/L_T$  is examined, the results are shown in Fig. 5.3. A shift in the threshold compared to the simulations at  $\hat{s} = 0.78$  is visible. This is associated with the increased magnetic shear, leading to a weakening of the ITG instability. The typical abrupt drop in the heat flux cannot be made out. It should be noted that the simulations close to the threshold do exhibit short states with suppressed turbulence, however no final, i.e. long term, stationary state is observed despite long simulation times. If the curve for an increased  $\hat{s}$  is compared to

### 5. Zonal flow generation through self-interaction

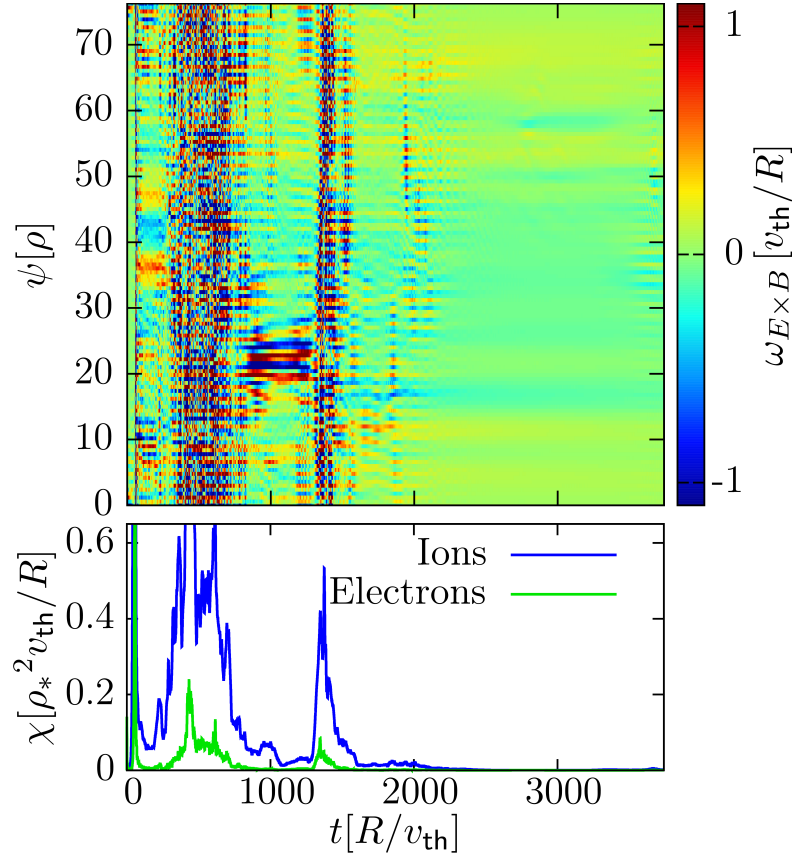


Figure 5.10.: Top: Time evolution of the radial  $E \times B$  shear profile  $\omega_{E \times B}$  of a simulation where the mechanism is weakened due to a different magnetic shear. It uses the grid size G2 and the standard parameters except  $\hat{s} = 1.092$  and  $R/L_T = 3.6$ . The colour range of  $\omega_{E \times B}$  is clipped to improve visibility. Bottom: Corresponding time evolution of the flux surface averaged heat conductivity  $\chi$ .

the results from standard parameters, a difference for small heat conductivities  $\chi \lesssim 1$  is visible. Where for standard parameters a small but finite  $\chi$  is found, for an increased  $\hat{s}$  the heat conductivity does go approximately linear to zero. This difference can be attributed to the appearance of the staircase structure and is backed by considerably long simulations.

It is concluded that staircase structures do form in simulations with kinetic electrons. The fact that the various signatures are only observed when reducing the self-interaction gives strong support to the idea that the small scale  $E \times B$  shearing rate structures prevent the formation of staircases. Why the observed small scale structures do not suppress turbulence as efficiently as large scale structures can not be answered in the scope of this analysis, however it will be a topic of future work.

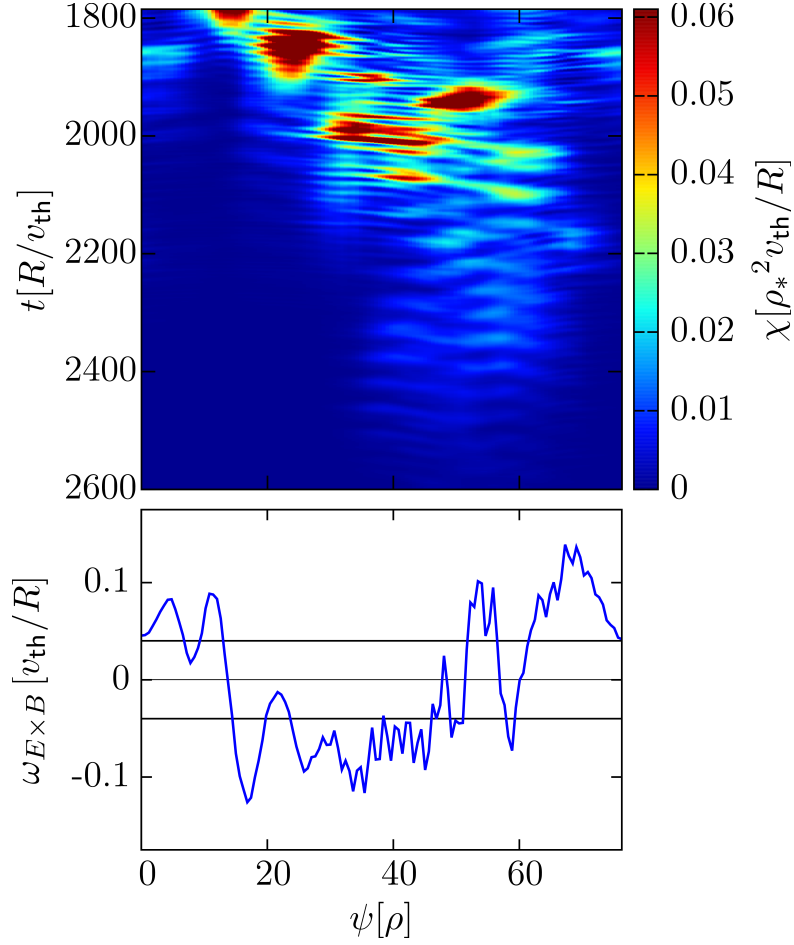


Figure 5.11.: Top: Radial heat conductivity profile of a simulation with  $\hat{s} = 1.092$  and  $R/L_T = 3.6$  on a grid G2. Bottom: Corresponding radial  $E \times B$  shear profile averaged over a stationary period. Mind the periodic boundary conditions.

## 5.6. Self-interaction in global simulations

Furthermore the question arises, in what way the self-interaction is observed in global simulations. This question is motivated as follows. The mechanism of the self-interaction requires the coupling of radial modes through the boundary conditions along a field line. These depend on  $q$ , which is taken to be constant in a flux-tube simulation, whereas in a global simulation,  $q$  varies over the radius. Consequently, the coupling also varies with the radius which could influence the self-interaction mechanism. It should also be stressed that all investigations of the self-interaction beforehand were carried out with the radial domain represented spectrally. In a global simulation this is not the case, therefore global simulations would allow to test, if the self-interaction mechanism is (unphysically) influenced by the choice of a spectral representation. To answer these questions, a global

## 5. Zonal flow generation through self-interaction

simulation is carried out.

The numerical investigation is performed with GKW [54] in the global version with the following parameters: Number of radial points  $N_x = 384$ , number of binormal modes  $N_\zeta = 24$ , number of points along the field line  $N_s = 16$ , number of points in the magnetic moment  $N_\mu = 18$ , number of points in the parallel velocity  $N_{v,\parallel} = 16$ . To correspond to the previously discussed simulations, an electromagnetic simulation with kinetic electrons and no plasma rotation is carried out. Electrons are treated kinetically with an electron to ion-mass-ratio  $m_e/m_i = 5.69 \cdot 10^{-4}$ . A small electron plasma beta  $\beta_e = 3 \cdot 10^{-4}$  is assumed so that the simulation retains the shear Alfvén wave physics to reduce the computational costs. In contrast to flux tube simulations, background profiles of the common parameters are specified, they are shown in Fig. 5.12. They are chosen to generate a simulation comparable to the previously studied local analyses. A small collision frequency is introduced to ensure computational stability. Therefore following parameters are chosen:  $n_{\text{ref}} = 1.0$ ,  $T_{\text{ref}} = 1.0$ ,  $R_{\text{ref}} = 1.0$ , resulting in the collision frequencies  $\nu_{ii} \approx 7 \cdot 10^{-4}$ ,  $\nu_{ie} \approx 7 \cdot 10^{-4}$  and  $\nu_{ee} = 3 \cdot 10^{-4}$ .

The simulation exhibits a non-vanishing heat flux  $Q$  as shown in Fig. 5.13. One has to be careful, as the time scale of this simulation might not be long enough to exhibit the formation of a fully-developed staircase structure, which can take considerable time as shown before and in Refs. [10, 11]. More insight in the long time behaviour can be gained from the observation of the radial shear profile. The radial shear is calculated similar to the local limit, however now, Dirichlet boundary conditions are assumed. The resulting shear is shown in Fig. 5.14. Here, the strong small scale structures typical for the self-interaction are observed. This shows that the self-interaction is also found when  $q$  and  $\hat{s}$  are not assumed to be constant. The strength of the small scale structures indicates that the formation of a staircase will most likely not be observed later on and the turbulence will not be suppressed. Additionally, the low order rationals of  $q$  are indicated as red vertical lines in Fig. 5.14. However no conclusive correlation between the position of the low order rationals and the small scale structures can be found.

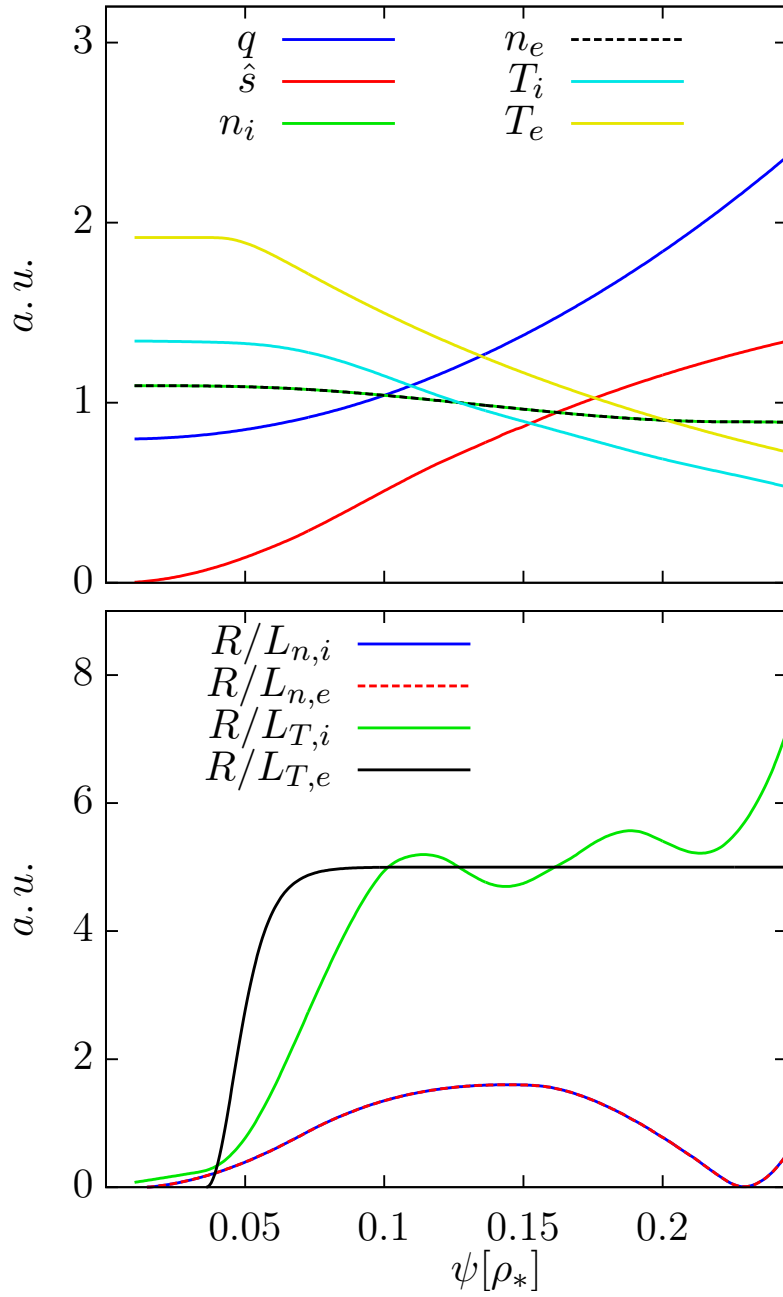


Figure 5.12.: Background profiles of the parameters used in the global analysis. Note that the parallel rotation gradient  $u'$  is zero for both species (not shown) and the profiles of  $R/L_{n,i}$  and  $R/L_{n,e}$  are identical.

5. Zonal flow generation through self-interaction

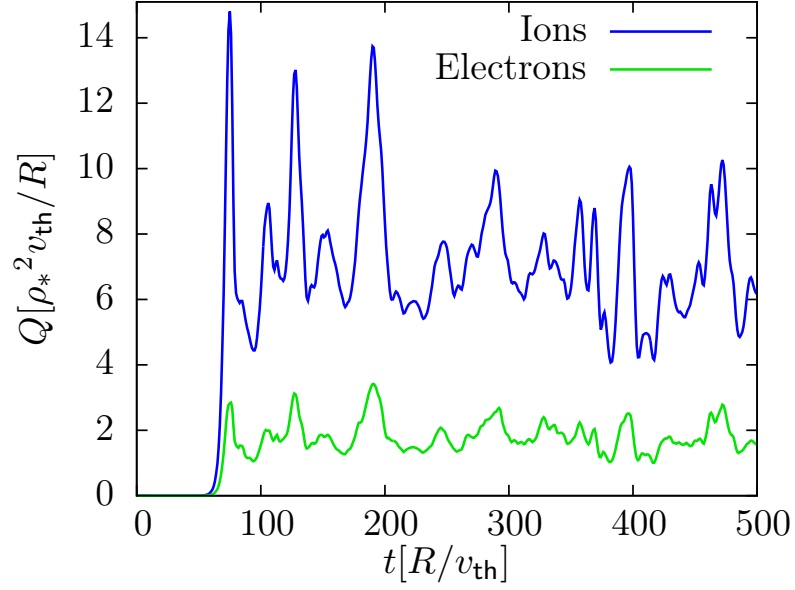


Figure 5.13.: Radially averaged heat flux  $Q$  for ions and electrons.

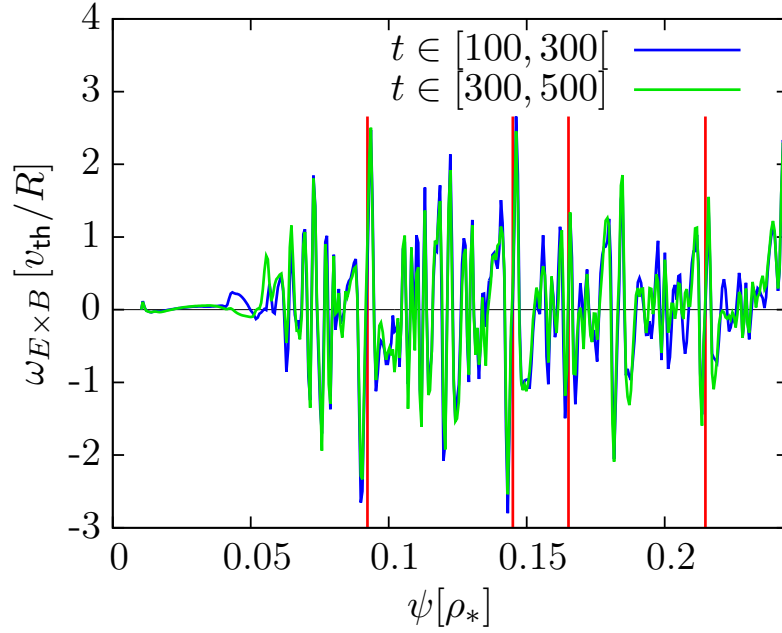


Figure 5.14.: Radial shear averaged in parts of the turbulent period for a global simulation. The position of the low order rationals of  $q \in \{1, 4/3, 3/2, 2\}$  (in that order) are indicated as red vertical lines (see Fig. 5.12).

## 5.7. Self-interaction influenced by collisions

The analysis presented in Chap. 4 shows that the structure formation in the radial  $E \times B$  shear is influenced by collisions. Therefore the question arises, whether and how the small scale structures driven by the self-interaction are affected by collisions. To investigate this, simulations with the standard parameter set and with the additional consideration of collisions are carried out on the grid G2. The parameters related to collisions are:  $n_{\text{ref}} \in \{0.5, 3.0\}$ ,  $T_{\text{ref}} = 1.0$ ,  $R_{\text{ref}} = 1.0$ . They result in the collision frequencies  $\nu_{ii} \in \{6 \cdot 10^{-4}, 3 \cdot 10^{-3}\}$ ,  $\nu_{ie} \in \{5 \cdot 10^{-4}, 3 \cdot 10^{-3}\}$  and  $\nu_{ii} \in \{5 \cdot 10^{-4}, 3 \cdot 10^{-3}\}$ .

The simulations do not exhibit significant changes compared to the collisionless simulations. The small scale structures dominate the radial profiles, characteristic staircase structures cannot be made out and no state with suppressed turbulence is observed, which will be detailed in the following. In Fig. 5.15, the radial spectra of the electrostatic potential and the  $E \times B$  shear of the simulation with the higher collision frequencies (with  $n_{\text{ref}} = 3.0$ ), are shown. For comparison, the spectra of a collisionless, but otherwise similar

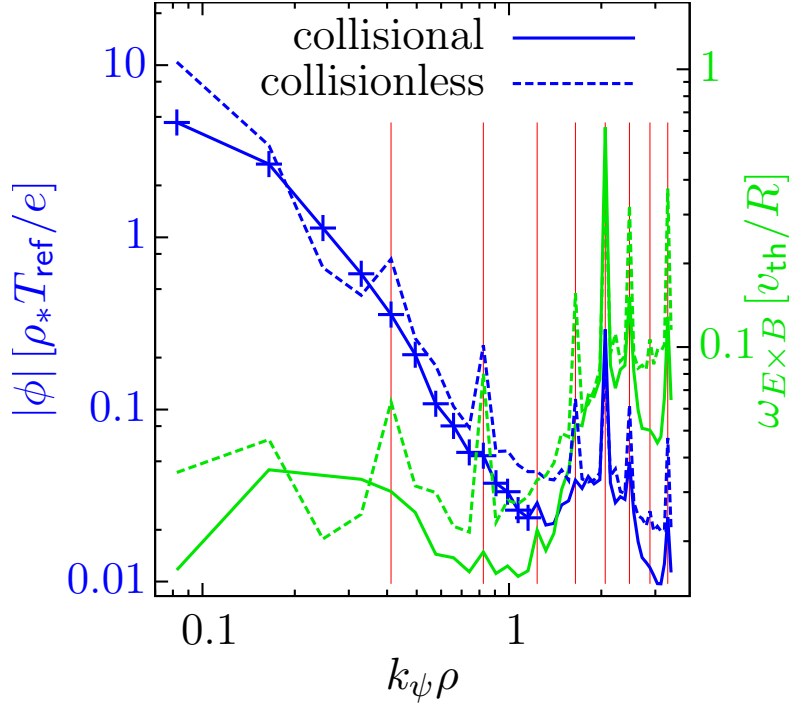


Figure 5.15.: Radial spectrum at  $k_\theta = 0$  of  $|\phi|$  (blue and corresponding to the left axis) and  $\omega_{E \times B}$  (green and corresponding to the right axis), averaged over the stationary state for an electrostatic simulation with grid G2.  $\Delta k_\psi$  is indicated with red vertical lines. For comparison, the potential and shear of a collisionless simulation with corresponding parameters are shown with dashed lines.

simulation is also depicted. It can be seen that the modes driven by the self-interaction

### 5. Zonal flow generation through self-interaction

mechanism at lower wave vectors are damped relatively strongly by collisions, whereas the modes at higher  $k_\psi$  are damped only slightly. Consequently, a large scale modulation in the shear is observable only weakly. The small scale structures dominate in the corresponding radial shear profile, which is shown in Fig. 5.16. In this profile, hints of staircase

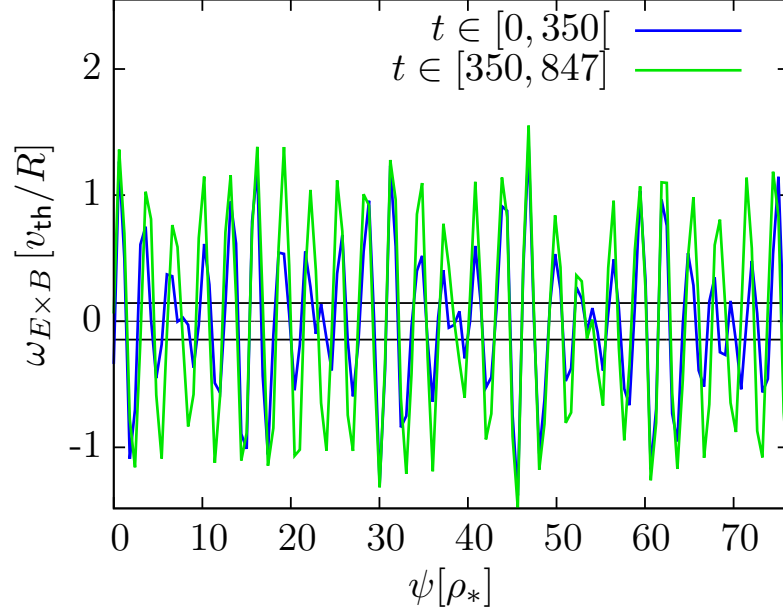


Figure 5.16.: Averaged radial shear profile of a simulation with the standard parameter set and  $n_{\text{ref}} = 3.0$ . The linear growth rate of the ITG is indicated by black vertical lines.

formation, i.e. a partial staircase, are not observed. In accordance to these findings, no suppression of turbulence is seen and a reduced heat flux is not measured. Due to no significant weakening of the small scale structures in combination with the damping of large scale structures (the scale of the staircase) and no sign of a partially developed staircase, it is concluded that the formation of a fully developed staircase at later times is not possible.

Comparing to these results, the simulation with lower collision frequencies (with  $n_{\text{ref}} = 0.5$ ) shows the effects mentioned above in a less pronounced manner. indications on the formation of a staircase are not observed as this shear profile is also dominated by small scale structures. For similar reasons as mentioned above it is again concluded that the formation of a staircase at later times is not possible.

In conclusion it is found that collisions do not damp the small scale structures significantly, whereas structures at larger scales, akin to staircases, are affected more strongly. Taking the analysis of Chap. 4 into account, it can be concluded that regimes with collision frequencies strong enough to damp the small scale structures will not exhibit staircase formation either. In regimes with small collision frequencies, the damping of the small

scale structures can be neglected. Therefore, the formation of staircases in the kinetic electron picture is not aided by the consideration of collisions.

## 5.8. Reduced time step in the electromagnetic picture

Here, the use of (slightly) electromagnetic simulations, i.e. a small plasma- $\beta \neq 0$ , to reduce the required time step, will be briefly explained and examined. The use of  $\beta \neq 0$  raises the question whether this has an influence on the observed generation of the small scale structures. Therefore, a short investigation of the self-interaction in the electrostatic picture, where  $\beta = 0$ , follows.

The shear Alfvén wave is a propagating displacement of the particles in the direction perpendicular to the magnetic field. The restoring force of the oscillation is provided by the magnetic field, a bent field line exerting a force  $B \cdot \nabla B$  towards the centre of the osculating circle. A simplified analysis in the MHD-picture, found for example in Ref. [6], shows that the Alfvén wave travels along the magnetic field with the Alfvén velocity

$$v_A = \frac{B}{\sqrt{\mu_0 \varrho}} \propto \frac{1}{\sqrt{\beta}}, \quad (5.9)$$

with the magnetic permeability  $\mu_0$  and the mass density of the fluid  $\varrho$  (cgs). Consequently, a very small  $\beta$  leads to fast shear Alfvén waves. Following the Courant-Friedrichs-Lewy condition [62], this would require a very small time step to properly describe shear Alfvén waves physics. Furthermore, (electromagnetic) shear Alfvén waves physics are required, as otherwise, the kinetic version of the Alfvén wave converts into an electrostatic electron thermal wave at small perpendicular length scales, where its velocity changes from the Alfvén velocity to the thermal electron velocity. Again, this would require a smaller time step, increasing the required numerical resources. On the other hand, a relatively large  $\beta$  would lead to the appearance of noticeable electromagnetic effects relevant for transport. Consequently, a small  $\beta$  will suppress the electrostatic shear Alfvén wave which allows a bigger time step, but does not lead to relevant electromagnetic effects [103].

To investigate, whether the small plasma  $\beta$  used in this investigation, might influence the self-interaction mechanism, a comparable simulation in the electrostatic limit is carried out. Otherwise the simulation uses the standard parameter set and the grid G2. For the grid G2, the choice of an electrostatic simulation already leads to a decrease of the required time step by a factor of  $\approx 2.5$ . The simulation also shows the distinct drive of the resonant modes through self-interaction, presented in Fig. 5.17. Here, no qualitative differences to the electromagnetic cases, also shown in Fig. 5.17 as dashed lines or in Fig 5.6, can be found. A comparison of the spike intensities (see Sec. 5.3 for calculation) shows also shows no qualitative differences. In accordance to this, the resulting small scale structures in the radial shear profile are found and no suppression of the heat flux is observed. This investigation leads to the conclusion that the use of a small plasma- $\beta \neq 0$  does not influence the results of the analysis presented in this chapter.

## 5. Zonal flow generation through self-interaction

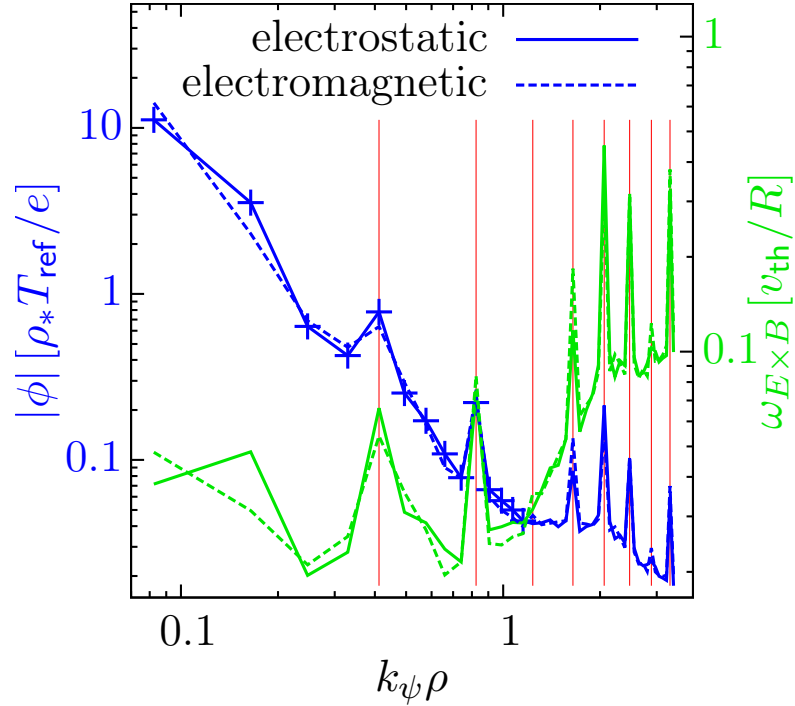


Figure 5.17.: Radial spectrum at  $k_\theta = 0$  of  $|\phi|$  (blue and corresponding to the left axis) and  $\omega_{E \times B}$  (green and corresponding to the right axis), averaged over the stationary state for an electrostatic simulation with grid G2.  $\Delta k_\psi$  is indicated with red vertical lines. For comparison, the potential and shear of an electromagnetic simulation with corresponding parameters are shown with dashed lines (blue and green).

## 5.9. Conclusion

In this chapter staircase structures are shown to develop in gyro-kinetic simulations with kinetic electrons. Staircases, however, do not develop under all circumstances. In many cases a large amplitude small scale structure in the  $E \times B$  shearing rate is observed, and in these cases no staircase structure can be identified. The heat flux then goes smoothly to zero when reducing the temperature gradient length, and no radial localization of avalanches is observed. The small scale  $E \times B$  shearing rate structures are interpreted to disrupt the formation of the larger scale staircase structures. This interpretation is empirically obtained since there is at present no convincing explanation for the staircase formation.

The small scale structures observed in the  $E \times B$  shearing rate are interpreted as being driven by the self-interaction of turbulent modes that is generated over the periodic boundary conditions of the double periodic torus. While the ITG mode with adiabatic electrons is localized along the magnetic field, and shows no appreciable self-interaction, the mechanism is present in the case of kinetic electrons due to the extended mode structure. A proper numerical evaluation of the effect can only be obtained when the

whole flux surface is treated, and consequently a flux tube simulation that covers only part of the toroidal circumference can produce spurious results near the nonlinear threshold of turbulence generation. The self-interaction is shown to decrease with the number of toroidal modes kept in the simulation, and for a full flux surface simulation scales proportional to  $\rho_*$ . It is to be expected that the effect is small in a reactor plasma, but at  $\rho_* = 5 \cdot 10^{-3}$  it is still dominantly present and it is therefore likely that it is of importance to present day experiments. Also the magnetic shear is observed to affect the results through their impact on the boundary conditions. This dependence was utilized to generate conditions under which staircases can be observed to form. In global simulations, the strong small scale structures are observed, indicating that the self-interaction is not limited to the local approximation. To complement these investigations, the influence of collisions on the self-interaction mechanism and the resulting structures are examined. These structures are found to be affected only slightly by collisions compared to the staircase structures that are observed in Chap. 4. The entirety of the carried out investigations leads to the conclusion that the self-interaction is a relatively robust mechanism.



## 6. Suppression of ITG due to structures in the zonal flow

It is widely known that ITG turbulence is regulated through structures in the zonal flow [8–11, 51, 84]. The self-organization of the  $E \times B$  shear flow into staircases [8], can lead to the emergence of a state with suppressed turbulence and a strongly reduced heat flux as shown in as shown in Ref. [11], where a finite threshold in the heat flux was observed as a result of staircase formation. Subsequent analyses investigated the influence of collisions, the impact of momentum transport and tertiary instabilities [36, 84, 104]. A further analysis of staircase formation using the kinetic electron response [96], showed that, through the so-called self-interaction, structures with high shearing rates and small wavelengths are generated in the zonal flow. However, these structures do not damp the turbulence sufficiently to establish a state with suppressed turbulence. This observation raises the question, how the wavelength of the structures that form in the zonal flow impacts the regulations of turbulence. In the analysis presented here, this question is investigated.

The method to measure the suppression of turbulence can be summarized as follows: A simulation is run until a stationary state is observed. This ensures that the structure formation in the zonal flow has advanced sufficiently. Then, the turbulence but not the zonal flow (or only a part of it) is quenched, i.e. set to a value that is small in comparison to the initial values used in the simulations. After that, the turbulence is allowed to re-establish, while the zonal flow (or a modified version of it) which has not been quenched, is kept fixed. This ensures that a subsequent decay of the zonal flow due to an absent drive does not affect the results. Here, a (mostly) linear period, with behaviour similar to the initial evolution of a simulation, is observed. In this period, the amplitude of the modes is relatively small, therefore the nonlinear interactions can be neglected. Consequently, the modes grow nearly exponentially in this period. In this linear period, the remaining zonal flow damps the exponential growth of the modes. By varying its radial structure, i.e. using only certain modes of the zonal flow, it is possible to gain insights on how the structure of the zonal flow affects the growth of the ITG.

### 6.1. Numerical setup

The simulations are carried out with the spectral flux-tube version of the nonlinear Eulerian gyro-kinetic code GKW [54]. They are gradient driven, neglect plasma rotation

## 6. Suppression of ITG due to structures in the zonal flow

as well as collisions, and have a standard parameter set compliant to the well known cyclone base case: safety factor  $q = 1.4$ , magnetic shear  $\hat{s} = 0.78$ , inverse aspect ratio  $\varepsilon = 0.19$ , and density gradient  $R/L_n = 2.2$ . Electrons are either treated in the adiabatic limit (adiabatically) or as a separate kinetic species (kinetically) with an electron to ion-mass-ratio of  $m_e/m_i = 2.72 \cdot 10^{-4}$  (deuterium). A temperature gradient of  $R/L_T = 6.9$  for the adiabatic cases and a  $R/L_T = 3.5$  for the kinetic cases is used. These values are chosen to ensure a comparable turbulent behaviour of both simulation types, as both values of  $R/L_T$  are located slightly above the respective thresholds [11, 84, 96]. However, care has to be taken if adiabatic and kinetic simulations are compared in a quantitative manner. Electron and ion temperature ( $T$ ) as well as their gradients are chosen to have the same value. To reduce the computational cost in the kinetic case, a small electron plasma beta  $\beta_e = 3 \cdot 10^{-4}$  is assumed so that the simulations retain the shear Alfvén wave physics. With this choice, the shear Alfvén wave propagates at a velocity comparable to the electron thermal speed, thus allowing an optimal time step without affecting the desired behaviour, as shown in Chap. 5. The used grid size is: the number of radial modes  $N_\psi = 83$ , the number of Binormal modes  $N_\theta = 21$ , the number of points along the magnetic field  $N_s = 32$ , the number of points in the magnetic moment  $N_\mu = 9$ , the number of points in the parallel velocity direction  $N_{v_\parallel} = 64$  and the maximal radial wave vector is  $k_{\psi, \max} = 1.4$ . All the wave vectors are given in relation to the Larmor radius  $\rho = m_d v_{th} / eB$  with  $m_d$  the deuterium mass,  $e$  the elementary charge,  $B$  the magnetic induction and  $v_{th} = \sqrt{2T/m_d}$  is the thermal velocity. Note that the thermal velocity is  $\sqrt{2}$  larger compared with the often employed sound speed. The size of the radial wave vector grid is determined by the condition that modes connected through the boundary along the field line can be represented on the grid, see Chap. 5 for details. To ensure a comparable resolution in the radial and the binormal direction albeit this condition, the integer factor  $i_k = 5$  is used [78]. For the zonal mode the sixth order scheme along the magnetic field is used, the dissipation coefficients are  $D_x = 0.1$ ,  $D_y = 0.1$ ,  $D_s = 1$ , and  $D_{v_\parallel} = 0.2$  (see Ref. [11] for details on the implementation of the scheme and the dissipation).

A linear analysis is carried out to examine the undamped growth rates in the adiabatic and kinetic case. Therefore, the aforementioned parameters are used, however, the nonlinear terms in the gyro-kinetic equation are neglected. The results are depicted in Fig. 6.1, where the binormal spectra of the growth rate  $\gamma$  and the dominant frequency  $\omega$  in the adiabatic and kinetic case, are shown. In the kinetic electron case (green), the trapped electron mode (TEM), distinguishable by a negative mode frequency for higher  $k_\theta$  [105–107] influences the spectrum.

To change the form of the zonal flow, parts of it are disregarded by setting the corresponding modes to zero. To illustrate this behaviour, the zonal part of the electrostatic potential of such a simulation is depicted in Fig. 6.2. Here, only the zonal modes that are driven by the self-interaction, see Eq. (5.6), are retained, the other zonal modes are set to zero.

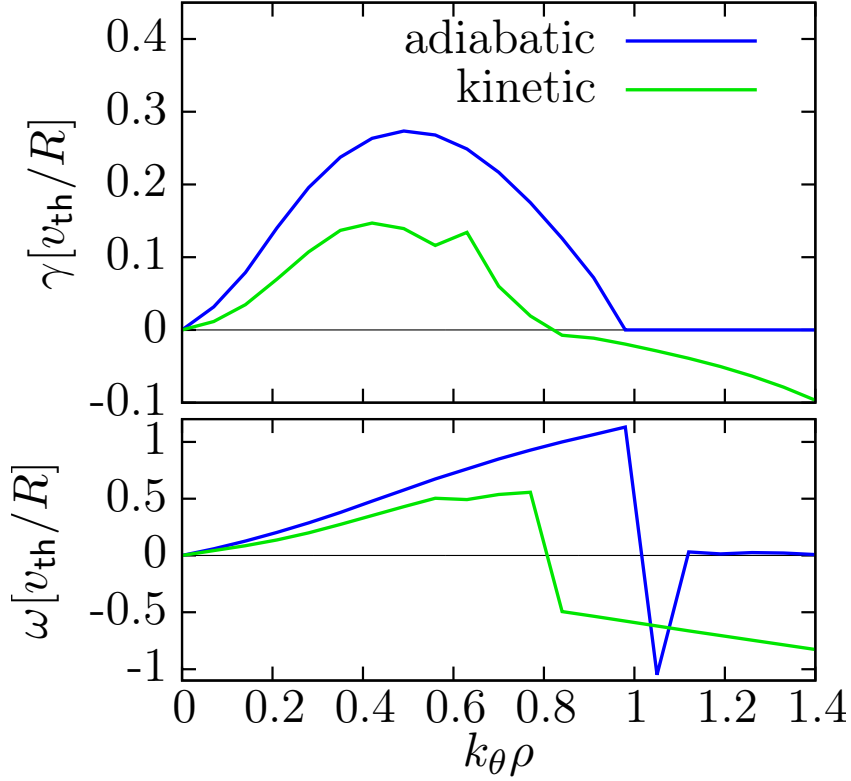


Figure 6.1.: Binormal spectra of the growth rate  $\gamma$  and the dominant frequency  $\omega$  for a linear simulation. In the kinetic case, the spectrum shows the influence of a trapped electron mode TEM for higher  $k_\theta$ .

In the adiabatic simulations, the following problem arises: The partially developed staircase, which is found above the finite heat flux threshold, is obstructed by fast fluctuations (see for example Ref. [11]) due to the unsuppressed turbulence. The typical staircase structure is only found if the  $E \times B$  shear is averaged over a long period. Therefore, keeping the current zonal flow fixed would bias the results. To circumvent this problem, the zonal flow is not kept fixed over time in that case. This can be justified as the linear period, in which the growth rates are measured, is relatively small ( $\approx 50R/v_{th}$ ) compared to the decay of the zonal flow, as shown in Chap. 4. A consequence of the turbulence quenching is that the fluctuations are not found any more. However, this is assumed to be negligible, as fast fluctuations exert no significant suppression [48]. If the damping of a fully developed staircase is investigated, this problem does appear, as no strong fluctuations are found in that case. In kinetic simulations strong small scale fluctuations are found, however they are not (strongly) fluctuating in time, which can be seen for example in Fig. 5.4 from Chap. 5. Consequently, it is assumed that keeping the zonal flow fixed does not bias the results.

## 6. Suppression of ITG due to structures in the zonal flow

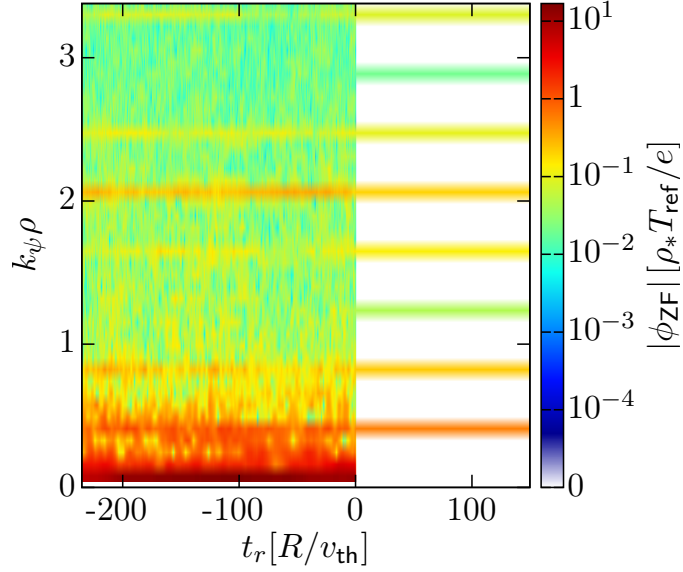


Figure 6.2.: Evolution of the radial spectrum of the zonal part ( $k_\theta = 0$ ) of the electrostatic potential  $\phi_{ZF}$ . At  $t_r = 0R/v_{th}$  ( $t = 534R/v_{th}$ ), only the zonal modes driven by self-interaction are kept. Note that the colour axis is logarithmic, however zero values are shown, they are indicated with white.

An example of linear growth after the quenching of the turbulence is given in Fig. 6.3. Here, the evolution of the poloidal spectrum of the electrostatic potential's absolute value averaged in the radial direction, which is taken as a measurement for mode intensity, is depicted. For visual convenience, only selected modes are shown, the quenching occurs at  $t_r = 0R/v_{th}$  ( $t = 534R/v_{th}$ ). The figure depicts the results of a kinetic simulation, where only the zonal modes driven by self-interaction are kept (see Fig. 6.2) after the turbulence is quenched. Consequently a suppressed regrowth is observed. To quantify the regrowth, the evolution of each mode is fitted with an exponential function of the form  $|\phi(t)| = A \exp[\gamma t]$  in the linear period, to obtain the growth rate  $\gamma$  of that mode. These fits are indicated with dashed lines in Fig. 6.3, the obtained growth rate spectrum is shown in Fig. 6.5. In most simulations, the period where a perfectly linear growth due to the ITG prevails is rather small. After that, nonlinear interactions lead to a grow of modes at high  $k_\theta$ . This is used as a reference for the end of the (purely) linear period in which the growth rate is measured.

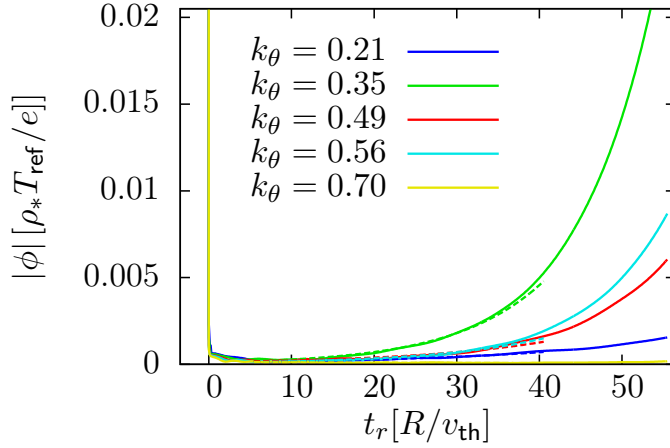


Figure 6.3.: Evolution of the poloidal spectrum of the electrostatic potential's absolute value averaged in the radial direction for selected binormal modes. The quenching occurs at  $t_r = 0R/v_{th}$  ( $t = 534R/v_{th}$ ). The exponential fit is shown with dashed lines of the same colour. In this kinetic simulation, only the zonal modes driven by self-interaction are kept (see Fig. 6.2).

## 6.2. Comparison of growth rate spectra

At first, a qualitative investigation of the damping of the zonal flow is carried out with the proposed method. Therefore adiabatic simulations are used, as in these simulations, no self-interaction is found [96] and a strong shear suppression is present [9–11, 51, 84]. In the adiabatic case, four growth rate spectra are measured with the proposed method and are shown in Fig. 6.4: A spectrum obtained from a simulation without the zonal flow (blue). A spectrum with the zonal flow, where a partially developed staircase is found (green) (here the zonal flow is not kept fixed over time). A spectrum where a fully developed staircase is present in the zonal flow (solid red). This zonal flow structure is obtained from a simulation below the finite heat flux threshold ( $R/L_T = 6.1$ ), where the zonal flow is kept fixed and  $R/L_T$  is changed to  $R/L_T = 6.9$  after the quenching. Furthermore, a spectrum also with a fully developed staircase, but where the zonal flow is not kept fixed (dashed red). The growth rate spectrum observed without the zonal flow shows only minor differences to the linear spectrum depicted in Fig. 6.1. A slight reduction of the overall growth rate and a small reduction of the unstable region are observed. This shows that the proposed measurement method can be used to obtain good results. The spectrum obtained here will be used as a reference value in Sec. 6.3 and later on. If this spectrum is compared to the spectra measured with a zonal flow, a strong damping is observed. The spectrum measured with a partial staircase shows a weaker damping than the spectrum obtained from a fully developed staircase. This is compliant to the findings described for example in Chap. 4 or Ref. [11]. When comparing these two spectra directly, care has to be taken as the zonal flow intensity depends on the strength of the turbulence (Waltz rule [49, 50]) and therefore

## 6. Suppression of ITG due to structures in the zonal flow

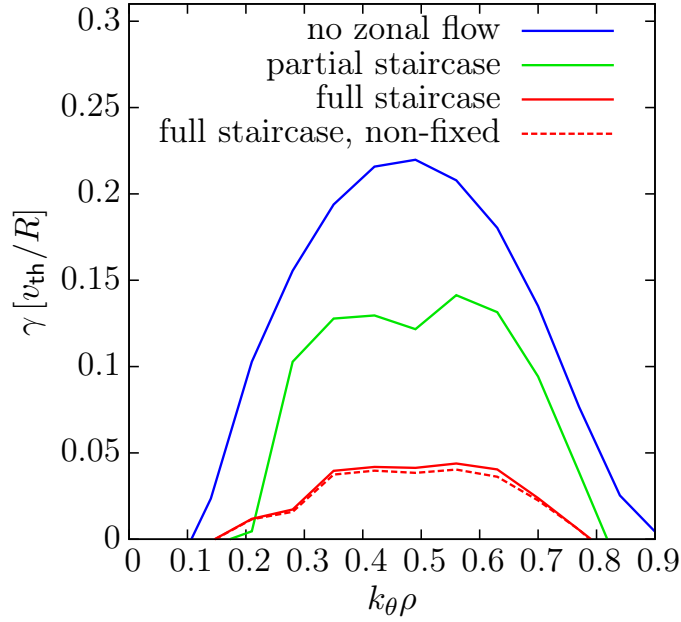


Figure 6.4.: Comparison of the measured binormal growth rate spectra after quenching. Results of an adiabatic simulations without zonal flow (blue), with a partially developed staircase (green) and a fully developed staircase (red) are shown.

on  $R/L_T$ , which leads to a small bias. The spectrum obtained from the simulation in which the zonal flow is not kept fixed shows only very slight variations compared to the spectrum measured with a fixed zonal flow. Thus it is assumed that not keeping the zonal flow fixed in the simulation with a partial staircase does not affect the results significantly.

Furthermore, in Fig. 6.5 three spectra that are obtained in the kinetic case are shown: A spectrum without the zonal flow (cyan). A spectrum where the complete zonal flow, with the dominant small scale structures driven by self-interaction, is present (yellow). A spectrum where only these small scale structures in the zonal flow are present, i.e. only the zonal modes driven by self-interaction are kept (magenta). A spectrum where these small scale structures, i.e. the modes driven by self-interaction, are removed from the zonal flow. Small differences, that are similar to the ones observed in the adiabatic case, between the growth rate spectrum obtained without the zonal flow and the linear growth rate spectrum are observed. The spectrum which is measure with the complete zonal flow, shows a considerable damping of the growth rates. The spectrum obtained with only the self-interaction-driven zonal modes, shows that these modes do contribute to the damping only marginally despite their large intensity. In the case where the modes driven by self-interaction are neglected, a strongly suppressed growth rate spectrum is measured, which is comparable to the one obtained with the complete zonal flow.

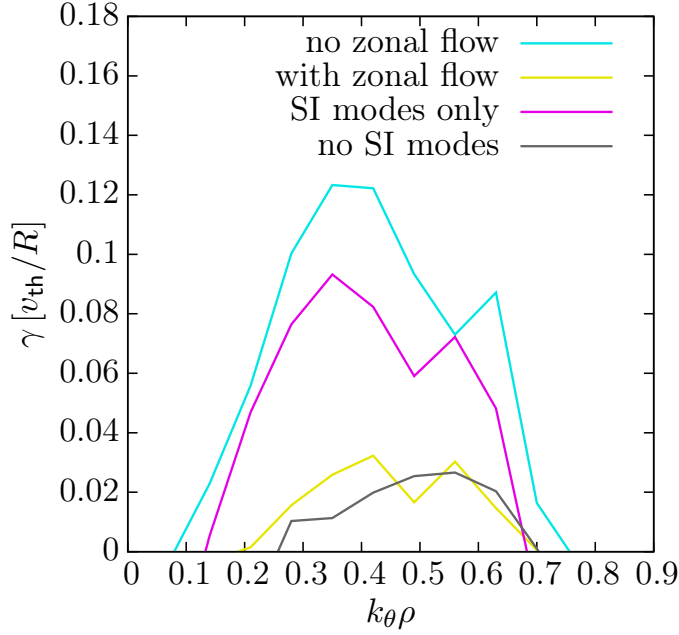


Figure 6.5.: Binormal growth rate spectra measured in kinetic simulations without the zonal flow (cyan), with the complete zonal flow (yellow), with only the modes driven by self-interaction (magenta) and with the zonal flow but without the modes driven by self-interaction (dark grey).

### 6.3. Relative Suppression Strength

The analysis described above shows the damping due to the zonal flow. However, the amplitude of the structures in the zonal flow is not taken into account, which hinders a quantitative statement about the efficiency of the damping due to a certain structure. To rectify this, the relative damping (efficiency)  $\alpha_{k_\theta}$  is defined to correspond to the Waltz rule, which states that turbulence suppression occurs when  $\omega_{E \times B} \approx \gamma_{ITG}$ . The relative damping efficiency is calculated as the difference (per mode) in the growth rate between an undamped reference spectrum  $\phi_{\text{ref}}$  and the spectrum itself  $\phi$  in relation to the total zonal flow intensity:

$$\alpha_{k_\theta} = \frac{\gamma_{\text{ref}, k_\theta} - \gamma_{k_\theta}}{1/2 \sum_{k_\psi} k_\psi^2 \phi_{\text{ZF}, k_\psi}}. \quad (6.1)$$

Therefore,  $\alpha_{k_\theta}$  should be approximately unity in simulations where the Waltz rule applies. For  $\phi_{\text{ref}}$ , the spectra measured for the cases without a zonal flow, depicted in Fig. 6.4 and Fig. 6.5 respectively for the adiabatic and kinetic cases, are chosen. This analysis allows to determine the damping efficiency of a certain zonal flow structure.

The relative damping  $\alpha_{k_\theta}$  is calculated for the simulations presented in Sec. 6.2, the results of the adiabatic cases are shown in Fig. 6.6. The relation between the relative

## 6. Suppression of ITG due to structures in the zonal flow

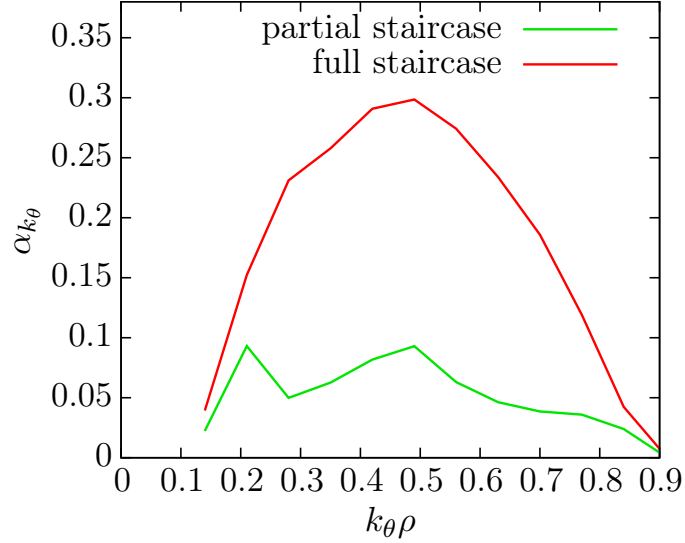


Figure 6.6.: Relative damping  $\alpha_{k_\theta}$  for adiabatic simulations where a partially developed (green) or a fully developed (red) staircase is present.

damping  $\alpha_{k_\theta}$  of a full staircase and the Waltz rule, suggests that  $\alpha_{k_\theta} \approx 1$ . However, this is not found and instead, surprisingly low values are observed. A possible explanation can be given as follows. Assuming that the suppression predominantly stems from the modes with low  $k_\theta$ , taking all modes, especially those at high  $k_\theta$ , into account, will reduce the intensity of  $\alpha_{k_\theta}$  (Eq. (6.1)). However, these modes will not lead to a significant suppression of the ITG, resulting in the observed discrepancy. Taking only the modes with  $k_\psi \rho \leq 1$  would lead to an increase of  $\alpha_{k_\theta}$  about a factor of  $\approx 2$ . Another reason for a part of the discrepancy could be the difference in  $R/L_T$  between the simulation used to obtain the zonal flow and the simulation where the growth rate is measured. From linear ITG simulations this would give a factor of  $\approx 0.2$ . The partial staircase has a lower relative damping than the fully developed staircase, which is in accordance to the observation that fully developed staircases lead to suppressed turbulence. At first glance, the difference appears relatively large, as partial staircases exert a strong suppression over most of the radial domain similar to fully developed staircases. But in the region of the softened flank, the suppression is reduced leading to the measurement of a strong ITG and consequently, a low relative damping.

The relative damping efficiency measured in the kinetic cases is shown in Fig. 6.7. Compared to the adiabatic cases, the relative damping is further reduced (in all cases). Again this can be explained as an overestimation of the contribution from the zonal modes at high  $k_\psi$ . These modes are stronger in the kinetic case due to the self-interaction, therefore the claim made above can explain the lower values of  $\alpha_{k_\theta}$  observed here. The complete zonal flow shows a relative damping which is comparable to the case with only the self-interaction-driven modes in the zonal flow. It is attributed to the fact in the

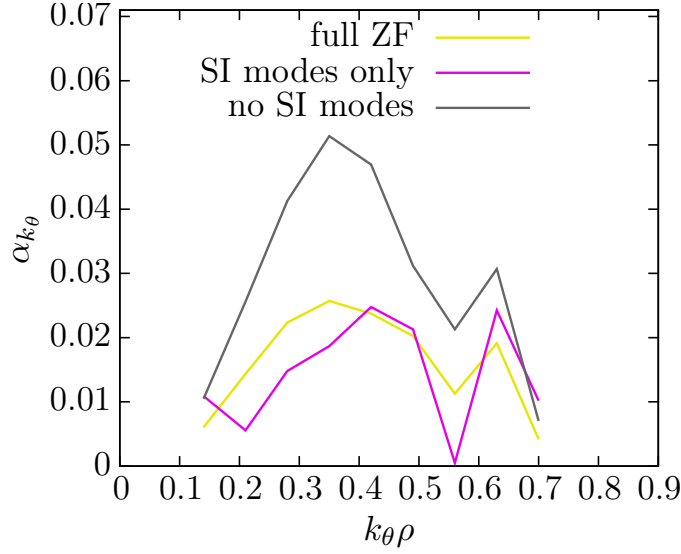


Figure 6.7.: In the kinetic case, results from simulations with the complete zonal flow (yellow), with only self-interaction driven modes (magenta) and without the self-interaction driven modes (dark grey) are shown.

latter case the total zonal flow intensity is considerably smaller than in the first case. Therefore, only a slight reduction of the observed growth rate results in a considerable damping efficiency. Removing the self-interaction driven modes from the zonal flow leads to an increase of the relative damping efficiency, as the growth rate spectra do not differ significantly, but a considerable part of the total zonal flow intensity is allocated in these modes, predominantly at higher radial wave vectors. This hints that the strongly driven modes might not play a significant role in the damping of the ITG and that the damping is mainly caused by modes with a low radial wave vector.

## 6.4. Relation to zonal flow spectrum

In this section, the relation of the damping to the wave vector will be examined more closely. Therefore, the relative damping  $\alpha_{k_{\theta}}$  is measured for simulations, where only parts of the zonal flow structure is kept. In the first analysis, kinetic simulations are used, where modes in the zonal flow spectrum up to a certain (maximal) radial wave vector  $k_{\psi}$  are retained. They are chosen to coincide with the modes driven by self-interaction. The resulting relative damping spectra are shown in Fig. 6.8. With only the large scale structures in the zonal flow where  $k_{\psi}\rho \leq 0.41$ , a high damping efficiency is measured. When the maximal radial wave vector is increased, the damping efficiency decreases. Here, a notable drop in efficiency is observed between the simulations with  $k_{\psi}\rho \leq 0.82$  and  $k_{\psi}\rho \leq 2.47$ . It has to be noted, that in the different cases, relatively comparable growth rate spectra are observed. The reduced intensity measured in the cases with

## 6. Suppression of ITG due to structures in the zonal flow

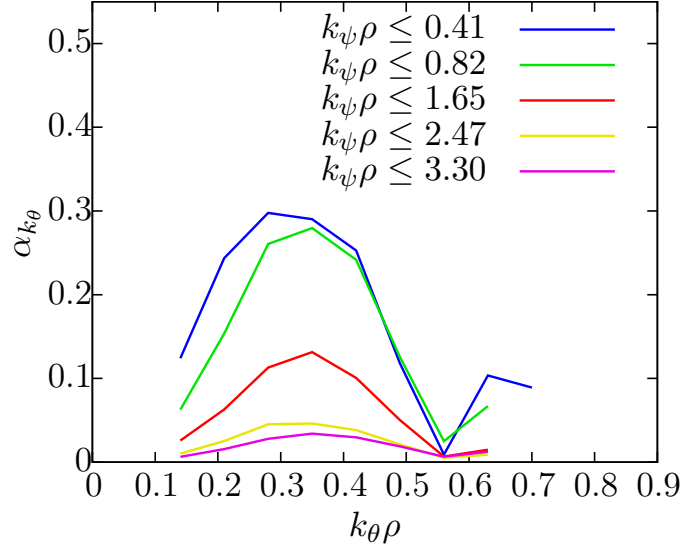


Figure 6.8.: Relative suppression  $\alpha_{k_{\theta}}$  for zonal flow spectra where modes up to a specified radial wave vector  $k_{\psi}$  are kept.

higher maximal  $k_{\psi}$  is then mainly caused by the increased intensity of the zonal flow itself (compare for example with Fig. 5.6). This proves the point made in the previous chapter. The modes at low  $k_{\psi}$  effect the observed suppression, whereas the modes at high  $k_{\psi}$  cause a negligible suppression of the ITG. Consequently, retaining these modes (in the calculation of  $\alpha_{k_{\theta}}$ ) leads to an underestimation of the relative damping  $\alpha_{k_{\theta}}$ .

Motivated by these findings, the damping efficiency of large scale structures for the adiabatic cases is examined. Therefore simulations with a zonal flow spectrum where only modes with  $k_{\psi}\rho \leq 1$  are kept, are carried out. The measured relative damping is shown in Fig. 6.9.  $\alpha_{k_{\theta}}$  of a simulation with a partial staircase (green) and a simulation with a full staircase (red) are depicted. The simulation with a full staircase again shows a higher relative damping than the simulation with a partial staircase, as discussed in Sec. 6.3. The overall value of  $\alpha_{k_{\theta}}$  increases, which further strengthens the conclusion that the damping of the growth rate is predominantly caused by zonal flow structures with a low radial wave vector.

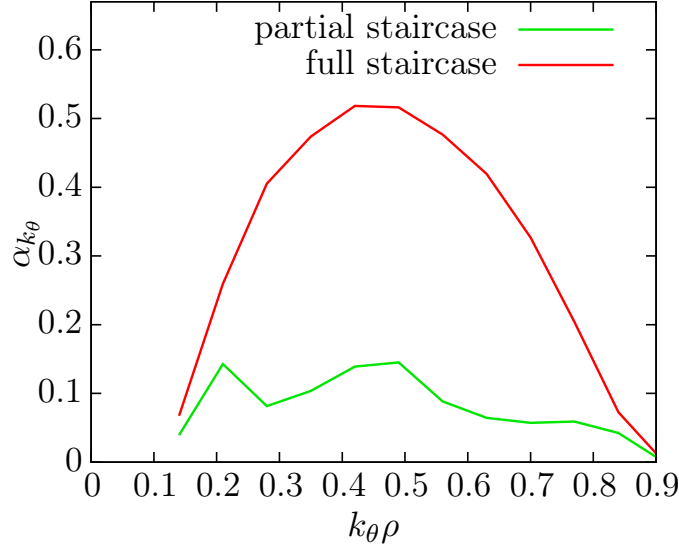


Figure 6.9.: Relative suppression  $\alpha_{k_{\theta}}$  of zonal flow spectra where only modes with  $k_{\psi}\rho \leq 1$  are kept. Results of adiabatic simulations with a partially developed (green) and a fully developed (red) staircase are depicted.

## 6.5. Conclusion

In this chapter, the damping of the ITG driven turbulent modes due to structures in the zonal flow is investigated. Therefore adiabatic and kinetic simulations with the gyrokinetic code GKW are carried out. To measure the growth rate of the modes, the turbulent modes are quenched, i.e. set to a small value. After that, a period where these modes exhibit a linear behaviour and an exponential growth is visible, which allows to measure their growth rates. The established zonal flow from before the quenching is kept fixed or modified, therefore a damped growth of the turbulent modes is observed. A qualitative analysis of the growth rate spectra measured without a zonal flow shows only minor differences compared to the spectra measured in linear simulations. In the adiabatic case, a strong damping of due to fully developed staircase and a less pronounced damping due to a partial staircase is observed. In the kinetic case, also a strongly damped growth rate spectrum is measured if the complete zonal flow is kept. If only the modes that are driven by the self-interaction are kept, albeit their high intensity, only a moderately damped spectrum is observed. In turn, if these modes are removed, a damping comparable to the full zonal flow is measured. To quantify the analyses, the relative damping  $\alpha_{k_{\theta}}$ , which is taken as a measure of the damping efficiency of a zonal flow structure, is introduced. It is defined as the per mode growth rate difference to the corresponding undamped spectrum in relation to the total zonal flow intensity. In general, surprisingly low values of  $\alpha_{k_{\theta}}$  are measured, which is linked to the damping being effected predominantly by the modes with low radial wave vectors. Consequently, taking all modes into account leads to an underestimation of  $\alpha_{k_{\theta}}$ . For adiabatic simulations it is found that the damping efficiency

## 6. *Suppression of ITG due to structures in the zonal flow*

of a partially is smaller than the efficiency of a fully developed staircase, which is expected. In all the kinetic cases, even lower values of  $\alpha_{k_\theta}$  are observed. As the main contribution of the modes driven by self-interaction lies at higher radial wave vectors, it is concluded that this result strengthens the claim made above. The modes driven by self-interaction have a comparable damping efficiency to the complete zonal flow, whereas removing these modes leads to an increase of the damping efficiency. Furthermore, the relation of the relative damping to the radial zonal flow spectrum is examined, by keeping only the zonal flow spectrum below a certain maximum radial wave vector  $k_\psi$ . A high damping efficiency is observed for large scale structures, increasing the maximum wave vector leads to a significant decrease of efficiency. This behaviour suggest again that mainly large scale structures contribute to the turbulence suppression. To complement this investigation, a comparison of  $\alpha_{k_\theta}$  for zonal flow structures with  $k_\psi \rho \leq 1$  in adiabatic simulations is carried out. The relative damping increases, which corroborates the conclusion that the damping is predominantly effected by zonal flow structures with a low radial wave vector and therefore the modes driven by self-interaction do not contribute significantly.

## 7. Conclusion and Outlook

In this thesis, the structure formation in the  $E \times B$  shear in a Tokamak plasma was investigated.

The influence of ion-ion collisions on the ion temperature gradient driven heat flux and its relation to the formation of staircases in the  $E \times B$  shear were examined in the adiabatic limit. In a linear analysis the influence of collisions on the decay of the zonal potential has been examined and was compared with the analytical model of Ref. [35]. The obtained decay rates agree well with the analytic prediction mainly for low collision frequencies. The influence of the safety factor and the inverse aspect ratio were reproduced. An extensive scan in the temperature gradient length and the collision frequency parameter space was carried out to investigate the behaviour of the finite heat flux threshold. In these simulations two distinct states are visible: a state where turbulence is suppressed and the heat flux almost vanishes, and a state with a finite heat flux. At some points in the parameter space, a transposition of both states for a considerable time period was observed. Three different temperature gradient lengths that characterize the near threshold dynamics were identified: the gradient length of linear stability  $R/L_{T,\text{lin}}$ , the Dimits gradient length  $R/L_{T,\text{Dim}}$  and the finite heat flux threshold  $R/L_{T,\text{fh}}$ , where  $R/L_{T,\text{lin}} < R/L_{T,\text{Dim}} < R/L_{T,\text{fh}}$  applies. In the region where  $R/L_{T,\text{Dim}} < R/L_T < R/L_{T,\text{fh}}$ , the collisions exert the most influence on the finite heat flux threshold. Slight increases of the collision frequency lead to a noticeable decrease of the finite heat flux threshold. Outside of this region a very strong increase of the collision frequency was needed to produce a significantly larger heat flux. A comparison of the time spent in the vanishing heat flux state and the collisional zonal flow decay time, revealed that in the linear analysis the potential would have decayed substantially long time before the end of the state has been reached. For sufficiently small collision frequencies, the zonal flow can therefore be driven against the collisional dissipation even when the heat flux is vanishingly small. Despite the reduction of the finite heat flux threshold with increasing collision frequency, it remained considerably larger compared to the interpolated Dimits threshold for collision frequencies relevant to current experiments. For a fixed collision frequency, the shear rate of the radial mode with the longest wave length increased almost linearly with  $R/L_T$  up to the value of the finite heat flux threshold, for larger values a decay was observed. This behaviour was not seen for very high collision frequencies. The latter decay suggests a saturation mechanism of the zonal flow directly related to the turbulence intensity. If the collision frequency was increased for a fixed  $R/L_T$  close to the finite heat flux threshold, the shear intensity stayed relatively constant until the finite heat flux threshold was reached, then decayed to a finite value for

## 7. Conclusion and Outlook

high collision frequencies. A small region in temperature gradient lengths, above the finite heat flux threshold, was found, where a high shear intensity is paired with a finite heat flux, indicating that the contemplation of only the shear intensity is not sufficient for a description of the finite heat flux threshold. The radial profile of the  $E \times B$  shearing rate showed staircase formation in relation to the finite heat flux behaviour. Fully developed staircases were observed below the finite heat flux threshold and lead to a suppression of turbulence with a vanishing heat flux. Partially developed staircases (which have the shapes of sawtooth) allow the appearance of avalanches and lead to a finite heat flux. The latter were observed above the finite heat flux threshold, both in the direction of  $R/L_T$  and collision frequency. It was also observed that, although the transition from fully developed to partially developed staircase required only small changes in the collision frequency at the corresponding  $R/L_T$ , very high collision frequencies were required to suppress the formation of partial staircases themselves. The examination of staircases provided a satisfying explanation for the behaviour of the finite heat flux threshold.

Furthermore, the formation of structures in the zonal flow was investigated in the kinetic electron picture. It was shown that staircase structures do develop in gyro-kinetic simulations with kinetic electrons, however not under all circumstances. In many cases strong small scale structures in the  $E \times B$  shearing rate were observed. In these cases, no staircase structure could be identified and consequently, the heat flux went smoothly to zero when the temperature gradient length was reduced. Heat flux avalanches were observed, however no radial localization could be made out. The small scale  $E \times B$  shearing rate structures are interpreted to disrupt the formation of the larger scale staircase structures. As no convincing explanation for the staircase formation is available, this interpretation is empirical. The small scale structures observed in the  $E \times B$  shearing rate are interpreted as being driven by the self-interaction of turbulent modes that were generated over the periodic boundary conditions of the double periodic torus. While the ITG mode with adiabatic electrons is localized along the magnetic field, and shows no appreciable self-interaction, the mechanism is present in the case of kinetic electrons due to the extended mode structure. This explains the differences to the previously conducted adiabatic analysis. The self-interaction was shown to decrease with the number of toroidal modes kept in the simulation, and for a full flux surface simulation scaled proportional to  $\rho_*$ . It is to be expected that the effect is small in a reactor plasma, but at  $\rho_* = 5 \cdot 10^{-3}$  it was still dominantly present and it is therefore likely that it is of importance to present day experiments. Also the magnetic shear was observed to affect the results through its impact on the boundary conditions, which allowed to generate conditions under which staircases were observed to form in kinetic simulations. An investigation of the self-interaction mechanism in global simulations also allowed to observe the strong small scale structures. This ruled out, that the self-interaction and the small scale structures were an artefact of the local approximation. To complement the investigation of Chap. 4, the influence of collisions on the self-interaction mechanism was examined. The small scale structures were found to be affected only slightly by collisions compared to the staircase structures observed in the adiabatic limit. The entirety of the

carried out investigations lead to the conclusion that the self-interaction is a relatively robust mechanism.

Furthermore, the damping of the ITG driven turbulent modes due to structures in the zonal flow shear was examined in adiabatic and kinetic simulations. To obtain quantitative data, the growth rates were fitted exponentially in the linear regime after a quenching of the turbulent modes. The established zonal flow from before the quenching was completely kept or partly modified, therefore a damped growth of the turbulent modes was measured. A qualitative analysis of the growth rate spectra observed without a zonal flow showed only minor differences to the spectra measured in linear simulations. In the adiabatic case, a strong damping due to a fully developed staircase and a less pronounced damping due to a partial staircase was observed. In the kinetic case, also a strongly damped growth rate spectrum was measured if the complete zonal flow was kept. If only the modes that are driven by the self-interaction were kept in the zonal flow, albeit their high intensity, only a moderately damped spectrum was observed. In turn, if these modes were removed, a damping comparable to the full zonal flow was measured. To quantify the analyses, the relative damping  $\alpha_{k_\theta}$ , which is taken as a measure of the damping efficiency of a zonal flow structure, was introduced. It is defined as the per mode growth rate difference to the corresponding undamped spectrum in relation to the total zonal flow intensity. In general, low values of  $\alpha_{k_\theta}$  were observed. This could be explained if the damping is predominantly caused by modes with low radial wave vectors and consequently, taking the complete zonal underestimates the efficiency. For adiabatic simulations it was found that the damping efficiency of a fully developed staircase was larger than the efficiency of a partial staircase. Kinetic simulations showed that the modes driven by self-interaction have a damping efficiency comparable to the complete zonal flow, removing these modes lead to an increase of the damping efficiency. As the main contribution of these modes lies at higher radial wave vectors, these results hinted that the damping is caused by modes with low radial wave vectors. Furthermore, the relation of the relative damping to the radial zonal flow spectrum was examined, by keeping only the zonal flow spectrum below a varying maximum radial wave vector  $k_\psi$ . A high damping efficiency was observed for large scale structures, which suggest that mainly these large scale structures contribute to the turbulence suppression. To complement this investigation, a comparison of  $\alpha_{k_\theta}$  for zonal flow structures with  $k_\psi \rho \leq 1$  was carried out for adiabatic simulations. Its results corroborated the conclusion that the damping is predominantly effected by zonal flow structures with a low radial wave vector and therefore the modes driven by self-interaction do not contribute significantly to the damping of the ITG.

The analyses showed that the staircase structure can be considered relatively robust. It has been widely observed in varying conditions, not only in the scope of this thesis but also for example in Refs. [8–11, 36, 51] and its suppression of turbulent transport has also been reported outside of this thesis in Refs. [10, 11]. Collisions do not affect the formation significantly at moderate collision frequencies. Instead, a wide range in

## *7. Conclusion and Outlook*

the collisional regime with high relevance to the core region of current or future reactor experiments is suitable for staircase formation. The strong small scale structures driven by self-interaction, which are robustly found in kinetic simulations are observed to hinder the formation of fully developed staircases. At the same time they do not provide an efficient damping of turbulence themselves. However there are regimes where staircase formation dominates and states with a suppressed heat flux are present. As the self-interaction is found to scale with the Larmor radius, its influence on future reactor experiments might be overestimated by current day numerical investigations and staircase formation and an augmented turbulence suppression might prevail. This shows that the formation of structures in Tokamak fusion reactors is an important and rewarding topic.

## A. Running GKW with LAW

A brief summary over the “library Arne Weikl” (LAW) is given in this chapter. LAW is a collection of BASH-scripts<sup>1</sup>, facilitated to minimize the “manual” effort required to run GKW on a (or many) super computer(s) (external machine - EM), *i.e. if one feels too important to copy files by hand*. It is intended not only to save valuable time, but also to encourage a sufficient amount of accompanying tests and convergence studies for an examined problem. In theory, running a simulation should only require to: type the name of the LAW-script, specify an *input.dat*-file, make up a directory-name and hit -ENTER- multiple times. Its work flow is based on a central run-directory (CRD), which contains all simulations and is usually located on the local hard-disk. For basic operation, four scripts, being at the “front-end”, are needed:

- *law\_compile\_external*: copy the relevant part of a GKW-directory to an EM and compile the code there
- *law\_run\_external*: start a simulation on an EM and once finished, copy the results back to CRD
- *law\_scan\_external*: do a multitude of simulations on an EM
- *restart\_external*: restart a simulation

More “front-end” scripts do exist, for example a backup for the CRD, conversion to or from a *gkwrn*-style directory structure, etc. . A detailed description can be found at the beginning of each script. Currently the following EMS are (were) supported: Bayreuth cluster III, Bayreuth cluster II, (Helios), (Marconi).

A working version can be found at `/home/btpp/btp00000/arne/LAW-scripts`. To install, the parameters found in `lib_AW.txt` have to be adapted, the scripts in the *script* directory have to be given execution-rights and paths to this directory and also the *internal\_script* directory have to be exported. Furthermore, the installation of a ssh-key (to prevent a password prompt) is recommended. To use it, a work flow with a CRD and the CRD itself are (obviously) necessary. Also, for the external compilation, everything required for the compilation (modules, etc.) has to be loaded even for a “non-interactive” ssh-prompt. More detailed information on the installation and the use can be found at the beginning of the *lib\_AW.txt*-file. It uses selective ssh-multiplexing to circumvent several restrictions from the EMS. It will also do basic statistics of the simulations which were run with the library. Furthermore it will deposit extensive information about the versions of GKW which was used to run each simulation to ease version management and prevent errors.

---

<sup>1</sup>Done in BASH due to the (probably) same reasons for every BASH-script.



## B. GTS-theory

Here, an equation for the evolution of the spikes in the zonal flow is derived, with the electrostatic potential being used as a variable. The time averaged momentum balance equation of the Navier-Stokes equations is used as a starting point. Using the Reynolds decomposition and neglecting spatial variations of the plasma density, the magnetic field and external forces leads to the only contribution to the slow varying zonal flow coming from the time averaged Reynolds stress in the momentum balance equation [53]:

$$\frac{\partial \mathbf{v}_{\text{ZF}}}{\partial t} + \nabla \cdot \langle \tilde{\mathbf{v}} \tilde{\mathbf{v}} \rangle_t = 0. \quad (\text{B.1})$$

As the evolution of the zonal flow is considered, the zonal potential  $\phi_{\text{ZF}}$  is introduced as

$$v_{\text{ZF}} = \frac{1}{B} \frac{\partial \phi_{\text{ZF}}}{\partial \psi}. \quad (\text{B.2})$$

Taking the flux-surface average, indicated with curly brackets, allows to take only the net transport of momentum by the Reynolds stress. Assuming that the variation of the Reynolds stress in the directions other than the radial are small and can be neglected, the momentum balance is transformed to

$$\left\{ \frac{\partial}{\partial \psi} \frac{\partial \phi_{\text{ZF}}}{\partial t} \right\} = -B \left\{ \frac{\partial}{\partial \psi} \langle \tilde{v}_\psi \tilde{v}_\zeta \rangle_t \right\}. \quad (\text{B.3})$$

This is equal to

$$\left\{ \frac{\partial \phi_{\text{ZF}}}{\partial t} \right\} = -B \{ \langle \tilde{v}_\psi \tilde{v}_\zeta \rangle_t \}. \quad (\text{B.4})$$

The relation of the fluctuating flows to the electrostatic potential is given through the  $E \times B$  flow in the lowest order of Tokamak geometry:

$$\tilde{v}_\psi = -\frac{1}{\psi B} \frac{\partial \tilde{\phi}}{\partial \zeta} \quad \tilde{v}_\zeta = \frac{1}{B} \frac{\partial \tilde{\phi}}{\partial \psi}. \quad (\text{B.5})$$

Normalizing the potential with  $\phi = \frac{T\rho_*}{e} \phi_N$  and assuming a slim flux tube allows to write (where the subscript  $N$  is omitted in the following)

$$\left\{ \frac{\partial \phi_{\text{ZF}}}{\partial t} \right\} = \frac{T\rho_*}{eB\psi} \left\{ \left\langle \frac{\partial \tilde{\phi}}{\partial \zeta} \frac{\partial \tilde{\phi}}{\partial \psi} \right\rangle_t \right\}, \quad (\text{B.6})$$

## B. GTS-theory

to obtain an evolution equation for the zonal potential. To estimate the drive of each mode, a spectral representation, similar to the one employed by GKW as detailed in Chap. 3, is used to describe the potential:

$$\begin{aligned} \phi(\psi, \zeta) = & \sum_{k_\zeta > 0, k_\psi} \hat{\phi}(k_\psi, k_\zeta) \exp[ik_\zeta \zeta + ik_\psi \psi] + \sum_{k_\zeta > 0, k_\psi} \hat{\phi}^\dagger(k_\psi, k_\zeta) \exp[-ik_\zeta \zeta - ik_\psi \psi] \\ & + \sum_{k_\psi} \hat{\phi}(k_\psi, 0) \exp[ik_\psi \psi]. \end{aligned} \quad (\text{B.7})$$

Note that the binormal wave vector is restricted to the positive domain (and the sum is split), whereas the radial wave vector is not. The dependence along the magnetic field is not taken into account as it can be neglected for this analysis. Inserting this representation into the evolution equation with the zonal flow being restricted to  $k_\zeta = 0$  and introducing distinguished wave vectors leads to

$$\begin{aligned} & \left\{ \frac{\partial}{\partial t} \sum_{k_\psi^{\text{ZF}}} \hat{\phi}(k_\psi^{\text{ZF}}, 0) \exp[ik_\psi^{\text{ZF}} \psi] \right\} = \\ & \left\{ \left\langle \left( \sum_{k_\zeta^1 > 0, k_\psi^1} ik_\zeta^1 \hat{\phi}(k_\psi^1, k_\zeta^1) \exp[ik_\zeta^1 \zeta + ik_\psi^1 \psi] - \sum_{k_\zeta^1 > 0, k_\psi^1} ik_\zeta^1 \hat{\phi}^\dagger(k_\psi^1, k_\zeta^1) \exp[-ik_\zeta^1 \zeta - ik_\psi^1 \psi] \right) \right. \right. \\ & \left. \left. \left( \sum_{k_\zeta^2 > 0, k_\psi^2} ik_\zeta^2 \hat{\phi}(k_\psi^2, k_\zeta^2) \exp[ik_\zeta^2 \zeta + ik_\psi^2 \psi] + \sum_{k_\zeta^2 > 0, k_\psi^2} ik_\zeta^2 \hat{\phi}^\dagger(k_\psi^2, k_\zeta^2) \exp[-ik_\zeta^2 \zeta - ik_\psi^2 \psi] \right) \right\rangle_t \right\}, \end{aligned} \quad (\text{B.8})$$

where the wave vectors and the time derivative have been normalized according to GKW's standard [78]. Here  $\mathbf{k}^1$  and  $\mathbf{k}^2$  denote the wave vectors of the turbulent modes and  $\mathbf{k}^{\text{ZF}}$  the wave vector of the zonal mode. To progress, the following has to be considered. The flux surface average provides an integral in  $\psi$ ,  $\zeta$  and  $s$ . Following from a basic identity of the delta-distribution [108], only modes where

$$\mathbf{k}_1 + \mathbf{k}_2 - \mathbf{k}_{\text{ZF}} = 0 \quad (\text{B.9})$$

holds, need to be considered, as observed in three wave interaction theory. Various mode interactions are possible, however only interactions where both binormal wave vectors are antisymmetric can drive the zonal flow. Furthermore, modes which are connected through the boundary conditions along a field line with a wave vector shift of  $\Delta k_\psi$  (see Eq. 5.6) are expected to generate a strong drive due to their strong connection. This leads to the selection of mode pairs with

$$k_\psi^1 = -(k_\psi^2 - \Delta k_\psi) \quad (\text{B.10})$$

and vice versa. Using this selection in Eq. B.9 means that all modes at the same binormal wave vector will drive the zonal mode at the radial wave vector distinguished by the wave vector shift  $\Delta k_\psi$ . This will lead to an exceptionally strong drive. The described behaviour is visualized in Fig. B.1, where the interaction is depicted in the spectral plane for two modes with different  $k_\psi$  (black and blue). It can be seen that for both  $k_\psi$  the

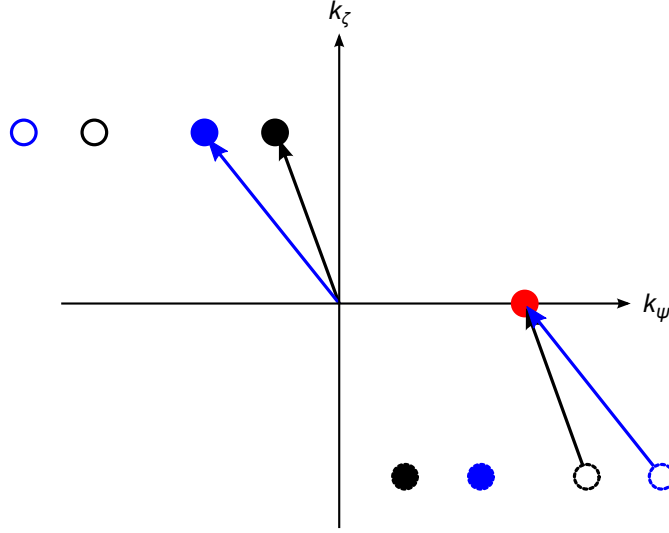


Figure B.1.: Sketch of the wave vector selection rules of the self-interaction for two modes with different  $k_\psi$ .

same zonal mode (red) is driven. Using this information allows to estimate the drive from modes at a specified  $k_\zeta$  of a zonal mode at the corresponding  $\Delta k_\psi$ :

$$\frac{\partial}{\partial t} \hat{\phi}_{\text{ZF}}(\Delta k_\psi) = \sum_{k_\psi > 0} k_\psi k_\zeta \left( \hat{\phi}(-k_\psi, k_\zeta) \hat{\phi}^\dagger(k_\psi + \Delta k_\psi, -k_\zeta) + \hat{\phi}^\dagger(-k_\psi, -k_\zeta) \hat{\phi}(k_\psi + \Delta k_\psi, k_\zeta) \right). \quad (\text{B.11})$$

Note that this equation describes the growth of zonal modes at positive  $\Delta k_\psi$ , a corresponding expression is found for negative  $\Delta k_\psi$ .



## Bibliography

- [1] NRL *plasma formulary* (Naval Research Laboratory, Washington DC, 2018).
- [2] G. Miley, H. Towner, and N. Ivich, “Fusion cross sections and reactivities”, *University of Illinois, C-U Campus Nuclear Engineering Program* (1974).
- [3] Max-Planck-Gesellschaft zur Förderung der Wissenschaften e. V., ASDEX *Upgrade*, [www.ipp.mpg.de/ippcms/de/pr/forschung/asdex/](http://www.ipp.mpg.de/ippcms/de/pr/forschung/asdex/), Oct. 1, 2018.
- [4] ITER *technical basis* (IAEA, Vienna, 2002).
- [5] K. Ikeda, “ITER on the road to fusion energy”, *Nuclear Fusion* **50**, 014002 (2009).
- [6] J. Wesson, ed., *Tokamaks*, 3. (Oxford University Press, Oxford, New York, 1987).
- [7] G. Dif-Pradalier, V. Grandgirard, Y. Sarazin, X. Garbet, and P. Ghendrih, “Interplay between gyrokinetic turbulence, flows, and collisions: perspectives on transport and poloidal rotation”, *Phys. Rev. Lett.* **103**, 065002 (2009).
- [8] G. Dif-Pradalier, P. H. Diamond, V. Grandgirard, Y. Sarazin, J. Abiteboul, X. Garbet, P. Ghendrih, A. Strugarek, S. Ku, and C. S. Chang, “On the validity of the local diffusive paradigm in turbulent plasma transport”, *Phys. Rev. E* **82**, 025401 (2010).
- [9] G. Dif-Pradalier, G. Hornung, P. Ghendrih, Y. Sarazin, F. Clairet, L. Vermare, P. H. Diamond, J. Abiteboul, T. Cartier-Michaud, C. Ehrlacher, D. Estève, et al., “Finding the elusive  $\mathbf{E} \times \mathbf{B}$  staircase in magnetized plasmas”, *Phys. Rev. Lett.* **114**, 085004 (2015).
- [10] F. Rath, A. G. Peeters, R. Buchholz, S. R. Grosshauser, P. Migliano, A. Weikl, and D. Strintzi, “Comparison of gradient and flux driven gyro-kinetic turbulent transport”, *Physics of Plasmas* **23**, 052309 (2016).
- [11] A. G. Peeters, F. Rath, R. Buchholz, Y. Camenen, J. Candy, F. J. Casson, S. R. Grosshauser, W. A. Hornsby, D. Strintzi, and A. Weikl, “Gradient-driven flux-tube simulations of ion temperature gradient turbulence close to the non-linear threshold”, *Physics of Plasmas* **23**, 082517 (2016).
- [12] W. M. Stacey, ed., *Fusion plasma physics*, 2. (Wiley-VCH, Weinheim, 2012).
- [13] R. Fitzpatrick, ed., *Plasma physics: an introduction*, 1. (CRC-Press, Boca Raton, Florida, 2014).
- [14] L. Shunjie, H Jiang, Z. Ren, and C Xu, “Optimal tracking for a divergent-type parabolic PDE system in current profile control”, *Abstract and Applied Analysis* **2014**, 1–8 (2014).

## Bibliography

- [15] V. D. Shafranov, “On magnetohydrodynamical equilibrium configurations”, *Soviet Physics JETP* **6**, 545–554 (1958).
- [16] ITER Organization, ITER, [www.iter.org](http://www.iter.org), Oct. 1, 2018.
- [17] G. A. Ct., DIII-D, <https://fusion.gat.com/global/diii-d/home>, Oct. 1, 2018.
- [18] EUROfusion, JET: EUROfusion’s flagship device, <https://www.euro-fusion.org/devices/jet/>, Oct. 1, 2018.
- [19] D. Meade, “50 years of fusion research”, *Nuclear Fusion* **50**, 014004 (2009).
- [20] S. C. Cowley, R. M. Kulsrud, and R. Sudan, “Considerations of ion-temperature-gradient driven turbulence”, *Physics of Fluids B: Plasma Physics* **3**, 2767–2782 (1991).
- [21] A. M. Dimits, G. Bateman, M. A. Beer, B. I. Cohen, W. Dorland, G. W. Hammett, C. Kim, J. E. Kinsey, M. Kotschenreuther, A. H. Kritz, L. L. Lao, et al., “Comparisons and physics basis of tokamak transport models and turbulence simulations”, *Physics of Plasmas* **7**, 969–983 (2000).
- [22] C. Greenfield, J. DeBoo, T. Osborne, F. Perkins, M. Rosenbluth, and D. Boucher, “Enhanced fusion performance due to plasma shape modification of simulated ITER discharges in dIII-d”, *Nuclear Fusion* **37**, 1215 (1997).
- [23] P. S. Marcus, “Jupiter’s great red spot and other vortices”, *Annual Review of Astronomy and Astrophysics* **31**, 523–569 (1993).
- [24] U. Stroth, ed., *Plasmaphysik*, 1. (Vieweg+Teubner Verlag, Wiesbaden, 2011).
- [25] L. Chen, Z. Lin, and R. White, “Excitation of zonal flow by drift waves in toroidal plasmas”, *Physics of Plasmas* **7**, 3129–3132 (2000).
- [26] P. N. Guzdar, R. G. Kleva, and L. Chen, “Shear flow generation by drift waves revisited”, *Physics of Plasmas* **8**, 459–462 (2001).
- [27] C. N. Lashmore-Davies, D. R. McCarthy, and A. Thyagaraja, “The nonlinear dynamics of the modulational instability of drift waves and the associated zonal flows”, *Physics of Plasmas* **8**, 5121–5133 (2001).
- [28] G. Manfredi, C. M. Roach, and R. O. Dendy, “Zonal flow and streamer generation in drift turbulence”, *Plasma Physics and Controlled Fusion* **43**, 825–837 (2001).
- [29] D. Strintzi and F. Jenko, “On the relation between secondary and modulational instabilities”, *Physics of Plasmas* **14**, 042305 (2007).
- [30] X. Garbet, Y. Idomura, L. Villard, and T. Watanabe, “Gyrokinetic simulations of turbulent transport”, *Nuclear Fusion* **50**, 043002 (2010).
- [31] M. N. Rosenbluth and F. L. Hinton, “Poloidal flow driven by ion-temperature-gradient turbulence in tokamaks”, *Phys. Rev. Lett.* **80**, 724–727 (1998).
- [32] F. L. Hinton and M. N. Rosenbluth, “Dynamics of axisymmetric  $\mathbf{E} \times \mathbf{B}$  and poloidal flows in tokamaks”, *Plasma Physics and Controlled Fusion* **41**, A653 (1999).

- [33] N. Winsor, J. L. Johnson, and J. M. Dawson, “Geodesic acoustic waves in hydro-magnetic systems”, *The Physics of Fluids* **11**, 2448–2450 (1968).
- [34] Z. Lin, T. S. Hahm, W. W. Lee, W. M. Tang, and P. H. Diamond, “Effects of collisional zonal flow damping on turbulent transport”, *Physical Review Letters* **83**, 3645–3648 (1999).
- [35] Y. Xiao, P. J. Catto, and K. Molvig, “Collisional damping for ion temperature gradient mode driven zonal flow”, *Physics of Plasmas* **14**, 032302 (2007).
- [36] F. Seiferling, A. G. Peeters, R. Buchholz, S. R. Grosshauser, F. Rath, and A. Weigl, “Damping of zonal modes through turbulent momentum transport”, *Physics of Plasmas* **25**, 022505 (2018).
- [37] T. S. Hahm and K. H. Burrell, “Flow shear induced fluctuation suppression in finite aspect ratio shaped tokamak plasma”, *Physics of Plasmas* **2**, 1648–1651 (1995).
- [38] A. M. Dimits, T. J. Williams, J. A. Byers, and B. I. Cohen, “Scalings of ion-temperature-gradient-driven anomalous transport in tokamaks”, *Phys. Rev. Lett.* **77**, 71–74 (1996).
- [39] Z. Lin, T. S. Hahm, W. W. Lee, W. M. Tang, and R. B. White, “Turbulent transport reduction by zonal flows: massively parallel simulations”, *Science* **281**, 1835–1837 (1998).
- [40] P. W. Terry, “Suppression of turbulence and transport by sheared flow”, *Rev. Mod. Phys.* **72**, 109–165 (2000).
- [41] J. Candy and R. Waltz, “An eulerian gyrokinetic-maxwell solver”, *Journal of Computational Physics* **186**, 545–581 (2003).
- [42] K. Itoh, S.-I. Itoh, P. H. Diamond, T. S. Hahm, A. Fujisawa, G. R. Tynan, M. Yagi, and Y. Nagashima, “Physics of zonal flows”, *Physics of Plasmas* **13**, 055502 (2006).
- [43] G. M. Staebler, R. E. Waltz, J. Candy, and J. E. Kinsey, “New paradigm for suppression of gyrokinetic turbulence by velocity shear”, *Phys. Rev. Lett.* **110**, 055003 (2013).
- [44] H. Biglari, P. H. Diamond, and P. W. Terry, “Influence of sheared poloidal rotation on edge turbulence”, *Physics of Fluids B: Plasma Physics* **2**, 1–4 (1990).
- [45] K. C. Shaing, E. C. Crume, and W. A. Houlberg, “Bifurcation of poloidal rotation and suppression of turbulent fluctuations: a model for the L-H transition in tokamaks”, *Physics of Fluids B: Plasma Physics* **2**, 1492–1498 (1990).
- [46] F. Wagner, G. Becker, K. Behringer, D. Campbell, A. Eberhagen, W. Engelhardt, G. Fussmann, O. Gehre, J. Gernhardt, G. v. Gierke, G. Haas, et al., “Regime of improved confinement and high beta in neutral-beam-heated divertor discharges of the asdex tokamak”, *Phys. Rev. Lett.* **49**, 1408–1412 (1982).

## Bibliography

- [47] I. Shesterikov, Y. Xu, C. Hidalgo, M. Berte, P. Dumortier, M. V. Schoor, M. Vergote, and G. V. Oost, “Direct evidence of eddy breaking and tilting by edge sheared flows observed in the TEXTOR tokamak”, *Nuclear Fusion* **52**, 042004 (2012).
- [48] T. S. Hahm, M. A. Beer, Z. Lin, G. W. Hammett, W. W. Lee, and W. M. Tang, “Shearing rate of time-dependent  $\mathbf{E} \times \mathbf{B}$  flow”, *Physics of Plasmas* **6**, 922–926 (1999).
- [49] R. E. Waltz and G. D. Kerbel, “Toroidal turbulence simulations with gyro-landau fluid models in a nonlinear ballooning mode representation”, *AIP Conference Proceedings* **284**, 310–343 (1994).
- [50] R. E. Waltz, R. L. Dewar, and X. Garbet, “Theory and simulation of rotational shear stabilization of turbulence”, *Physics of Plasmas* **5**, 1784–1792 (1998).
- [51] G. Dif-Pradalier, G. Hornung, X. Garbet, P. Ghendrih, V. Grandgirard, G. Latu, and Y. Sarazin, “The  $\mathbf{E} \times \mathbf{B}$  staircase of magnetised plasmas”, *Nuclear Fusion* **57**, 066026 (2017).
- [52] G. Hornung, G. Dif-Pradalier, F. Clairet, Y. Sarazin, R. Sabot, P. Hennequin, and G. Verdoolaege, “ $\mathbf{E} \times \mathbf{B}$  staircases and barrier permeability in magnetised plasmas”, *Nuclear Fusion* **57**, 014006 (2017).
- [53] A. G. Peeters, “The bootstrap current and its consequences”, *Plasma Physics and Controlled Fusion* **42**, B231–B242 (2000).
- [54] A. Peeters, Y. Camenen, F. Casson, W. Hornsby, A. Snodin, D. Strintzi, and G. Szepesi, “The nonlinear gyro-kinetic flux tube code GKW”, *Computer Physics Communications* **180**, 40 YEARS OF CPC: A celebratory issue focused on quality software for high performance, grid and novel computing architectures, 2650–2672 (2009).
- [55] J. Candy, “TGLF recalibration for ITER standard case parameters fy2015: theory and simulation performance target final report”, (2015).
- [56] A. J. Brizard and T. S. Hahm, “Foundations of nonlinear gyrokinetic theory”, *Rev. Mod. Phys.* **79**, 421–468 (2007).
- [57] J. A. Krommes, “The gyrokinetic description of microturbulence in magnetized plasmas”, *Annual Review of Fluid Mechanics* **44**, 175–201 (2012).
- [58] R. G. Littlejohn, “Variational principles of guiding centre motion”, *Journal of Plasma Physics* **29**, 111–125 (1983).
- [59] E. A. Frieman and L. Chen, “Nonlinear gyrokinetic equations for low-frequency electromagnetic waves in general plasma equilibria”, *The Physics of Fluids* **25**, 502–508 (1982).
- [60] W. W. Lee, “Gyrokinetic approach in particle simulation”, *The Physics of Fluids* **26**, 556–562 (1983).

- [61] J. R. Cary, “Lie transform perturbation theory for hamiltonian systems”, *Physics Reports* **79**, 129–159 (1981).
- [62] R. Courant, K. Friedrichs, and H. Lewy, “Über die partiellen differenzgleichungen der mathematischen physik”, *Mathematische Annalen* **100**, 32–74 (1928).
- [63] S. Hamada, *Nuclear Fission Research in Japan* **1**, 542 (1958).
- [64] S. Hamada, “Hydromagnetic equilibria and their proper coordinates”, *Nuclear Fusion* **2**, 23 (1962).
- [65] M. A. Beer, S. C. Cowley, and G. W. Hammett, “Field-aligned coordinates for nonlinear simulations of tokamak turbulence”, *Physics of Plasmas* **2**, 2687–2700 (1995).
- [66] W. D’haeseleer, ed., *Flux coordinates and magnetic field structure*, 1. (Springer-Verlag, Berlin, Heidelberg, New York, 1991).
- [67] B. Scott, “Global consistency for thin flux tube treatments of toroidal geometry”, *Physics of Plasmas* **5**, 2334–2339 (1998).
- [68] B. Scott, “Shifted metric procedure for flux tube treatments of toroidal geometry: avoiding grid deformation”, *Physics of Plasmas* **8**, 447–458 (2001).
- [69] H. R. H. Grad, “Hydromagnetic equilibria and force-free fields”, *Computer Physics Reports* **39** (1958).
- [70] V. D. Shafranov, “Plasma Equilibrium in a Magnetic Field”, *Reviews of Plasma Physics* **2**, 103 (1966).
- [71] H. Lütjens, A. Bondeson, and O. Sauter, “The chease code for toroidal mhd equilibria”, *Computer Physics Communications* **97**, 219–260 (1996).
- [72] V. D. Shafranov, “Equilibrium of a toroidal pinch in a magnetic field”, *Soviet Atomic Energy* **13**, 1149–1158 (1963).
- [73] X. Lapillonne, S. Brunner, T. Dannert, S. Jolliet, A. Marinoni, L. Villard, T. Görler, F. Jenko, and F. Merz, “Clarifications to the limitations of the  $s - \alpha$  equilibrium model for gyrokinetic computations of turbulence”, *Physics of Plasmas* **16**, 032308 (2009).
- [74] S. G. J. JM. Frigo, “The design and implementation of fftw3”, *Proc. IEEE* **93**, 216–231 (2005).
- [75] J. W. Connor and J. B. Taylor, “Ballooning modes or fourier modes in a toroidal plasma?”, *Physics of Fluids* (1977).
- [76] J. W. Connor, R. J. Hastie, and J. B. Taylor, “Shear, periodicity, and plasma ballooning modes”, *Phys. Rev. Lett.* **40**, 396–399 (1978).
- [77] E. A. Frieman, G. Rewoldt, W. M. Tang, and A. H. Glasser, “General theory of kinetic ballooning modes”, *The Physics of Fluids* **23**, 1750–1769 (1980).
- [78] A. G. Peeters, *GKW how and why (manual)* (2018).

## Bibliography

- [79] M. Hazewinkel, ed., *Encyclopedia of mathematics* (Springer Science+Business Media B.V., 1994).
- [80] M. Abramowitz, ed., *Handbook of mathematical functions: with formulas, graphs, and mathematical tables*, 9. (Dover Publications; 1965).
- [81] C. F. Karney, “Fokker-planck and quasilinear codes”, *Computer Physics Reports* **4**, 183–244 (1986).
- [82] P. H. Diamond, S.-I. Itoh, K Itoh, and T. S. Hahm, “Zonal flows in plasma - a review”, *Plasma Physics and Controlled Fusion* **47**, R35 (2005).
- [83] X. Garbet and R. E. Waltz, “Heat flux driven ion turbulence”, *Physics of Plasmas* **5**, 2836–2845 (1998).
- [84] A. Weikl, A. G. Peeters, F. Rath, S. R. Grosshauser, R. Buchholz, W. A. Hornsby, F. Seiferling, and D. Strintzi, “Ion temperature gradient turbulence close to the finite heat flux threshold”, *Physics of Plasmas* **24**, 102317 (2017).
- [85] X. Q. Xu, Z. Xiong, Z. Gao, W. M. Nevins, and G. R. McKee, “Tempest simulations of collisionless damping of geodesic-acoustic mode in edge plasma pedestal”, *Phys. Rev. Lett.* **100**, 215001 (2008).
- [86] L. Landau, *J. Phys. (UssR)* **10**, 25–34 (1946).
- [87] F. C. Grant and M. R. Feix, “Fourier-hermite solutions of the vlasov equations in the linearized limit”, *The Physics of Fluids* **10**, 696–702 (1967).
- [88] J. W. Banks and J. A. F. Hittinger, “A new class of nonlinear finite-volume methods for vlasov simulation”, *IEEE Transactions on Plasma Science* **38**, 2198–2207 (2010).
- [89] E. Camporeale, G. Delzanno, B. Bergen, and J. Moulton, “On the velocity space discretization for the vlasov-poisson system: comparison between implicit hermite spectral and particle-in-cell methods”, *Computer Physics Communications* **198**, 47–58 (2016).
- [90] H. Nyquist, “Certain topics in telegraph transmission theory”, *Transactions of the American Institute of Electrical Engineers* **47**, 617–644 (1928).
- [91] C. E. Shannon, “Communication in the presence of noise”, *Proceedings in IRE* **37**, 447–457 (1949).
- [92] J. Candy, *General Atomics Report GA-A28239* (2015).
- [93] A. E. White, L. Schmitz, W. A. Peebles, T. A. Carter, T. L. Rhodes, E. J. Doyle, P. A. Gourdain, J. C. Hillesheim, G. Wang, C. Holland, G. R. Tynan, et al., “A correlation electron cyclotron emission diagnostic and the importance of multifield fluctuation measurements for testing nonlinear gyrokinetic turbulence simulations”, *Review of Scientific Instruments* **79**, 103505 (2008).

- [94] C. Holland, A. E. White, G. R. McKee, M. W. Shafer, J. Candy, R. E. Waltz, L. Schmitz, and G. R. Tynan, “Implementation and application of two synthetic diagnostics for validating simulations of core tokamak turbulence”, *Physics of Plasmas* **16**, 052301 (2009).
- [95] M. Nakata, T.-H. Watanabe, and H. Sugama, “Nonlinear entropy transfer via zonal flows in gyrokinetic plasma turbulence”, *Physics of Plasmas* **19**, 022303 (2012).
- [96] A. Weikl, A. G. Peeters, F. Rath, F. Seiferling, R. Buchholz, S. R. Grosshauser, and D. Strintzi, “The occurrence of staircases in its turbulence with kinetic electrons and the zonal flow drive through self-interaction”, *Physics of Plasmas* **25**, 072305 (2018).
- [97] A. I. Smolyakov, P. H. Diamond, and V. I. Shevchenko, “Zonal flow generation by parametric instability in magnetized plasmas and geostrophic fluids”, *Physics of Plasmas* **7**, 1349–1351 (2000).
- [98] T.-H. Watanabe, H. Sugama, A. Ishizawa, and M. Nunami, “Flux tube train model for local turbulence simulation of toroidal plasmas”, *Physics of Plasmas* **22**, 022507 (2015).
- [99] K. Hallatschek and W. Dorland, “Giant electron tails and passing electron pinch effects in tokamak-core turbulence”, *Phys. Rev. Lett.* **95**, 055002 (2005).
- [100] C. Angioni, R. Duxand, E. Fableand, A. Peeters, and the ASDEX Upgrade Team, “Giant electron tails and passing electron pinch effects in tokamak-core turbulence”, *Plasma Phys. Control. Fusion* **49**, 2027 (2007).
- [101] R. E. Waltz, G. D. Kerbel, J. Milovich, and G. W. Hammett, “Advances in the simulation of toroidal gyro-landau fluid model turbulence”, *Physics of Plasmas* **2**, 2408–2416 (1995).
- [102] T. Görler, X. Lapillonne, S. Brunner, T. Dannert, F. Jenko, S. K. Aghdam, P. Marcus, B. F. McMillan, F. Merz, O. Sauter, D. Told, et al., “Flux- and gradient-driven global gyrokinetic simulation of tokamak turbulence”, *Physics of Plasmas* **18**, 056103 (2011).
- [103] F. Merz and F. Jenko, “Nonlinear interplay of TEM and ITG turbulence and its effect on transport”, *Nuclear Fusion* **50**, 054005 (2010).
- [104] F. Rath, A. G. Peeters, R. Buchholz, S. R. Grosshauser, F. Seiferling, and A. Weikl, “On the tertiary instability formalism of zonal flows in magnetized plasmas”, *Physics of Plasmas* **25**, 052102 (2018).
- [105] Y. Camenen, Y. Idomura, S. Jolliet, and A. Peeters, “Consequences of profile shearing on toroidal momentum transport”, *Nuclear Fusion* **51**, 073039 (2011).
- [106] J. Dominski, S. Brunner, T. Görler, F. Jenko, D. Told, and L. Villard, “How non-adiabatic passing electron layers of linear microinstabilities affect turbulent transport”, *Physics of Plasmas* **22**, 062303 (2015).

## Bibliography

- [107] J. Dominski, B. F. McMillan, S. Brunner, G. Merlo, T.-M. Tran, and L. Villard, “An arbitrary wavelength solver for global gyrokinetic simulations. application to the study of fine radial structures on microturbulence due to non-adiabatic passing electron dynamics”, *Physics of Plasmas* **24**, 022308 (2017).
- [108] F. Thomas, ed., *Experimentalphysik, Mechanik*, 1. (De Gruyter, Berlin, Boston, 2018).

## Eidstattliche Versicherung

Hiermit versichere ich an Eides statt, dass ich die vorliegende Arbeit selbständig verfasst und keine anderen als die von mir angegebenen Quellen und Hilfsmittel verwendet habe.

Weiterhin erkläre ich, dass ich die Hilfe von gewerblichen Promotionsberatern bzw. -vermittlern oder ähnlichen Dienstleistern weder bisher in Anspruch genommen habe, noch künftig in Anspruch nehmen werde.

Zusätzlich erkläre ich hiermit, dass ich keinerlei frühere Promotionsversuche unternommen habe.

Bayreuth, den .....

.....  
(Arne Weigl)